Molecular Nanomagnets Probed by Inelastic Neutron Scattering

A thesis submitted to the University of Manchester for the degree of

Doctor of Philosophy

in the Faculty of Science and Engineering

2017

Simon Geoffrey Ansbro

School of Chemistry

Contents

Contents 3

List of Figures 5

Abstract 7

Copyright Statement 12

Acknowledgements 15

Chapter 1 Introduction 17

- **1.1 Organisation of Thesis and Contributing Authors** 17
- **1.2 Introduction to Magnetism** 20
- **1.3 Introduction to Molecular Magnetism** 22
- **1.4 Spin Hamiltonian Formalism** 25
- **1.5 Introduction to Inelastic Neutron Scattering** 31
  - 1.5.1 Experimental Setup 33
  - 1.5.2 Nuclear Elastic Scattering 37
  - 1.5.3 Magnetic Scattering 39
- **1.6 Time-of-Flight Neutron Spectroscopy** 42
  - 1.6.1 Choppers 44
  - 1.6.2 Accessible Regions in (Q,E) Space 45
  - 1.6.3 Single Crystal INS 46
  - 1.6.4 Data Cleaning 48
  - 1.6.5 Advantages of ToF Neutron Spectroscopy 49
- **1.7 Overview of Recent Research** 50

Chapter 2 INS Spectroscopy of Molecular Nanomagnet Dimers 57

- **2.1 Background** 57
- **2.2 Spectroscopy of Nanomagnet Dimers Paper** 59

Chapter 3 INS Study of Cr_7Co ... 67

3.1 Cr_7Co Background ... 67

3.2 Spin Dynamics of Cr_7Co ... 67

Chapter 4 INS Study of Mn_{12} ... 78

4.1 Mn_{12} Background ... 78

4.2 Unravelling the Spin Dynamics of Mn_{12} Paper ... 81

Chapter 5 Entanglement Unravelled by INS ... 99

5.1 Entangled Dimer Background ... 99

5.2 Portraing Entanglement in a Nanomagnet Dimer Paper ... 102

Chapter 6 Conclusion ... 110

References ... 112

List of Figures

Figure 1. Illustration of the general form of a molecular nanomagnet showing the magnetic core and protective ligand shell.. 23

Figure 2. Electron configuration of the 3*d* electrons in Ni(II)...................... 24

Figure 3. Crystal field diagram for the Ni(II) ion in an octahedral symmetry, showing splitting from the barycentre and resultant energy levels. 24

Figure 4. Energy level diagram of the Ni(II) ion under the influence of a weak octahedral field and spin-orbit coupling, for which the multiplicity of the state is shown numbered in brackets... 25

Figure 5. Standard experimental set up for a neutron experiment with incident neutron energy E_i and incident neutron wavevector k_i scattering off of sample onto detector with final energy E_f and wavevector k_f....................................... 34

Figure 6. The scattering triangle for a neutron experiment defining the momentum transfer Q, where the incident neutrons with wavector k_i are scattered into a final state k_f whereby for elastic scattering k_i=k_f. 35

Figure 7. Schematic of a neutron with incident wavector k_i scattering from a target into detector with area *d*A 36

Figure 8. Standard setup for a neutron spectrometer featuring choppers, sample and detector with istances shown. Image adapated from [44]. 44

Figure 9. Distance *vs* time diagram for the chopper set up, sample and detectors on the ToF spectrometer IN5 at the Institut Laue-Langevin........... 46

Figure 10. Several scans taken using IN5 of a molecular nanomagnet measured at different rotation angles in ToF... 48

Figure 11. Simultaneously obtained maps of S(Q,w) for a Tb-Cu molecular nanomagnet with incident neutron energy a) 4.9 b) 8.3, c) 16.8, d) 50 meV [57]... 52

Figure 12. Schematic of the lanthanide compounds investigated 1-3. Where for 1. X=Y=H 2. X=CH_3 Y=I and 3. X=Cl and Y=H 53

Figure 13. Visualisation of the provoking of the spin propagation in the Cr_8 ring.. 54

Figure 14. Spin density and configuration obtained from D3 experiment on Cr7Cd adapted from[60].. 56

Figure 15. Schematic of the activation barrier in Mn12 80

Abstract

Molecular Nanomagnets Probed by Inelastic Neutron Scattering. A thesis submitted to the University of Manchester for the degree of Doctor of Philosophy in the faculty of Science and Engineering.

Molecular nanomagnets have the potential to address many technological challenges whilst also giving insights into fundamental quantum behaviours. In order to accomplish this it is crucial that a determination of the magnetic properties of these nanoscopic objects is established. Inelastic neutron scattering (INS) is at the forefront of these investigations and is a technique capable of unravelling vast amounts of information that can enable a detailed understanding and tailoring of the properties of these molecules. This thesis demonstrates the application of this state-of-the-art technique to a number of different yet important nanomagnets in the field, pushing the technique to the limit to yield new insights into the underlying physics in these systems. The potential of this technique is finely displayed in the unravelling of the spin dynamics in a supramolecular $(Cr_7Ni)_2$ dimer, where the intermolecular entanglement is portrayed in the vast 4D phase space extracted. This work also harnesses the full power of the 4D-INS technique to resolve the long standing issue of the spin Hamiltonian in the archetypal single molecule magnet (SMM) Mn_{12}, which after hundreds of papers since the realisation of its magnetic properties some 25 years ago had still not been convincingly settled. A little utilised avenue to building on Mn_{12} and generating better SMMs is also suggested and the evolution of the technique demonstrated by

characterising the magnetic properties in a tiny quantity of nanomagnet dimers.

Declaration

I declare that no portion of the work referred to in this thesis has been submitted in support of an application for another degree or qualification of this or any other university or other institute of learning.

Simon Ansbro

2017

Copyright Statement

(i) The author of this thesis (including any appendices and/or schedules to this thesis) owns certain copyright or related rights in it (the “Copyright”) and he has given the University of Manchester certain rights to use such Copyright, including for administrative purposes.

(ii) Copies of this thesis, either in full or in extracts, and whether in hard or electronic copy, may be made only in accordance with the Copyright, Designs and Patents Act 1988 (as amended) and regulations issued under it or, where appropriate, in accordance with licensing agreements that the University has from time to time. This page must form part of any such copies made.

(iii) The ownership of certain copyright, patents, designs, trademarks and other intellectual property (the “Intellectual Property”) and any reproductions of copyright works in the thesis, for example graphs and tables (“Reproductions”), which may be described in this thesis, may not be owned by the author and may be owned by third parties. Such Intellectual Property and Reproductions cannot and must not be made available for use without the prior written permission of the owner(s) of the relevant Intellectual Property and/or Reproductions.

(iv) Further information on the conditions under which disclosure, publication and commercialisation of this thesis, the copyright, and any intellectual property and/or reproductions described within it may take place is available in the University IP Policy, in any relevant thesis restriction declarations deposited in the University Library, the University Library's regulations, and in the University's policy on the presentation of theses.

Acknowledgements

This work would not have been possible without the support of many people. Firstly I would like to thank my supervisors Dr Hannu Mutka, Professor Richard Winpenny and Professor Paolo Santini for their helpful suggestions and guidance. I am greatly indebted to the advice and teachings of Professor Stefano Carretta, Professor David Collison and Professor Eric McInnes. I am also very grateful for the invaluable assistance throughout different aspects of this project from Dr Jacques Ollivier, Dr Tatiana Guidi, Dr Alessandro Chiesa, Dr Elena Garlatti, Dr Eufemio Moreno and Dr Grigore Timco. Thank you to all of the magnets group (past and present) and the PhD students at the ILL for their advice, assistance and friendship.

I would like to thank my family, in particular my parents Derek and Dawn for all their love and support. Finally, to my wife Kittie, thank you for your love, patience and continuing faith, which has sustained me throughout.

Chapter 1 Introduction

1.1 Organisation of Thesis and Contributing Authors

Chapter 1 gives an introduction to the field of research and an overview of the thesis. A brief description of the basic concepts of this work including an introduction to the measurement technique utilised (inelastic neutron scattering) is covered.

Chapter 2 presents the magnetic characterisation of two molecular nanomagnet dimers that show potential for application in molecular electronics. The paper has been written by this author, with support on the INS measurements provided by Hannu Mutka and Jacques Ollivier. The samples were synthesised by Wen Yu with XRD and susceptibility data collected by Eufemio Moreno. INS and susceptibility simulation codes were written by Alessandro Chiesa with all data analysis and simulations carried out by this author. The project was conceived and proposed by this author and Mario Ruben.

Chapter 3 provides an investigation into the magnetic properties of a Cr_7Co molecular nanomagnet, this molecule represents a less explored methodology to obtaining effective single molecule magnets. The paper has been written by this author who also carried out the INS measurements with Jacques Ollivier, Hannu Mutka, Elena Garlatti Tatiana Guidi and Michael Baker. A model for the INS simulations was made by Elena Garlatti, Stefano Carretta, Paolo Santini and Giuseppe Amoretti. Data analysis has been carried out by this author, Elena Garlatti, Alessandro Chiesa and Tatiana Guidi. Calculations and fits were performed by this author and Elena Garlatti. The structure was solved by Inigo Vitorica-Yrezbal. The sample was synthesised and grown by Grigore Timco and the project was conceived and proposed by Richard Winpenny, Stefano Carretta, Paolo Santini and Giuseppe Amoretti.

Chapter 4 is a detailed characterisation of the spin dynamics of Mn_{12} using four-dimensional inelastic neutron scattering to obtain a vast amount of information on this archetypal single molecule magnet. This paper has been written by Alessandro Chiesa, Stefano Carretta and Paolo Santini with input from all authors. Tatiana Guidi and this author performed the INS experiment, the structure and crystal alignment was performed by Inigo Vitorica-Yrezabal. The sample was synthesised and grown by Grigore Timco. Data analysis was conducted by this author, Alessandro Chiesa, Stefano Carretta and Tatiana Guidi. The calculations and fits were performed by Alessandro Chiesa, Elena Garlatti, Stefano Carretta, Paolo Santini and Giuseppe Amoretti. The project was proposed by Richard Winpenny, Tatiana Guidi, Stefano Carretta, Paolo Santini and Giuseppe Amoretti.

Chapter 5 demonstrates the capability of inelastic neutron scattering to unravel the entanglement in a supramolecular molecular nanomagnet dimer, consisting of two prototypical molecular qubits. The paper was written by Elena Garlatti and Stefano Carretta with inputs from all authors. This author, Jacques Olliver, Hannu Mutka, Tatiana Guidi Elena Garlatti, Paolo Santini and Stefano Carretta performed the INS experiment. Data treatment was made by this author, Elena Garlatti, Tatiana Guidi and Jacques Ollivier. The structure of the compound was determined by Inigo Vitorica-Yrezbal and George Whitehead. The sample was synthesised and crystals grown by Grigore Timco. A model and data simulations were performed by Elena Garlatti, Paolo Santini, Stefano Carretta and Giuseppe Amoretti. The project was conceived and proposed by Richard Winpenny, Stefano Carretta, Paolo Santini and Giuseppe Amoretti.

Chapter 6 concludes this thesis.

A note on the format of this thesis

This thesis has been written in the alternative format style where each of the chapters are presented in the form that they would take in a journal publication. This work is highly collaborative and has been undertaken at large-scale facilities such as the ILL and ISIS neutron sources, whose exposure is heavily reliant on rapid publication of obtained results. The work carried out in this thesis is of interest to those working in the wider field and this method reduces the process of having to rewrite chapters for publication later on and greatly facilitates their eventual publication to promptly distribute these findings.

1.2 Introduction to Magnetism

Whilst man has been fascinated by the seemingly invisible force of magnetism for at least a couple of millennia, he has also sought to harness its apparently mystical properties, from the earliest days of the compass needle, to the smartphones in our pockets today. The drive to understand this behaviour has propelled electromagnetism to be one of the most important research areas in modern physics. Oersted demonstrated this link in 1820 when he showed that an electric current passing through a wire generated a magnetic field, with Maxwell later uniting electricity and magnetism in his famous equations. Progress in the understanding of magnetism since Oersted's findings has been rapid, permitting some of the very intricate devices that surround us today[1].

A true understanding of magnetism requires a quantum approach and the magnetism we see around us is due to the unpaired electron's orbital (l) and spin angular momentum (s) that gives rise to a magnetic moment, the fundamental object in magnetism. When considering this atomic origin it is necessary to apply a vector sum to these quantities, such that the total momenta are given by the sum of each unpaired electron present in a magnetic body, that is to say $S = \sum_i s_i$ and $L = \sum_i l_i$. Due to spherical symmetry a filled shell will sum to zero and so only contributions from a partially filled shell will respond in a paramagnetic moment. The combination of these two quantities yielding the state with the lowest energy is described by Hund's rules, where the state lowest in energy is that which has the highest multiplicity $(2S + 1)$. For such a given multiplicity, the term with the largest L is then lowest in energy. Lastly, for less than half-full shells $\mathrm{J} = L - S$ and for more than half-full shells $\mathrm{J} = L + S$.

The effective magnetic moment can then be calculated as

$$\mu_{eff} = g\mu_B\sqrt{J(J+1)} \qquad (1.1)$$

With μ_B the Bohr magneton and the Lande g-value is given by $g = \frac{3}{2} + \frac{S(S+1) - L(L+1)}{2J(J+1)}$

Although this is the case for free ions if there is a quenching of the orbital angular momentum then the effective magnetic moment can be described solely by the spin angular momentum component

$$\mu_{eff} = g\mu_B\sqrt{S(S+1)} \qquad (1.2)$$

This simplification is frequently applicable for the 3*d* ions found in molecular nanomagnets[2].

1.3 Introduction to Molecular Magnetism

Molecular nanomagnets are molecules with a magnetic core surrounded by an organic ligand sheath which acts to protect the core from magnetic intermolecular interactions and isolates the molecules into zero-dimensional magnetic units. This puts them on a length scale much smaller than more conventional magnetic nanoparticles. Due to this nanoscopic nature they display interesting quantum effects[3-5] that have motivated many to understand such behaviours but also to exploit them for various revolutionary applications[6-8].

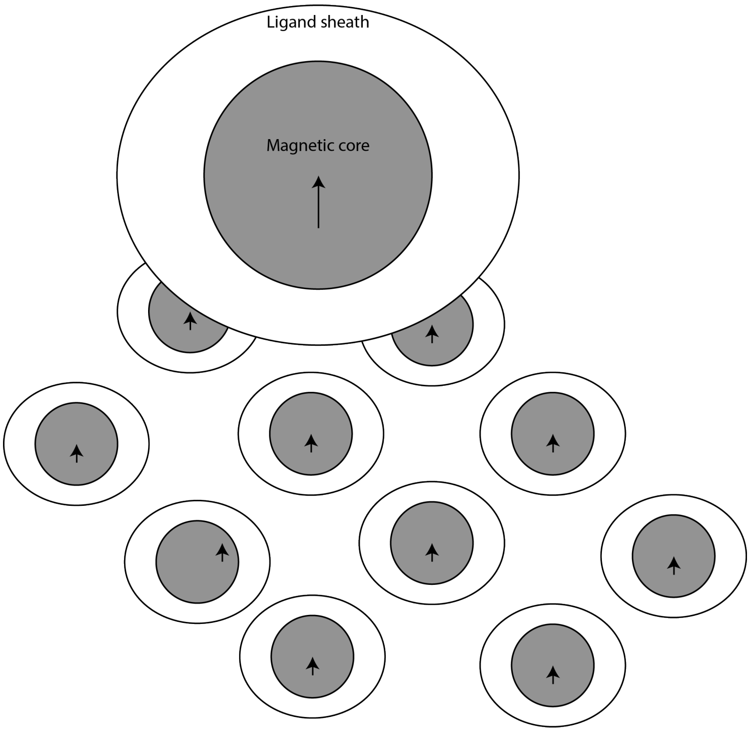

Figure 1. Illustration of the general form of a molecular nanomagnet showing the magnetic core and protective ligand shell.

The metal ions in molecular nanomagnets therefore cannot be considered free, since they are bound to the ligands. This changes the previously discussed energy arrangement, which is typically described through crystal field theory.

For example one of the common ions used throughout molecular nanomagnetism is Ni(II) 3d^8.

m_l=-2	m_l=-1	m_l=0	m_l=1	m_l=2
↓↑	↓↑	↓↑	↑	↑

Figure 2. Electron configuration of the 3*d* electrons in Ni(II).

The ground state term is L=2+1=3 =^{3}F (where S=0,P=1,D=2,F=3 etc.). In an octahedral environment, the *d* electrons are arranged as shown in figure 3.

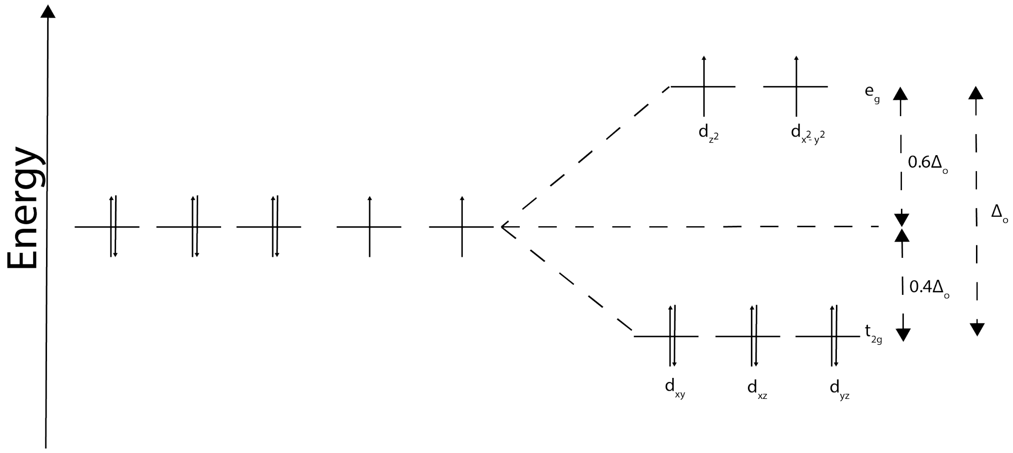

Figure 3. Crystal field diagram for the Ni(II) ion in an octahedral symmetry, showing splitting from the barycentre and resultant energy levels.

The $t^6_{2g}\ e^2_g$ in a weak octahedral field takes the ^{3}F state to a ^{3}A ground state term. Although no first order anisotropy is expected from the A term, the promotion of an electron to one of the e_g states will result in an uneven occupation. Hence, this will result in an anisotropic excited state and therefore there can be single ion anisotropy due to the mixing of these anisotropic excited states with the ground state.

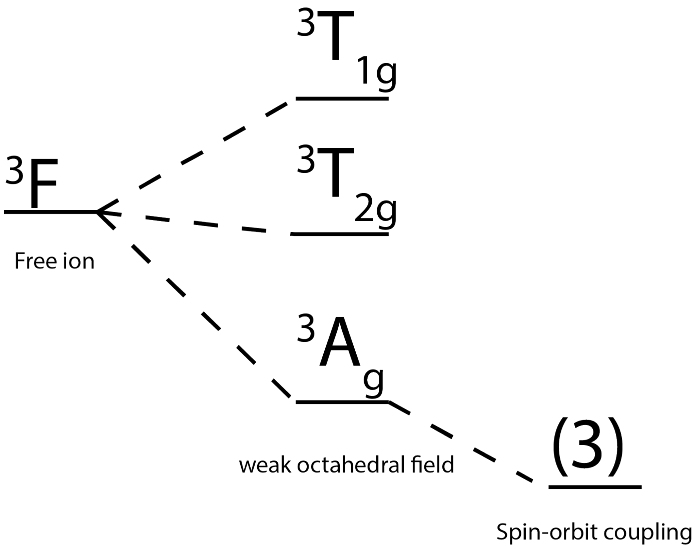

Figure 4. Energy level diagram of the Ni(II) ion under the influence of a weak octahedral field and spin-orbit coupling, for which the multiplicity of the state is shown numbered in brackets.

In a perfectly symmetric octahedral field the result of the mixing is to reduce the energy of the ground state term, no degeneracy is lifted. In real molecules of course this will deviate from this perfect scenario[9].

Commonly in molecular magnetism there is more than one metal centre and the spin moments localised on these metal centres can undergo exchange interactions. These interactions are commonly forged by the overlap of the orbitals of the metal centres or through the bridging ligands[2,10]. The type of coordination ligand used, the degree of orbital overlap as well as the bridging angle all affect the strength of this interaction and thus the underlying magnetism in the complex[11]. This interaction is a result of the symmetrical requirements on the exchange of identical particles since electrons must pair according to the Pauli principle[2]. The description used for the energy levels of single ions is now no longer a good description for the system and so we must look to the spin Hamiltonian formalism to get a description of the quantum energy of a system with paired spin centres.

1.4 Spin Hamiltonian Formalism

This formalism is key in describing the fundamental magnetic properties of most molecular nanomagnets and unravelling the terms which parameterise the Hamiltonian, in light of their chemical structure is essential for the rational design of future molecules tailored for application.

Underlying the spin Hamiltonian formalism is the assumption that the metal ions contained within a molecule can each be treated as an effective spin s and that all the contributions to the energy of the system can solely be expressed as operators[12].

The most dominant contribution to describing the magnetic properties of a molecular nanomagnet is almost always from the exchange interaction. The Hamiltonian for two electrons at sites i and j interacting via this interaction can be expressed as

$$\hat{H} = \sum_{i>j} J_{i,j} \hat{S}_i \cdot \hat{S}_j \tag{1.3}$$

Where J is the measure of the exchange interaction, with a positive J describing an antiferromagnetic exchange and a negative J describing a ferromagnetic exchange. $\hat{S}_x$ where $\hat{S}$ is the spin operator of the ion at site x. This term is frequently referred to as the Heisenberg Hamiltonian. Whilst the case for two spins has been shown this formalism can easily be expanded for larger spin systems by summing over all the necessary spin pairs.

The local environment of the metal ions in molecular nanomagnets often requires the addition of a local zero-field splitting tensor taking its major contribution from single ion anisotropy. For spin systems with $S > 1/2$ having non-cubic symmetry, the dipole-dipole coupling between the electron spins removes the 2S+1 fold degeneracy from the ground state. The name of this tensor derives from its field-independent origin for which the Hamiltonian term takes the form

$$\hat{H} = \sum_i \hat{S}_i \cdot D_i \cdot \hat{S}_i \qquad (1.4)$$

Where D_i is the local anisotropy tensor at the *i*th site. If the coordinates of the system *(x,y,z)* are chosen such that they are parallel to the orthogonal eigenvectors of the real, symmetric tensor *D*, then this term in the Hamiltonian can be rewritten as

$$\hat{H} = D_x\hat{S}_x^2 + D_y\hat{S}_y^2 + D_z\hat{S}_z^2 \qquad (1.5)$$

$$= D\left[\hat{S}_z^2 - \tfrac{1}{3}S(S+1)\right] + E\left(\hat{S}_x^2 - \hat{S}_y^2\right)$$

Where $D = \frac{3D_z}{2}$ and $E = \frac{(D_x - D_y)}{2}$. When there exists cubic symmetry $D = E = 0$ and if the symmetry is axial then $D \neq 0$ and $E = 0$. For symmetries lower than axial $D \neq 0$ and $E \neq 0$.

In many cases these two main terms are sufficient to describe the spin interactions in *3d* molecular nanomagnets, however there are instances when more complex terms must be accounted for in the total effective spin Hamiltonian representing the system. One of these frequently encountered terms is that which accounts for anisotropic exchange.

$$\hat{H} = \sum_{i>j} \sum_{\alpha\beta} J_{ij}^{\alpha\beta} \hat{S}_{i,\alpha} \hat{S}_{j,\beta} \qquad (1.6)$$

Where α, β represent x, y, z and $J_{i,j}^{\alpha\beta}$ is a measure of the anisotropic exchange interaction.

One final exchange term, that is less commonly encountered, is one describing antisymmetric exchange or otherwise called the Dzyaloshinsky-Moriya interaction. For two spin centres this interaction reduces to zero if there exists a centre of inversion between them. This interaction breaks parity symmetry and states with different parity can therefore mix. This interaction is not necessary to describe the magnetism of any of the compounds in this work.

$$\hat{H} = \sum_{i>j} G_{ij} \cdot \hat{S}_i \times \hat{S}_j \tag{1.7}$$

In the presence of an external magnetic field one must also remember to take into account the term accounting for the Zeeman effect that results in the splitting of the energy levels[10,13].

$$\hat{H} = \sum_i \mu_B B \cdot g \cdot \hat{S}_i \tag{1.8}$$

The isotropic part of the exchange is determined by chemical bonding, whereas the anisotropic and antisymmetric exchange is determined by relativistic effects through the mixing of excited states into the ground state via spin-orbit coupling.

The total dimension of the Hamiltonian matrix for diagonalisation is given by $Dim = \prod_i^N (2S_i + 1)$ thus the dimension of the Hilbert space grows incredibly large for several magnetic ions and can be very computationally demanding. It follows that for such large spin systems it is often necessary to exploit various techniques to simplify the task of diagonalising large matrices.

Whilst the majority of studies take place on polycrystalline powders, these compounds can also be grown into large single crystals, opening up the opportunity to obtain a very detailed characterisation of their magnetic properties. The confined nature of these molecules means that one is essentially probing the magnetic properties of a single molecule from bulk measurements.

Undoubtedly the most well known molecular nanomagnet is Mn_{12}. This molecule is part of a special subclass of molecular nanomagnets known as single-molecule magnets (SMMs). The defining feature of this class of compounds is that they retain their magnetisation M in the absence of an applied magnetic field H. SMMs, like conventional magnets show hysteresis loops. However, in contrast these hysteresis loops are not the result of collective long-range interactions from an ordered system but instead, originate from the individual magnetically isolated molecule. The term "single-molecule magnet" is therefore one that is evocative of conventional magnetic behaviour rather than a physically accurate description. The discovery of this particular $Mn_{12}O_{12}(O_2CCH_3)_{16}(H_2O)_4].2CH_3COOH.4H_2O$ molecule in the 1980s[14] and later reporting of its magnetic properties in the mid-90s[15,16] led to a huge surge of interest in the field of molecular magnetism[17-19], with the hope of exploiting these exciting materials in spintronic technologies. The retained magnetisation states of M and –M (depending on the field direction) opens up the possibility of employing them as bit states, with their single molecule nature allowing the possibility of extremely dense magnetic storage devices.

Whilst many efforts have been made to understand and improve the remarkable properties of Mn_{12}, others have pursued different chemical routes to obtain the high spin ground state and large axial anisotropy characteristic of successful SMMs. This therefore requires different measurement techniques, such as electron paramagnetic resonance (EPR)[20,21] and inelastic neutron scattering[22] (INS) to unravel such properties of these systems.

These different aspects of molecular magnetism make the field itself highly interdisciplinary, with chemists and physicists in particular, working closely together to synthesise, characterise and tailor molecules towards specific applications. One group of compounds that epitomise this process are the chromium based antiferromagneic wheel complexes that derive from the parent compound $[Cr_8F_8(O_2C^tBu_{16})]$[23]. This compound consists of eight chromium (III) ions arranged in a regular octagon, bridged by eight fluoride ions on the inside of the ring and sixteen carboxylates. The compound crystallises in a tetragonal space group with all the chromiums antiferromagnetically coupled, giving an $S=0$ ground state[24]. One of the striking features of this compound is its chemical versatility. Not only is it possible to change the structure with different templates[25], swap the outer ligands[26,27] as well as expand on them to bridge to other metal cores[28-30], but it is feasible to replace one of the Cr(III) sites with other d-metal ions of differing valency, giving a controlled tuning of the magnetic properties of the system. Of the different possible spin rings synthesised, particular success has been achieved by adding divalent metals to the reaction mixture to produce rings with an S=1/2 spin ground state, such as Cr_7Ni, and Cr_7Co. Molecular nanomagnets with an S=1/2 spin ground state are of particular importance since the S=1/2 spin ground state is a necessary prerequisite for encoding these nanomagnets as molecular qubits[6]. Cr_7Ni is one of the finest examples of a molecular qubit and has been the subject of many investigations into understanding these properties and maximising those which enhance its applicability for quantum information processing[31]. One such contemporary area of focus is the linking of these rings together in an attempt to satisfy the need for an ordered array of entangled qubits[32].

Whilst the implementation of quantum information processing and the realisation of such a high density of data storage may still be some way off, the continued technological revolution of spintronics[33,34] (where the spin degree of freedom is utilised in conjunction with that of the charge) is reaching new bounds by combining with the field of molecular electronics[35]. Molecular nanomagnets establishes a perfect link between these fields and in one recent example, a Co-based molecular nanomagnet dimer with its spin centres coupled has been used to create a single molecule junction[34]. It was demonstrated that the lowest electronic states of the system, namely the pseudo-singlet and the pseudo-triplet could be repeatedly switched between by applying a finite bias. Such controlled electronic manipulation of single molecules at this level is crucial for the continued theme of minimisation of technology and provides a direct viewpoint into the physics of materials at the molecular level.

All of the molecular nanomagnets referred to in the above introduction are at the focal point of areas that span different, but each very crucial parts of the field of molecular magnetism. They are also at the centre of the main investigations of this thesis.

Whilst different techniques have been historically employed to investigate the properties of molecular nanomagnets, Inelastic Neutron Scattering (INS) remains one of the most powerful techniques and arguably the best to quantify exchange and zero-field splitting parameters for the spin Hamiltonian formalism[22,36].

1.5 Introduction to Inelastic Neutron Scattering

Inelastic neutron scattering (INS) is a technique that has had an integral role in the development of the field of molecular nanomagnetism, however, even in the wider sense it is an important technique to probe excitations in many different areas of condensed matter research[37-39]. The neutron's general applicability for experiments in condensed matter physics originates from its intrinsic properties[40,41]:

1) The thermal neutron's de Broglie wavelength is on the same order as the atomic spacings in most materials, and thus they can be used to study molecular order through the process of diffraction.

2) The neutron is a charge-neutral particle and so is able to penetrate deeply into matter without being perturbed by electrostatic interactions. This means we can be certain we are observing the bulk behaviour and not deviatory, unique surface effects.

3) The neutron possesses a magnetic dipole moment and thus interacts with that of unpaired electrons' making it sensitive to magnetic interactions in materials.

4) The energy of cold neutrons is on the same order of magnitude as many of the common excitations that we would like to study.

In an inelastic collision a significant portion of the neutron's initial energy is exchanged with the sample and so detailed information on the excitation being studied can be extracted. It is important to note that the neutron must still have sufficient remaining energy after this inelastic process, otherwise it will not reach the detector.

The properties of the neutron also lead to some drawbacks. Neutron scattering is an intensity limited technique. The weakly interacting nature of the neutron means that large sample masses are frequently necessary but this is not always synthetically practical, particularly when single crystal samples are required. A further complication is that whilst neutrons themselves are plentiful, the production of free neutrons (unbound from atomic nuclei) is a considerable technical challenge.

The requirement for an intense beam of neutrons necessitates that they are produced at large-scale facilities such as reactor and spallation sources. A reactor source such as that present at the ILL utilises the nuclear fission of U^{235} to produce a chain reaction, resulting in a flux of high-energy neutrons, which are then moderated before being transported to the various instrumentation present at the facility.

In a spallation source such as at ISIS, H^- ions are accelerated through a linac to approximately 37 % of the speed of light. They are then injected into a synchrotron where they are stripped of their electrons, leaving just protons. When a sufficient quantity of protons has been amassed they are accelerated around the synchrotron by radio frequency electric fields and separated into bunches travelling at about 84% the speed of light. These are extracted from the synchrotron and directed at a heavy tungsten target. The collision produces extremely intense pulses of neutrons through a physical process known as spallation. The neutrons are then moderated and directed towards the instrumentation present.

A consequence of the extreme lengths one has to go to in the production of neutrons, is that neutron experiments are very expensive and so the time afforded for experimentation is far more limited than for in-house techniques.

The theory of neutron scattering is well established and the reader is referred in particular to the texts by Lovesey[42] and Squires[43]. This section however is intended to give a brief overview of the main concepts of neutron scattering that have been invoked in this work.

1.5.1 Experimental Setup

The standard neutron scattering experiment is based on the relatively simple arrangement shown below:

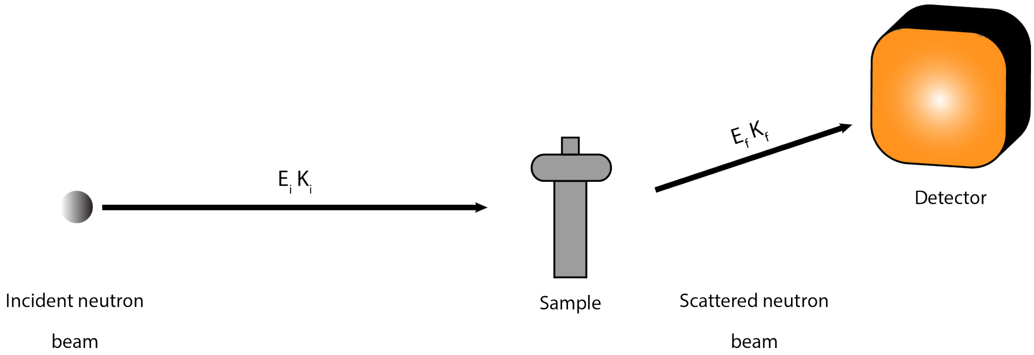

Figure 5. Standard experimental set up for a neutron experiment with incident neutron energy E_i and incident neutron wavector k_i scattering off of sample onto detector with final energy E_f and wavector k_f.

The neutrons are incident on the sample with a known energy E_i and so we are concerned with detecting where the scattered neutrons have gone and with what energy they now have.

Let us consider the incident neutron described by an initial wavevector k_i scattering from the sample resulting in a subsequent wavector k_f. We will define the angle subtended by the initial and final wavector as 2θ. The momentum transfer to the sample is then $\hbar Q$ where Q is defined as the scattering vector given by $k_i - k_f$.

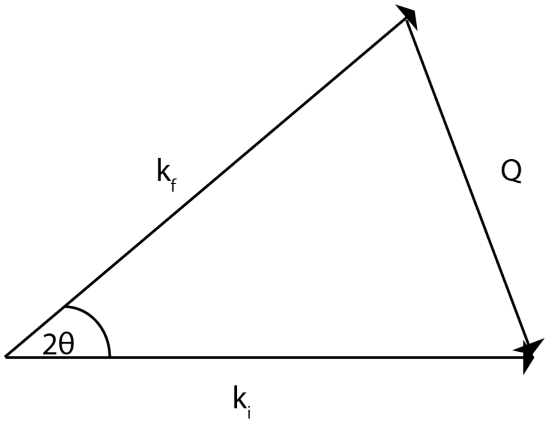

Figure 6. The scattering triangle for a neutron experiment defining the momentum transfer Q, where the incident neutrons with wavevector k_i are scattered into a final state k_f whereby for elastic scattering k_i=k_f.

As well as this momentum exchange, we also define the energy exchange that takes place in an inelastic collision, with initial neutron energy E_i and final energy E_f resulting in the energy transfer of

$$\Delta E = \hbar\omega = E_i - E_f = \frac{\hbar^2}{2m_n}\left(k_i^2 - k_f^2\right) \qquad (1.9)$$

Where m_n is the neutron mass.

Depending on the energy transfer, the scattered neutrons that have enough remaining energy can reach the detector. By analysing the scattered intensity as a function of the direction and energy, we can learn a huge amount of information about our sample.

Let us define the particle flux detected within an angular element

$$d\Omega = \sin\theta \, d\theta d\Phi \qquad (1.10)$$

The area of the detector and the corresponding solid angle encompassed are then related by

$$dA = r^2 d\Omega \qquad (1.11)$$

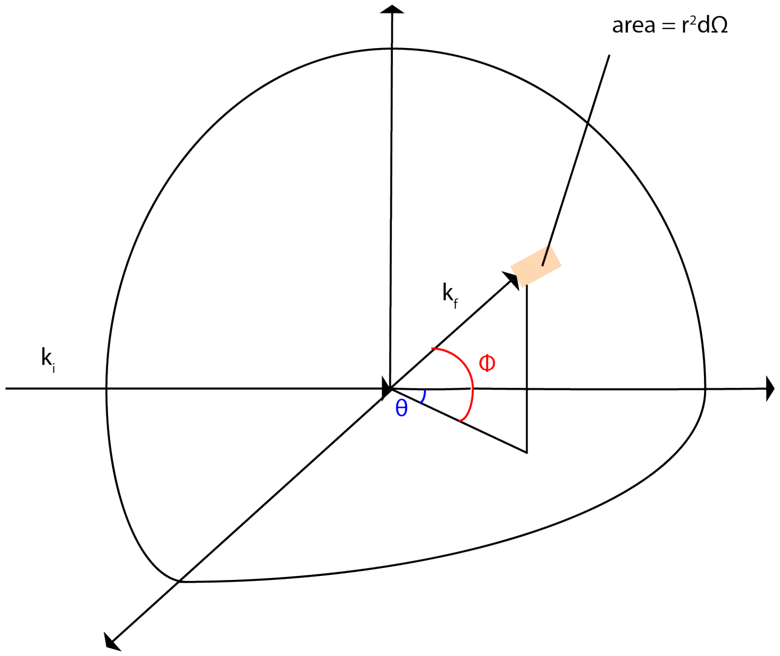

Figure 7. Schematic of a neutron with incident wavevector k_i scattering from a target into a detector of area *d*A.

If we assume that the detectors are sufficiently far away so that they are capable of resolving the direction of scattering with the required precision, we then wish to determine the ratio of the flux scattered into the angular element $d\Omega$ and the initial flux impinging on the sample.

$$d\sigma = r^2 d\Omega \frac{J_{scattered}(r,\theta,\phi,t)}{J_{initial}(t)} \tag{1.12}$$

We can then define the differential scattering cross section.

$$\frac{d\sigma}{d\Omega} d\Omega = \int d\sigma \tag{1.13}$$

Which being an area is given in units of m^2 and for convenience is often expressed in barns, where 1 barn = 10^{-24} cm^2

In an INS experiment we use the detectors to obtain the energy of the scattered neutrons with E_f $E_f + dE_f$, which leads us to the concept of the double differential cross section.

$$d^2\sigma = \frac{\mathit{flux\ scattered\ into\ } d\Omega \mathit{\ with\ an\ energy\ between\ } E_f \mathit{\ and\ } E_f + dE_f}{\mathit{initial\ flux\ onto\ the\ sample\ with\ the\ energy\ } E_i} d\Omega dE_f \qquad (1.14)$$

This leads us to the definition of the partial differential cross-section, which is the basic quantity, measured in a neutron scattering experiment

$$\frac{d^2\sigma}{d\Omega dE_f} = \frac{\substack{\mathit{flux\ scattered\ into\ the\ solid\ angle\ } d\Omega \mathit{\ in\ the\ direction\ } (\theta,\phi) \\ \mathit{with\ an\ energy\ between} E_f \mathit{\ and\ } E_f + dE_f}}{\phi d\Omega dE_f} \qquad (1.15)$$

Since the interaction between the neutron and sample is very weak it is possible to treat the ensuing interaction potential as a perturbation. Fermi's Golden rule can then be applied to calculate the transition probability W between the initial and final states of the sample ($\lambda_i\ and\ \lambda_f$ respectively). This is equivalent to the Born approximation which assumes the incoming and outgoing neutron beams can be treated as plain waves.

$$W_{|\lambda_i k_i \sigma_i\rangle \to |\lambda_f k_f \sigma_f\rangle} = \frac{2\pi}{\hbar} \left|\langle \lambda_i k_i \sigma_i | V | \lambda_f k_f \sigma_f \rangle\right|^2 \rho k_f \qquad (1.16)$$

Again $k_i$and $k_f$are the initial and final wavectors with σ being the neutron spin. The ρk_f term describes the number of momentum states contained in the solid angle $d\Omega$ for neutrons in the state k_f.

By summing over all final states and assuming we are dealing with unpolarised neutrons we can average over all incident states. One then obtains the following:

$$\frac{d^2\sigma}{d\Omega dE_f} = \frac{k_f}{k_i}\left(\frac{m_n}{2\pi\hbar^2}\right)^2 \sum_{\lambda_i \lambda_f} p_\lambda \sum_{\sigma_i \sigma_f} p_\sigma \left|\langle \lambda_f \sigma_f | V(Q) | \lambda_i \sigma_i \rangle\right|^2 \delta\left(\hbar\omega + E_i - E_f\right)$$

(1.17)

Where m_n is the mass of the neutron p_λ and p_σ are statistical weight factors for the initial states $|\lambda_i \sigma_i\rangle$. $V(Q)$ describes the Fourier transform of the neutron-matter interaction potential $V(r)$ at the scattering vector Q.

Where $V(Q) = \int drV(r)e^{iQ\cdot r}$

Finally δ is the Dirac delta function and here it ensures the conservation of energy.

The interaction potential V can take different forms depending on the type of interaction between the neutron and sample. One such interaction is of nuclear elastic scattering between the neutron and the atomic nuclei in the material, which is mediated by the strong nuclear force.

1.5.2 Nuclear Elastic Scattering

This interaction can be described by the Fermi pseudo-potential:

$$V_j(r) = \frac{2\pi\hbar^2}{m_n}\bar{B}_j\delta\left(r - R_j\right) \tag{1.18}$$

Where r is the incident neutron's position, j is the index of the atomic nucleus at the position R_j. The scattering length $\bar{B}_j$ is complex for the case of absorption but otherwise a real quantity. Its value depends on the details of the nuclear structure, which is not relatable in a simplistic way to the atomic number. Neutron scattering is therefore particularly strong at discriminating between different elements with similar atomic numbers or even the same element with different isotopes as the scattering length can vary wildly with subtle changes in the nuclear structure.

The scattered intensity contains not only a component that depends on Q and that reflects the structure of the target, but also an additional component that scatters isotropically. These are termed coherent and incoherent scattering respectively. Both have their own associated cross-sections related to the partial differential scattering cross-section as

$$\frac{d^2\sigma}{d\Omega dE_f} = \frac{d^2\sigma_{coh}}{d\Omega dE_f} + \frac{d^2\sigma_{incoh}}{d\Omega dE_f} \tag{1.19}$$

The coherent scattering results in phenomena such as elastic Bragg scattering and inelastic phonon scattering. The incoherent scattering results in a spatially isotropic background with an energy dependence characteristic of vibrational energies. This contribution is especially dominant in hydrogen containing compounds, and thus is particularly problematic for many molecular nanomagnets as they frequently contain large amounts of hydrogen-containing organic ligands. Replacing the hydrogen with deuterium is one way to alleviate this problem. However, deuteration is frequently not feasible, either due to economic or synthetic reasons and so separating this component from the other scattering behaviours is of the upmost importance.

It can be shown that the cross-section for coherent nuclear scattering can be expressed as

$$\left(\frac{d^2\sigma}{d\Omega d\omega}\right)_{coh} = \frac{N(2\pi)^3}{V_0} |F_N(Q)|^2 \delta(Q - \tau)\delta(\hbar\omega) \tag{1.20}$$

Where V_0 is the volume of the unit cell of the crystal, N is the number of unit cells in the crystal and τ is a vector in the reciprocal lattice, thus such scattering only occurs for $Q = k - k' = \tau$ and is analogous to Bragg's law for X-ray scattering. Where the nuclear structure factor is defined as $F_N(Q) = \sum_j \bar{B}_j \exp(iQ \cdot r_j)\, exp(-W_l(Q,T))$, the sum runs over all nuclei in the unit cell at positions r_j, $\bar{B}_j$ is the scattering length and the term $exp(-W_l(Q,T))$ is the Debye-Waller factor. This is an important term that describes the reduction in intensity of Bragg peaks due to the blurring of positional order in the scattering target, resulting from thermal fluctuations. Without it we would be describing unphysical fixed atomic positions with peaked Dirac-δ functions for Bragg peaks with the form factors turning into constants.

1.5.3 Magnetic Scattering

Whilst the nuclear scattering is always present it is not the primary scattering mechanism under investigation of this thesis. Magnetic scattering is a consequence of the interaction between the magnetic moment possessed by the neutron and that of the magnetic field generated by an unpaired electron. This is described by the interaction potential $V = -\mu_n \cdot B_i$

The magnetic moment of the neutron is given by

$$\mu_n = -\gamma u_N \hat{\sigma} \tag{1.21}$$

where γ is the gyromagnetic ratio, u_N is the nuclear magneton and σ is the Pauli spin operator with eigenvalues ± 1.

The magnetic field generated by the ith unpaired electron at a distance R is expressed as

$$\boldsymbol{B}_i = -\frac{\mu_0}{4\pi} 2\mu_B \left(\nabla \times \left(\frac{\hat{s}_i \times \boldsymbol{R}}{R^3} \right) + \frac{\boldsymbol{l}_i \times \boldsymbol{R}}{R^3} \right) \tag{1.22}$$

Where s_i is the spin of the ith electron and $\boldsymbol{l}_i$ its associated orbital angular momentum. μ_B is the Bohr magneton. The first term described the magnetic field resulting from the spin contribution whereas the second component describes the field originating from the orbital angular momentum. Many transition metal ions have quenched orbital angular momentum and hence it is only necessary to consider the spin component and so the magnetic cross-section is only due to spin scattering. Whilst this assumed quenching of the orbital angular momentum is usually a fair assumption, in many cases it breaks down as we will see later in this work.

By combining the previous 3 expressions and undergoing some lengthy algebra we arrive at the following expression for the magnetic cross-section.

$$\left(\frac{d^2\sigma}{d\Omega dE_f}\right)_{mag} = (\gamma r_o)^2 \frac{k_f}{k_i}\left(\frac{g}{2}f(Q)\right)^2 exp\big(-2W(Q,T)\big)\sum_{\alpha\beta}^{x,y,z}\left(\delta_{\alpha\beta} - \frac{Q_\alpha Q_\beta}{Q^2}\right) S^{\alpha\beta}(Q,\omega) \qquad (1.23)$$

r_o is the classical electron radius, g the Landé splitting factor, $f(Q)$ is the dimensionless magnetic form factor defined as the Fourier transform of the normalised spin density associated with the magnetic ions, $\big(-2W(Q,T)\big)$ is again the Debye-Waller factor and α, β refer to the spin components.

The $\left(\delta_{\alpha\beta} - \frac{Q_\alpha Q_\beta}{Q^2}\right)$ term is particularly interesting since it tells us that the neutron is only sensitive to magnetic moments which are perpendicular to $\boldsymbol{Q}$.

$S^{\alpha\beta}(Q,\omega)$ is the dynamical spin correlation function, which is the space and time Fourier transform of the time-dependent magnetic correlation function. It contains all the information about the magnetic structure and the spin dynamics of the system under study. The determination of this term is the primary objective of an INS experiment.

$$S^{\alpha\beta}(Q,\omega) = \sum_{j,j'} e^{iQ(r_j - r_{j'})} \sum_{i,f} p_i \langle\varphi_i|\hat{S}_{j',\alpha}|\varphi_f\rangle\langle\varphi_f|\hat{S}_{j,\beta}|\varphi_i\rangle \delta(E_i - E_f + \hbar\omega) \qquad (1.24)$$

The dynamical spin correlation function obeys the principle of detailed balance such that

$$S^{\alpha\beta}(Q,-\omega) = e^{-\hbar\omega/k_B T}\, S^{\alpha\beta}(Q,\omega) \qquad (1.25)$$

Energy transfer between the neutron and sample can therefore be positive or negative, corresponding to neutron energy-loss or neutron energy-gain. The probability of this is determined by the statistical weight factor of the initial state, so that at T=0 the cross section for neutron energy gain disappears since there is no energy for the neutron to take.

One other important relation is that of the dynamical correlation function to the imaginary component of the dynamic spin susceptibility by

$$S^{\alpha\beta}(Q,\omega) = [n(\omega)+1]\frac{\chi''_{\alpha\beta}(Q,\omega)}{\pi g^2 \mu_B^2} \tag{1.26}$$

This is the fluctuation-dissipation theorem for neutrons.

1.6 Time-of-Flight Neutron Spectroscopy

In Time-of-flight (ToF) neutron spectroscopy the determination of $S(Q, \omega)$ is achieved through measuring the neutron's energy by way of its flight time over a known distance. The interaction between the neutron and sample causes a change in the flight time of the neutron and this is used to infer the energy exchanged with the sample.

ToF spectrometers come in two main categories:

- Direct geometry- where the incident energy is defined before the sample via a device such as a monochromating crystal or chopper system. The final energy is then determined by ToF between the sample and detector.
- Indirect geometry- where the sample is illuminated by a white incident beam and the incident energy is determined at the sample by the flight time. The final energy is then measured using a monochromating crystal.

The measurements in this thesis have been solely conducted using direct geometry spectrometers and so we shall limit our discussion to this type.

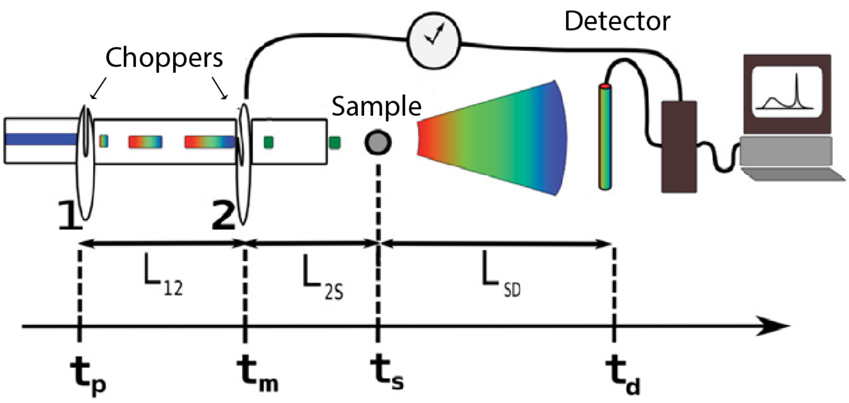

Figure 8. Standard setup for a ToF neutron spectrometer featuring choppers, sample and detector, with distances shown. Image adapated from [44].

In order to carry out this measurement it is essential that the neutron beam is monochromatic. This is achieved with a chopper system, or with a chopper system and a monochromator crystal. Then, by accurately knowing the flight distance L and the time taken to travel this distance t we can deduce the neutron's velocity through

$$v_n = \frac{L}{t} \tag{1.27}$$

$$v_i = \frac{L_{12}}{(t_m - t_p)} = \frac{L_{12} + L_{2S}}{(t_s - t_p)} \tag{1.28}$$

$$v_f = \frac{L_{SD}}{(t_d - t_s)} \tag{1.29}$$

it follows that

$$t_s = t_p + \frac{L_{12} + L_{2S}}{v_i} = \left(1 + \frac{L_{2S}}{L_{12}}\right) t_m - \left(\frac{L_{2S}}{L_{12}}\right) t_p \tag{1.30}$$

The energy transfer can therefore be expressed as a function of the travel time

$$\hbar\omega = \frac{1}{2} m_n \left(v_i^2 - v_f^2\right) \tag{1.31}$$

$$= \frac{1}{2} m_n \left[\frac{L_{12}^2}{\left(t_m - t_p\right)^2} - \frac{L_{SD}^2}{\left(t_d - \left(1 + \frac{L_{2S}}{L_{12}}\right) t_m + \left(\frac{L_{2S}}{L_{12}}\right) t_p\right)^2} \right] \tag{1.32}$$

At a pulsed source there is already an inherent time structure associated with the delivery of the neutrons to the instruments. At steady state sources however the chopper systems are used to provide the pulse structure[44].

1.6.1 Choppers

For IN5 at the Institut Laue-Langevin (ILL), the process starts with the pulsing choppers (P1 and P2) creating polychromatic neutron bursts from the near Maxwellian distribution of neutrons. The polychromatic bursts then go through a contaminant order chopper, which is a single chopper to remove harmonics from the large bandwidth arising from the pulsing choppers (CO). A frame overlap chopper is then used to prevent the overlapping of scattered neutrons from successive bursts by suppressing some of the pulses (FO). Finally a pair of counter-rotating choppers selects a narrow wavelength band from the bursts (M1 and M2)[45].

A further function of the chopper system is to select the energy resolution. A higher frequency chopping operation will produce shorter pulses leading to a narrower wavelength band and a higher precision in the measurement of time and thus energy. There is a trade-off however, since the higher the constraint on the resolution the lower the flux and therefore completing an experiment with a good enough statistic to obtain useful data in the beamtime generally allocated will not be reasonable[46]. The figure overleaf shows a distance *vs* time diagram of IN5.

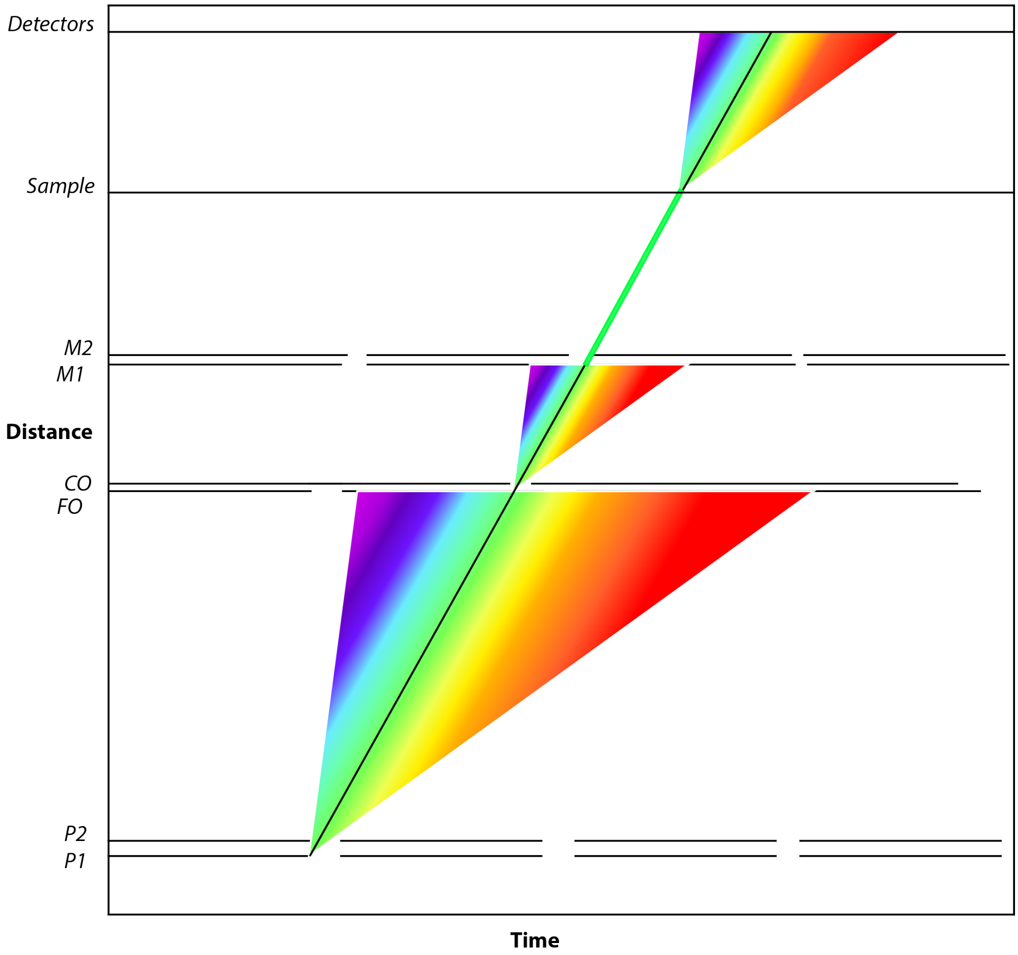
Detectors
Sample
M2
M1
Distance
CO
FO
P2
P1
Time

Figure 9. Distance *vs* time diagram for the chopper set up, sample and detectors on the ToF spectrometer IN5 at the Institut Laue-Langevin.

1.6.2 Accessible Regions in (Q,E) Space

The accessible region depends on the choice of incident energy and also on the placement of the detectors.

This kinematic range is expressed as

$$Q^2 = k_i^2 + k_f^2 - 2k_i k_f \cos\phi \tag{1.33}$$

By converting wavevectors to energies this can be rewritten as

$$\frac{\hbar^2 Q^2}{2m} = E_i + E_f - 2\sqrt{E_i E_f} \cos\phi \qquad (1.34)$$

which for direct geometry

$$\frac{\hbar^2 Q^2}{2m} = 2E_i - \hbar\omega - 2\sqrt{E_i(E_i - \hbar\omega)} \cos\phi \qquad (1.35)$$

A decrease in the incident energy results in an increase in the resolution, which is a direct consequence of the contraction of the phase space (Q, E)[46].

1.6.3 Single Crystal INS

Most INS experiments on molecular nanomagnets have probed powder samples and whilst they are synthetically easier and large amounts of information can be obtained, it is not possible to extract the full information on the spin-spin dynamical correlation functions. In a powder, information on the modulus of Q is extracted from the scattering cross section and so direct information on the internal spin structure becomes limited since it depends only on the distances between the magnetic ions. This orientation average is valuable, but if high quality single crystals can be provided then INS has the potential to deliver a wealth of additional information, as the INS intensity is now no longer just dependent on the magnitude of Q but also on its orientation with respect to the sample[47,48].

By using single crystals, position sensitive detectors (which record the neutron arrival position in a three-dimensional coordinate space) and a multi-orientation approach it is possible to obtain a full map of the phase space (Q_x, Q_y, Q_z, E) with measurements typically taken in 1 degree increments of the sample rotation and then stitched together using purpose built software such as Horace to obtain a vast data set describing the full 4D space[49].

For a direct geometry spectrometer, k_i remains in a fixed direction with respect to the sample orientation. The component of Q that is parallel to k_i remains fixed to ToF rather than detector position and so a “Q-scan” produces a curved path for each sample orientation[50].

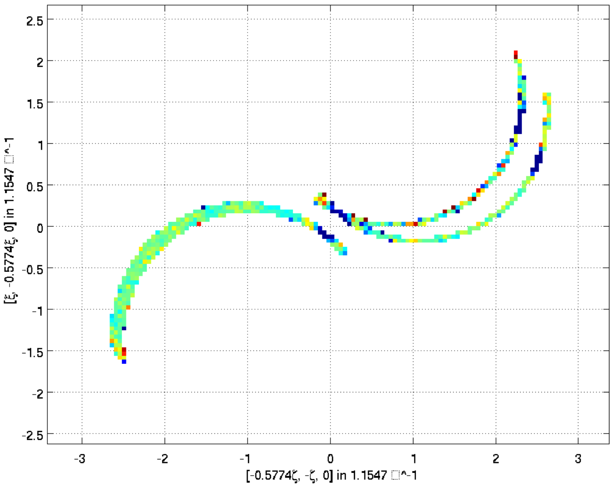

Figure 10. Several scans taken using IN5 of a molecular nanomagnet measured at different rotation angles in ToF.

Thus rotating steadily around the axis of the sample holder and concatenating the spectral runs can allow the assembly of complete maps containing information from the full 360 degree rotation. With the modern capabilities of ToF spectrometers, this type of experiment, whilst still time consuming is becoming a more routine procedure[51,52].

The extraction of such a huge amount of information greatly assists in the determination of a physical model characterising the system. For instance simple INS, EPR spectra and common susceptibility curves may be fitted with many mathematical functions with only the experimenter deciphering the likely mathematical result that is of physical consequence, but in fitting the four-dimensional space one can be more confident that the model is univocal since the mathematical complexity to describe such an object is of a higher order due to the vectorial Q-dependence. This quantity of information is so large that it has even been demonstrated possible to determine the full pattern of real-space two-spin dynamical correlation functions[47].

For a molecular nanomagnet with uniaxial anisotropy as $T \rightarrow 0$

$$S(Q,\omega) \propto \sum_{\alpha=x,y,z}\left(1-\frac{Q_\alpha^2}{Q^2}\right)\sum_p \sum_{d\geq d'} F_d(Q)F_{d'}(Q)\cos(Q\cdot R_{dd'}) \times \langle 0|\hat{s}_{\alpha,d}|p\rangle\langle p|\hat{s}_{\alpha,d'}|0\rangle\delta(\omega-\omega_p) \tag{1.38}$$

Where 0 and p are ground and excited eigenstates respectively. $F_d(Q)$ is the form factor for the *d*th ion and $\omega_p = \frac{\hbar}{p}$

This formula can be rewritten in terms of the T=0 dynamical correlation functions[47]

$$\langle s_\alpha(d,t)s_\alpha(d',0)\rangle = \sum_p \langle 0|s_\alpha(d)|p\rangle\langle p|s_\alpha(d')|0\rangle e^{-i\omega_p t} \tag{1.39}$$

ω_p can be read out directly from the magnetic transitions and $\langle 0|s_\alpha(d)|p\rangle\langle p|s_\alpha(d')|0\rangle$ the unknown Fourier components of the spin pair correlations are extracted for each of these excitations by fitting the general scattering cross section above to the Q-dependence of each selected magnetic peak. The dynamical correlation functions are embedded with the information describing the low-temperature spin dynamics which can be visualised by exploiting their relation to linear response functions[47].

1.6.4 Data Cleaning

To separate the magnetic peak from the non-magnetic background, the peak is fitted with a Guassian and some contribution for the local background. This fitting is then carried out q by q over every q point. This allows one to separate the magnetic behavior from the non-magnetic, providing the peak position can still be observed in the spectrum and is not completely buried by the non-magnetic character. In addition to this, the size and irregular macroscopic shape of the single crystals used in the experiments also result in a self-shielding contribution that needs to be corrected for. First the projection of the self-shielding on the non-magnetic behavior in the spectrum is taken and is then subsequently removed from the neighboring magnetic peak. Information from the magnetic features that is buried under a sizable phonon contribution can still be accessed by carefully completing the above cleaning procedures.

1.6.5 Advantages of ToF Neutron Spectroscopy

The major advantage for ToF spectroscopy is that we are able to survey large regions of phase space since the detectors simultaneously collect over a wide range of values of the scattered neutron energy (Q, E). This allows one to have a detailed understanding of the chemical physics in materials, to a degree not usually possible with other spectroscopic techniques. Indeed the full range of energy transfers spanning both the neutron energy loss and energy gain side are recorded in a single pulse allowing an enormous amount of information to be gathered over the course of an experiment[53].

In the broader sense INS transitions obey the selection rules $\Delta S = 0$ and ± 1 with $\Delta M_S = 0$ and ± 1. This is similar to other traditional spectroscopies used in the field such as EPR, with the addition of the $\Delta S = \pm 1$ selection rule, allowing us to go further than just probing the splitting of individual spin multiplets. Crucially we also have the momentum exchange with the sample, which gives us information on the nature of the wavefunctions involved. Importantly this can be obtained without having to apply an external magnetic field on the sample and can be collected over a wide temperature range, something that more traditionally used spectroscopies in the field, such as EPR, struggle to achieve[54,55].

1.7 Overview of Recent Research

Excellent overviews of INS research in molecular magnetism can be found stretching back to the earliest application of the technique to these systems, which should be consulted for a thorough overview of previous experiments [22,40,54,56]. However in recent years several more important experiments have taken place using INS spectroscopy reflecting both the application of new neutron technology to molecular nanomagnets and also the important physical results they permit the user to obtain.

The AMATERAS ToF spectrometer at the J-PARC facility has been used to probe a Tb-Cu dinuclear single-molecule magnet. The instrument is now capable of repetition rate multiplication (RRM) and thus the team was able to measure over four incident neutron energies and wave vectors at the same time, a development which allows for a much larger collection of data over a period of time than was previously possible. The different ranges of S(Q,w) probed are shown below in figure 11. Magnetic excitations were observed at 1.7 and 12.3 meV with the transition energy of 1.7 meV originating from the exchange coupling and the excitation at 12.3 meV corresponding to the transition between the J multiplets of the Tb 3+ moment. With the available resolution ($\frac{\Delta E}{E} \sim 1\%$) they were also able to resolve the splitting of the 1.7 meV excitation arising from the hyperfine interaction of the Cu and Tb[57].

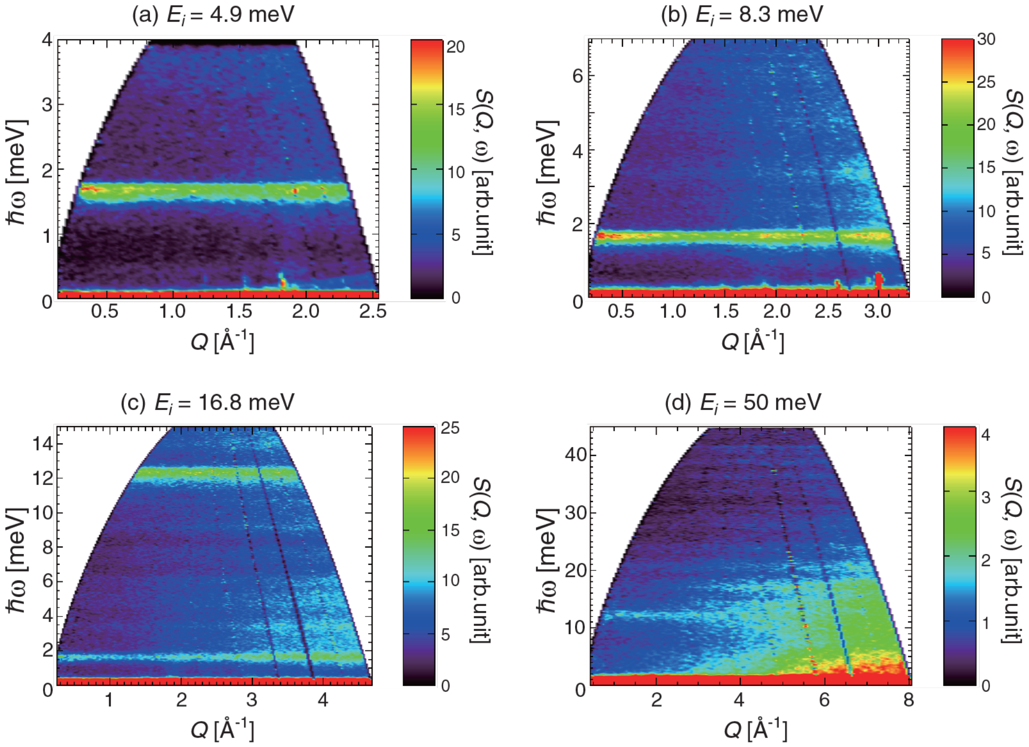

Figure 11. Simultaneously obtained maps of S(Q,w) for a Tb-Cu molecular nanomagnet, with incident neutron energy a) 4.9 b) 8.3, c) 16.8, d) 50 meV [57].

The inclusion of RRM on some modern spectrometers is an important advancement that permits the experimenter to potentially obtain multiple useful measurements simultaneously and is something that will be exploited in some of the measurements in this work where possible, such as on the cold-neutron spectrometer LET.

INS investigations of molecular nanomagnets containing purely 4f ions have also proved popular in recent years with a number of important studies. Pederson *et al.* have carried out a detailed investigation into the change in magnetic properties through the variation of peripheral ligand. 3 Er(III) single ion magnets were prepared with the peripheral ligands shown below.

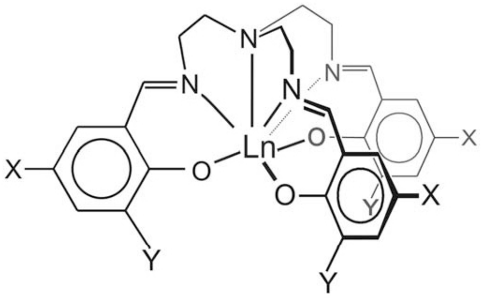

Figure 12. Schematic of the lanthanide compounds investigated 1-3. Where for 1. X=Y=H 2. X=CH_3 Y=I and 3. X=Cl and Y=H

The magnetic properties were investigated with a combination of magnetometry, EPR and INS. The INS measurements were undertaken on the IN4 and IN5 ToF spectrometers at the ILL. By probing the well-separated ground $^4I_{15/2}$ multiplet it was found that surprisingly the peripheral ligands had a dramatic effect on the magnetic properties of the molecules. These were well accounted for by their state-of-the-art *ab initio* calculations. In the wider context their results are particularly interesting since the demonstration that a variation of environment relatively far from the metal centres can have a profound effect on the magnetic properties is encouraging for those working on grafting molecular nanomagnets on surfaces, and thus motivates such a methodology towards chemical tuning of the magnetic properties[58].

In recent years important experiments have also taken place on antiferromagnetic rings. With the application of the full capabilities of modern position sensitive detectors and accompanying sample rotation of a single crystal, a benchmark $Cr_8[O_2CC(CD_3)_3]_{16}$ single crystal was used to extract the full 4D phase space. Comparatively the use of polycrystalline powders only allows one to measure the modulus of Q from the scattering cross section, whereas single crystals allow the vectorial dependence to be obtained and so the information embedded on the correlations is retained. By measuring a sufficient volume of this phase space one can extract the full pattern of real-space dynamical two-spin correlation functions. Embedded within the Fourier components of the dynamic spin correlations is information on the low temperature dynamics which can then be visualised by exploiting their relationship with linear response functions[47].

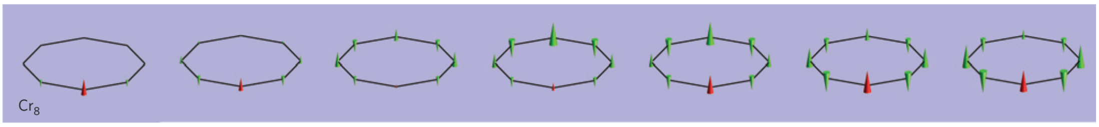

Figure 13. Visualisation of the provoking of the spin propagation in the Cr_8 ring

With the huge amount of information extracted it is possible to obtain this information without passing through a model spin Hamiltonian. This is particularly promising for large systems where the Hilbert space is too large for practical diagonalisation.

Intricate INS measurements have not just been reserved to even-membered antiferromagnetic rings and a study on odd-membered chromium-based antiferromagnetic rings by Baker *et al.* has obtained a detailed characterisation of the magnetic properties of a Cr_8Ni nanomagnet. This was achieved by using 3 separate INS spectrometers (namely IN5, Focus and IRIS). In characterising these properties the molecule is found to posses an S=0 ground state with the addition of the Ni(II) ion weakening the $J_{cr\text{-}cr}$ by around 10% compared to the even-membered homometallic Cr_8 ring. This occurs due to the opening up of the ring by the insertion of this extra ion and so the geometry of the bridging ligands is altered, thus reducing the Cr-Cr exchange interactions. The isotropic exchange parameters found to fit the data were $J_{cr\text{-}cr} = 1.32$ meV and $J_{cr\text{-}Ni} = 3.22$ for which the latter is strong enough to stabilise the ground state as an S=0 and describe the molecule in the context of a valence band solid model[59].

As well as inelastic neutron scattering, neutron diffraction experiments are also becoming more frequent in this field. One particularly impressive experiment has been carried out on another related molecular wheel, by Guidi *et al.*[60]. In this experiment polarized neutron diffraction was employed to directly observe finite size effects and a noncollinear spin distribution around an even-numbered antiferromagnetic spin chain Cr_8Cd with S=3/2. First the nuclear structure was studied using the D19 thermal neutron diffractometer at the ILL, then the PND experiment was carried out on the D3 instrument at the same facility at 1.6 K and under a field of 4.6 T. This was done to maximize the energy gap between the field enforced S=1 ground state and next nearest excited state, with a second measurement also taken at 9 T. From these measurements the experimental team showed that the spin density accumulates at the edges of the open ring with the distribution unaffected by the increase in magnetic field. The spins are arranged in a non-collinear arrangement with respect to the field as is predicted from the classical model of spin chains put forward by Lounis *et al.*[61]. This contrasts with that for an odd-membered spin chain where the spins align with the field. Such an understanding of the spin orientation can give an insight into spin transport and manipulation in potential spintronic materials, which should prove vital for their implementation in future devices. Furthermore the comparison to the spin arrangements in other spin chains represents fertile ground for further investigation.

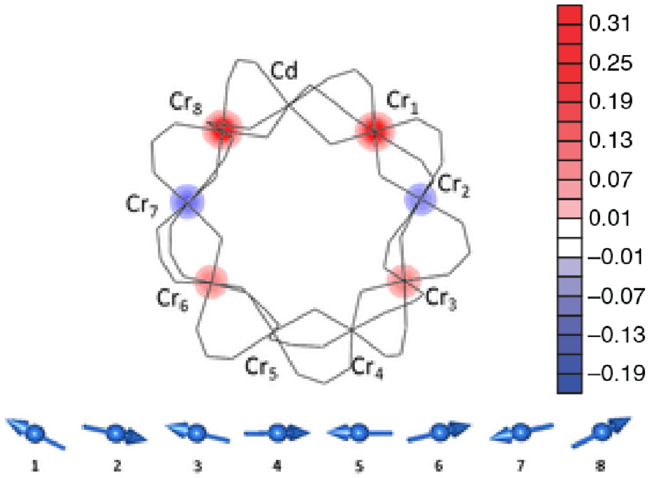
Cd
Cr₁
Cr₂
Cr₃
Cr₄
Cr₅
Cr₆
Cr₇
Cr₈
0.31
0.25
0.19
0.13
0.07
0.01
−0.01
−0.07
−0.13
−0.19
1
2
3
4
5
6
7
8

Figure 14. Spin density and configuration obtained from D3 experiment on Cr_7Cd adapted from[60].

Chapter 2 INS Spectroscopy of Molecular Nanomagnet Dimers

2.1 Background

Exchange coupled binuclear clusters were at the heart of some of the earliest applications of INS to what would go on to be referred to as molecular nanomagnets. These pioneering works by Güdel and Furrer in the late 1970s were motivated by the scaled down nature of these systems in comparison to bulk magnetic lattice[62]. These were very important investigations since the simplified nature was the necessary starting point, due to the comparatively meagre computational power available at the time. From these works they were able to chararcterise the exchange parameter between metal centres and then gradually scale up to include more complex exchange arrangements. This expanded process has been nurtured into an area capable of extracting vast amounts of information, which will be demonstrated later on.

Whilst the size of the molecules and the number of spin centres in these investigations have increased, the size of the active components in our technology has decreased to a point where molecular materials are now a significant focal point of contemporary research in an attempt to avoid the tailing off of this miniaturisation trend. In addition to this, the increasing application of technology based not just off the charge degree of freedom but also the spin (spintronic) has approached a crossroad of these two areas, forging the field of molecular spintronics. Molecular nanomagnets can clearly be seen as materials with tremendous potential to play a role in this emerging area.

Recently the Kondo effect has been observed in a binuclear metal system with two spins, namely $[(M(hfacac)_2)_2(bpym)]$ $M=Ni,Co$[63]. Analogous to how Güdel and Furrer started out, we begin by providing a magnetic characterisation of these two binuclear systems.

Journal Name

ARTICLE

Magnetic Properties of Kondo Effect Exhibiting Dimers Probed by Inelastic Neutron Scattering

Received 00th January 20xx,
Accepted 00th January 20xx

DOI: 10.1039/x0xx00000x

www.rsc.org/

S. Ansbro[a,b], A. Chiesa[c,d], E. M. Pineda[e], W. Yu[e,f], J. Ollivier[b], H. Mutka[b], M. Ruben[e]

The understanding and physical characterisation of molecular magnetic materials is one of the most important steps towards the integration of such materials in hybrid spintronic devices. Herein, the magnetic properties of two dinuclear complexes, namely [(M(hfacac)$_2$)$_2$(bpym)] (where M = Ni^{2+}, **1**; Co^{2+},**2**) are described. These are model systems that could constitute fundamental units of future spintronic devices. Exploiting the highly sensitive IN5 Cold inelastic neutron scattering spectrometer, we are able to full obtain the microscopic spin Hamiltonian parameters for both **1** and **2**. The close agreement between the magnetic susceptibility data and the inelastic neutron scattering spectra allows us to gain a deeper insight into the spin dynamics of these molecules.

Introduction

Molecular nanomagnets (MNMs) are finite clusters of transition metal ions, whose spins are coupled by exchange interactions and are magnetically isolated from neighbouring ions by the surrounding bulky ligands. Thanks to their relatively small size, and their zero dimensional characteristics, they offer a remarkable opportunity to study fundamental physical phenomena of both quantum and classical nature.[1-7] Moreover, the high degree of achieved chemical control makes these systems promising for many different applications, such as quantum-information processing[8-11], high-density data storage[12,13] or low-temperature magnetic refrigeration[14,15].

In the last few years, important steps have been made in the field of molecular electronics, where the challenge to construct certain electrical or spintronic devices on a molecular scale is addressed by the assembly of specific molecules tailored for specific applications. In particular, molecule-scaled diodes, transistors and memories were realised[16-22] and the magnetoresistance effect was observed on single molecules[23,24]. In this respect, di-nuclear magnetic complexes are the optimal test-beds to understand the transport behaviour of MNMs. Indeed, magnetic intra-molecular as well as molecular-substrate interactions can be finely tuned by chemical engineering, thus allowing us to explore new features arising from the competition between these couplings.[25,26] Recently a molecular nanomagnet dimer of chemical formula [(Ni(hfacac)$_2$)$_2$(bpym)] was deposited onto a copper surface where it was demonstrated to display the Kondo effect for certain adsorption types, with a relatively high Kondo temperature of 10 K.[27]

In turn, the characterisation of the magnetic properties of these complexes is essential to gain a deeper insight in their dynamics, thus paving the way for the rational design of future molecular devices. Indeed, the understanding of the structure-properties correlations is of utmost importance to establish the design criteria for better performing molecular systems and their optimal integration in spintronic devices.

In this context, several characterisation techniques have been used for the understanding of the magnetic and spectroscopic properties of MNMs[1] ranging from conventional SQUID, μ-SQUID arrays, to spectroscopic techniques such Nuclear Magnetic Resonance (NMR), Electron Paramagnetic Resonance (EPR) and Inelastic neutron scattering (INS). INS is one of the best techniques available to characterise the microscopic magnetic interactions of MNMs. It allows the precise determination of the parameters that define a spin Hamiltonian. In addition, rapid developments in spectrometer technology make it possible to measure increasingly smaller samples, which is particularly useful where the chemical synthesis yields low quantities of product. Herein we report the synthesis, magnetic properties and the INS spectroscopic characteristics of two MNMs with formula [(M(hfacac)$_2$)$_2$(bpym)] (where M = Ni^{2+}, **1,** Co^{2+}, **2**;) (Fig. 1).

---

[a] *School of Chemistry, The University of Manchester, Oxford Road, Manchester, UK, M13 9PL.*
[b] *Institut Laue-Langevin, 71 Avenue des Martyrs CS 20156, Grenoble, France.*
[c] *Institute for Advanced Simulation, Forschungszentrum Jülich, Germany.*
[d] *Dipartimento di Scienze Matematiche, Fisiche e Informatiche University of Parma, 43124 Parma, Italy.*
[e] *Institute of Nanotechnology (INT), Karlsruhe Institute of technology (KIT), Hermann-von-Helmholtz-Platz 1, D-76344 Eggenstein-Leopoldshafen, Germany.*
[f] *Zhejiang Provincial Key Laboratory for Chemical & Biochemical Processing Technology of Farm Products, School of Biological and Chemical Engineering, Zhejiang University of Schience and Technology, No. 318 Liuhe Road, Hangzhou 310023 China.*

† Footnotes relating to the title and/or authors should appear here.

Electronic Supplementary Information (ESI) available: [details of any supplementary information available should be included here]. See DOI: 10.1039/x0xx00000x

INS studies were carried out using the cold neutron spectrometer IN5 at the Institut Laue-Langevin[28], allowing us to directly probe the low-energy spin dynamics of the complexes.

Results and discussions

Compounds **1** and **2** were obtained by reacting one equivalent of bipyrimidine ligand with two equivalents of the M(hfacac)$_2$ (M = Ni^{2+}, Co^{2+}; hfacac = hexafluoroacetylacetonate) in a mixture of ethanol water. (See Si for details). Single crystal studies reveal the complexes to be two neutral dinuclear systems with formula [(Me(hfacac)$_2$)$_2$ (bpym)] (Fig. 1). Both complexes crystallise in the monoclinic *P21/c* space group, with the entire molecule in the asymmetric unit. In the structure, each transition metal centre, with an N_2O_4 coordination sphere, possesses a slightly symmetric octahedral environment (with CShM values of 0.247 and 0.326 for both Ni^{2+} ions in **1** and CShM values of 0.402 and 0.508 for both Co^{2+} ions in **2** respectively). Interestingly, compound **1** and **2** are mirror images of each other.

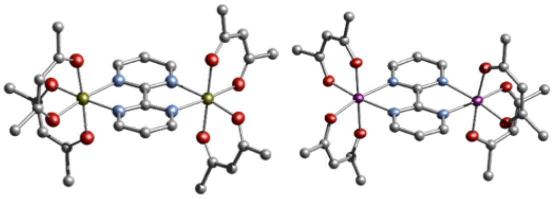

Figure 1. Crystals structure of **1** (left) and **2** (right). As observed, both complexes are mirror images of each other. Colour code: C, grey; N, cyan; O, red; Co, purple and Ni, green.

The octahedral sites show very similar M-N and M-O distances: For **1**, the Ni···N distances vary from 2.087(3) to 2.113(3) Å whilst for **2**, the Co···N distances range from 2.134(3) to 2.162(3) Å and the Co···O distances are between 2.036(2) to 2.059(2) Å Due to the slightly longer Co···N distances, a longer M···M distance is found for **2** with Co···Co of 5.7268(8) Å, compared to **1** where a Ni···Ni of 6.603(3) Å distance is observed.

We begin our investigation of the magnetic properties of **1** and **2**, firstly exploring the temperature dependent static magnetic susceptibility behaviour $\chi_M(T)$ (where χ_M is the molar magnetic susceptibility), by measuring powdered samples under an applied field of 0.1 T. Compound **1** shows a room temperature $\chi_M T(T)$ of 2.04 cm^3 mol^{-1} K. $\chi_M T(T)$ stays practically constant with decreasing temperatures. This profile is observed up to ca. 100 K, when it gradually (until about 40 K) drops to zero. Likewise, the $\chi_M(T)$ shows a maximum at approximately 24 K. This is indicative of the antiferromagnetic exchange between the two Ni centres. A similar trend is observed in Compound **2** which shows a room temperature $\chi_M T$ value of 5.41 cm^3 mol^{-1} K. Upon cooling the $\chi_M T(T)$ declines smoothly up to approximately 40 K, where it sharply declines to a $\chi_M T$*(see Si for details)* value of 0.37 cm^3 mol^{-1} K at 2 K. Inspection of the $\chi_M(T)$ plot shows at ca. 6.8 K, which decreases upon lowering temperatures. This maximum can again be ascribed to antiferromagnetic exchange operating within the metal Co^{2+} centres.

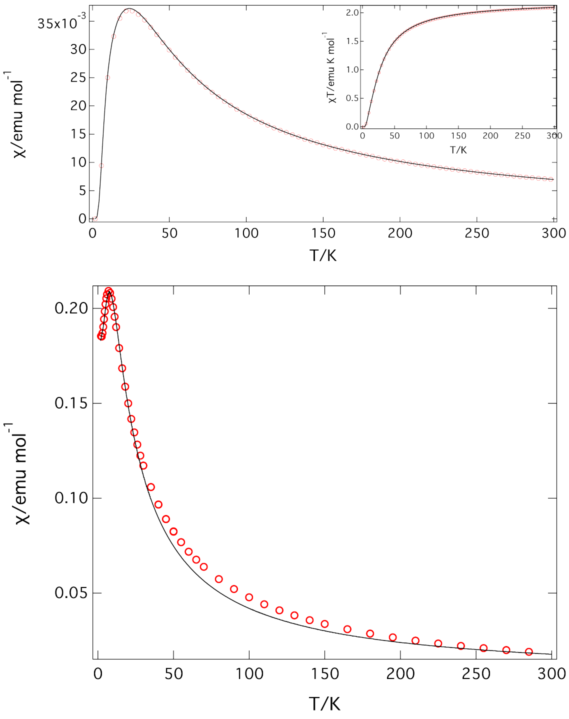

Figure 2. (a) shows the susceptibility curves for [(Ni(hfacac)2)2(bpym)] (top) and [(Co(hfacac)2)2(bpym)] (bottom) with measured (black) and simulated (red)with best fits employing Hamiltonian (1) and with the parameters described in the text.

INS was then used to accurately determine the exchange and zero-field splitting parameters that define the effective spin Hamiltonian of the system. The spectra (intensity versus energy transfer) were measured on 0.1 g polycrystalline powders of both samples. Momentum transfers have also been examined by integrating over the energy range corresponding to each magnetic transition, allowing us to confirm the structure of the eigenstates involved in each transition. Figure 3 shows INS spectra for **1** measured at three different temperatures, with incident neutron wavelength 4.8 Å, corresponding to a resolution of 90 μeV. At low temperature, three peaks are clearly distinguishable, corresponding to inter-multiplet transitions between the ground state singlet and the first excited triplet (split by anisotropy).

The data have been fitted using the microscopic spin Hamiltonian

$$\hat{H} = J\boldsymbol{s}_1 \cdot \boldsymbol{s}_2 + d\sum_{i=1}^{2} s_{zi}^2 + e\sum_{i=1}^{2}\left(s_{xi}^2 - s_{yi}^2\right)$$

where i labels the two magnetic ions, J is the anti-ferromagnetic isotropic exchange interaction, while d and e model axial and rhombic zero-field splitting anisotropy. Since the two ions are essentially related by an inversion centre, we have modelled them with the same spin Hamiltonian parameters.

In the limit in which isotropic exchange is the leading interaction, the value of J can be directly extracted from the position of the central peak (ii), while the positions of peaks i and iii are approximately given by $J \pm d, e$. Numerical simulations of the scattered cross-section lead to the refined parameters J = 2.026 meV, d=0.319 meV and a high e=0.10 meV.

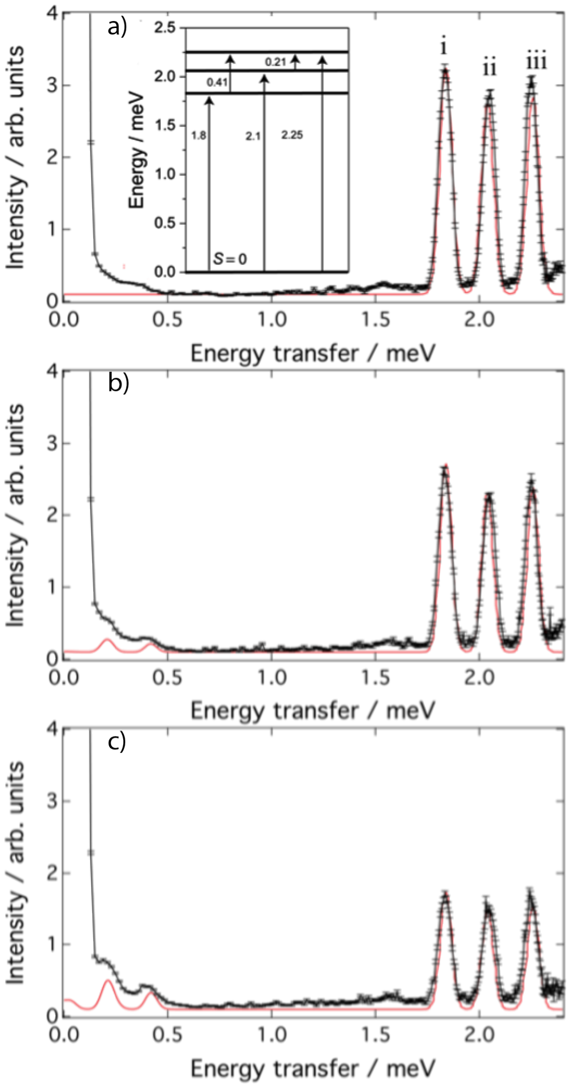

Figure 3. Energy spectra for **1** with a, b and c showing spectra at 1.6, 10 and 20 K respectively, measured (black) and simulated (red).

The extracted Q-dependence for the three main peaks is shown aside in figure 4.

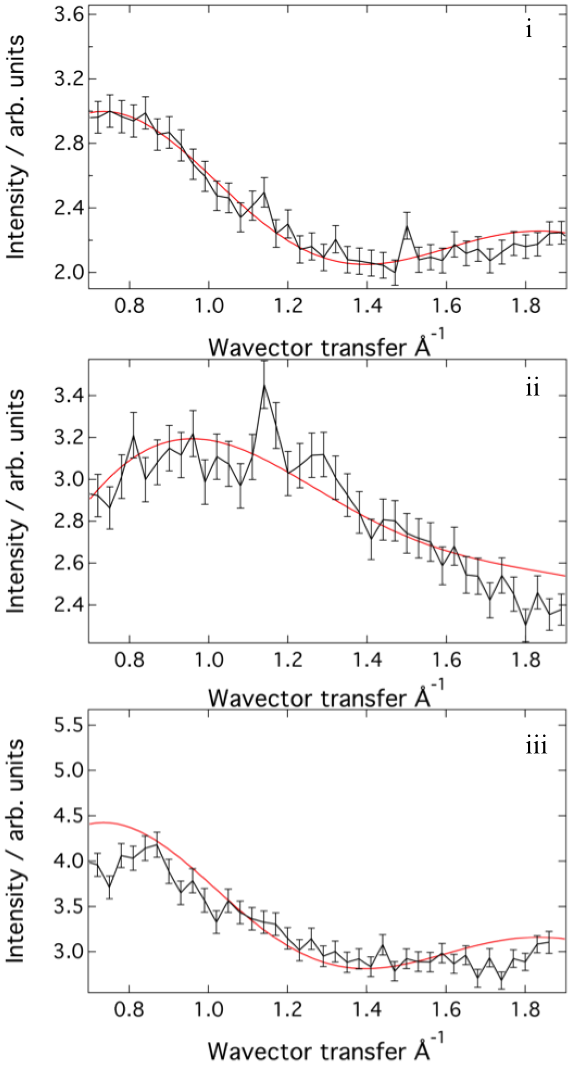

Figure 4. Q-dependence for the [(Ni(hfacac)$_2$)$_2$(bpym)] dimer with i, ii and iii showing the Q-dependence of the peaks at 1.8, 2.1 and 2.3 meV, measured (black) and simulated (red).

The reliability of these parameters is then reinforced by the Q-dependence of the scattered intensity, which also gives important information about the orientation of the anisotropy axes. Indeed, I(Q) data can only be reproduced by assuming the z-axis is perpendicular to the Ni-Ni axis, which in our model is positioned along the x-axis (intermediate anisotropy axis). Conversely, the sign of d cannot be determined from the data, but our DFT calculations[29] indicate $d > 0$.

Moreover, the reported parameters also finely reproduce the magnetometry data shown in figure 2, where an isotropic g=2.10 is found to complete the fit.

The Co dimer spectrum collected at 1.5 K using a wavelength of 4.8 Å is shown overleaf in figure 5. Many low-energy excitations can be distinguished, whose interpretation is somewhat more complicated and requires the following spin Hamiltonian:

$$\widehat{H} = \sum_{\alpha=x,y,z} J_\alpha s_{\alpha 1} s_{\alpha 2} + d \sum_{i=1}^{2} s_{zi}^2 + e \sum_{i=1}^{2} \left(s_{xi}^2 - s_{yi}^2\right)$$

in which we have included an anisotropic-exchange term.

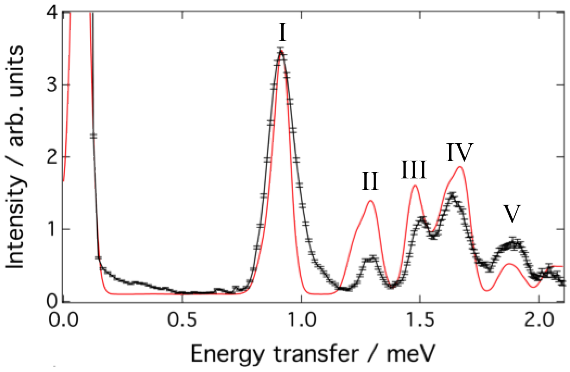

Figure 5. INS spectra for **2** at 1.6K with measured (black) and simulated (red)

Each Co(ii) ion is its high-spin (d^7, s=3/2) state. From the best fit we find that the two S=3/2 spins are antiferromagnetically coupled to each other (in agreement with susceptibility measurements) through the anisotropic exchange tensor of J_x=0.35 meV, J_y=0.23 meV and J_z=0.14 meV. In addition to this, an axial anisotropy of 0.48 meV and a rhombic anisotropy of -0.15 meV are required to reproduce the general positions of the low energy peaks. These parameters are also sufficient to describe the general form of the Q-dependence well (shown in figure 6 for peak I). It is important to note that even if I(Q) is less sensitive than the energy spectrum to small changes in all of the above parameters, it critically depends on the orientation of the anisotropy axes, which are in agreement with those found for the iso-structural Ni_2 complex. Further details on the Q-dependence can be found in the supplementary information.

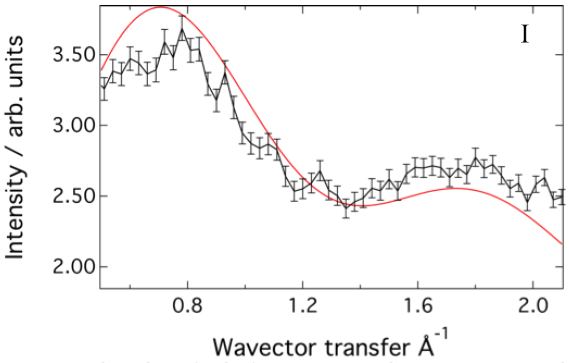

Figure 6. Q-dependence for the first transition in the **2** spectra, measured (black) and simulated (red)

The simulation of the Q-dependence for the **I** transition in the **2** INS spectra is in good agreement with the experimental measurement. This transition corresponds to an intermultiplet transition from the ground state singlet to the second level of the first excited multiplet, the structure of the eigenstates are complex due to the competing order of the exchange and anisotropy terms.

The susceptibility measurements for the Co dimer that are shown in figure 2 and are in good agreement with the simulations using the parameters obtained from the INS, an average g value of 2.06 and a temperature independent term of $5x10^{-3}$ emu mol^{-1} This is crucial to model the high temperature behaviour of χM, which deviates from that obtained with a spin-only model due to the presence of excited states arising from the split orbital ground triplet.

Conclusions

We have used INS in combination with SQUID magnetometry to obtain the microscopic spin Hamiltonian parameters for a set of binuclear molecular nanomagnet complexes. For both compounds, we obtain a very good agreement between simulations and experimental data. The measurement of the Q-dependence has been particularly useful to determine the orientation of the anisotropy axes in both compounds. In a more general perspective these measurements on relatively small quantities of sample are promising for the development of molecular electronic devises, where frequently the chemical yield of the synthesis is small. Systems such as these dimers provide excellent models for gaining crucial insights into quantum transport properties through molecular junctions, as well as the nature of the Kondo effect when they are deposited onto metallic surfaces. The ability of INS to provide a characterisation of the magnetic properties of these systems means it will have a pivotal role to play in the development of future molecular electronic technologies.

Acknowledgements

The acknowledgements come at the end of an article after the conclusions and before the notes and references.

Notes and references

‡ Footnotes relating to the main text should appear here. These might include comments relevant to but not central to the matter under discussion, limited experimental and spectral data, and crystallographic data.

1 D. Gatteschi, R. Sessoli, and J. Villain, *Molecular Nanomagnets* (Oxford University Press, 2006).
2 M.L. Baker, T. Lancaster, A. Chiesa, G. Amoretti, P.J. Baker, C. Barker, S.J. Blundell, S. Carretta, D. Collison, H.U. Guedel, T. Guidi, E.J.L. McInnes, J.S. Moeller, H. Mutka, J. Ollivier, F.L. Pratt, P. Santini, F. Tuna, P.L. Tregenna-Piggott, I.J. Vitorica-Yrezabal, G.A. Timco, R.E.P. Winpenny, *Chem. Eur. J.* **2016**, *22*, 1779.
3 R. J. Woolfson, G. Timco, A. Chiesa, I. J. Vitorica-Yrezabal, F. Tuna, T. Guidi, E. Pavarini, P. Santini, S. Carretta, R. Winpenny, *Angew. Chem.* **2016**, *128*, 9002.
4 W. Florek, M. Antkowiak, G. Kamieniarz *Phys. Rev. B* **2015**, *94*, 224421.
5 O. Waldmann, T.C. Stamatatos, G. Christou, H.U. Güdel, I. Sheikin, H. Mutka, Phys. Rev. Lett. **2009**, *102*, 157202
6 P. Santini, S. Carretta, G. Amoretti, T. Guidi, R. Caciuffo, A. Caneschi, D. Rovai, Y. Qiu, J.R.D. Copley, *Phys. Rev. B* **2005**, *71*, 184405.
7 S. Carretta, P. Santini, G. Amoretti, T. Guidi, J.R.D. Copley, Y. Qiu, R. Caciuffo, G. Timco and R.E.P. Winpenny, *Phys Rev Lett* **2007**, *98*, 167401.
8 F. Meier, J. Levy, D. Loss, *Phys. Rev. Lett.* **2003,** *90*, 47901.
9 K. Harriman, L. Jonathan, B.Liviu Ungur, P. Diaconescu, M.Muralee *J. Am. Chem. Soc.* **2014**, *136*, 14215.
10 J. Ferrando-Soria, E.M. Pineda., A. Chiesa, A. Fernandez S. Magee, S. Carretta, P. Santini, I.J. Vitorica-Yrezabal, F. Tuna, G. Timco, E. J.L McInnes, R.E.P. Winpenny *Nat Commun* **2016**, *7*, 11377.
11 J. Ferrando-Soria, S. Magee, A. Chiesa, S. Carretta, P. Santini, I.J. Vitorica-Yrezabal, F. Tuna, G. Whitehead, S. Sproules, K. Lancaster, A-L.Barra, G. Timco, E. J.L. McInnes, R.E.P. Winpenny *Chem Chem* **2016**, *1*, 727–752.
12 D. Gatteschi and R. Sessoli, Angew. *Chem. Int. Ed.* **2003**, *42*, 268.
13 Y. Rechkemmer,F. Breitgoff,M. Van der Meer, M. Atanasov, M. Hakl, M. Orlita, P. Neugebauer, F. Neese, B. Sarkar, J. Van Slageren, *Nat. Commun.* **2016**, *7*, 10467.
14 E. Garlatti, S. Carretta, J. Schnack, G. Amoretti, and P. Santini, *Appl. Phys. Lett.* **2013**, *103*, 202410.
15 J.W. Sharples, D. Collison, E.J.L. McInnes, J. Schnack, E. Palacios, M. Evangelisti, *Nat. Commun.* **2014**, *5*, 5321.
16 J. Reichert, R. Ochs, D. Beckmann, H.B. Weber, M. Mayor, H. v. Löhneysen, *Phys. Rev. Lett.* **2002**, *88*, 176804.

17 M. Elbing, R. Ochs, M. Koentopp, M. Fischer, C. von H¨anisch, F. Weigend, F. Evers, H.B. Weber, M. Mayor, *Proc. Natl. Acad. Sci. USA* **2005**, *102*, 8815.
18 J. Park, A.N. Pasupathy, J.I. Goldsmith, C. Chang, Y. Yaish, J.R. Petta, M. Rinkoski, J.P. Sethna, H.D. Abrõna, P. L.McEuen, D.C. Ralph, *Nature* **2002**, *417*, 722.
19 S. Kubatkin, A. Danilov, M. Hjort, H. Cornil, J.-L. Brédas, N. Stuhr-Hansen, P. Hedegård, and T. Bjørnholm, *Nature* **2003**, *425*, 698.
20 E. A. Osorio, K. O'Neill, N. Stuhr-Hansen, F. Nielsen, T. Bjørnholm, H. S. J. van der Zant, *Adv. Mater.* **2007**, *19*, 281.
21 E. Lörtscher, J. W. Ciszek, J. Tour, H. Riel, *Small* **2006**, *2*, 973.
22 V. Meded, A. Bagrets, A. Arnold, F. Evers, *Small* **2009**, *5*, 2218.
23 S. Schmaus, A. Bagrets, Y. Nahas, T.K. Yamada, A. Bork, M. Bowen, E. Beaurepaire, F. Evers, and W. Wulfhekel, *Nat. Nanotechnol. 2011*, *6*, 185.
24 A. Bagrets, S. Schmaus, A. Jaafar, D. Kramczynski, T. K. Yamada, M. Alouani, W. Wulfhekel, F. Evers, *Nano Lett.* **2012**, *12*, 5131.
25 W. Liang, M. P. Shores, M Bockrath, J.R. Long, H. Park *Nature* **2002**, *417*, 725.
26 S. Wagner, F. Kisslinger, S. Ballmann, F. Schramm, R. Chanddrasekar, T. Bodenstain, O. Euhr, D. Secker, K. Fink, M. Ruben, H. Weber, *Nature Nanotechnol.* **2013**, *8*, 575.
27 L. Zhang, A. Bagrets, D. Xenioti, R. Korytár, M. Schackert, T. Miyamachi, F. Schramm, O. Fuhr, R. Chandrasekar, M. Alouani, M. Ruben, W. Wulfhekel, F. Evers, *Phys. Rev. B* **2015**, *91*, 195424.
28 J. Ollivier, H. Mutka, *Jour. Phys. Soc. Jpn* **2011**, *80*, SB003.
29 S. Carretta, A. Chiesa, E. Pavarini, in preparation.

Supplementary information

Synthesis

Solvents and reagents were of commercial grade and used without further purification. 1 and 2 were prepared by modification of published procedures.[1] Elemental analysis data were collected on an ELEMENTAR Vario Micro Cube.

A solution of 0.5 mmol 2,2'-bipyrimidine (bpm) in 10 ml of a 1:1 mixture of ethanol/water was dropped to a solution of 1 mmol M(hfacac)$_2$ (M=Co, Ni) in 15 ml of a 3:1 mixture of ethanol/water. The mixture was stirred for several hours at room temperature, after that precipitates were formed. The residual solvent was filtered and kept by -17 ºC to gain crystals. The solid was washed twice with a mixture of ethanol/water (1:1). The solid was dried at 90 ºC and X-ray diffraction quality crystals were formed by recrystallization from Et$_2$O.

[(Ni(hfacac)$_2$)$_2$(bpm)] 1: pale green crystals; yield 41%; elemental analysis calculated (%) for C28H14F24N4O8Ni2: C 30.36, H 1.27, N 5.06; found: C 30.52, H 1.18, N 5.15.

[(Co(hfacac)$_2$)$_2$(bpm)] 2: red crystals; yield 57%; elemental analysis calculated (%) for C28H14F24N4O8Co2: C 30.34, H 1.27, N 5.06; found: C 30.54, H 1.16, N 5.10.

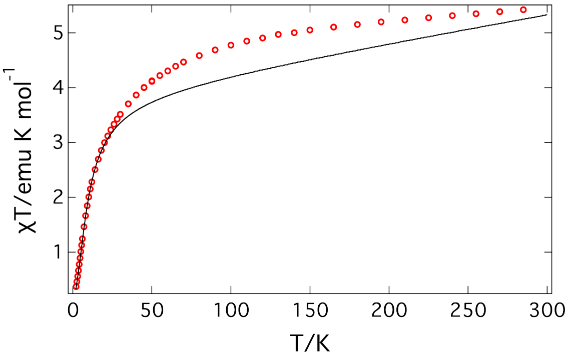

Figure 7. Susceptibility curve for compound **2,** measured (black) and simulated (red).

The deviation at high temperature is due to the lack of inclusion of the orbital moment in the model and so the model is lacking higher temperature multiplets but is sufficient for the low temperature behaviour and thus the INS measurements.

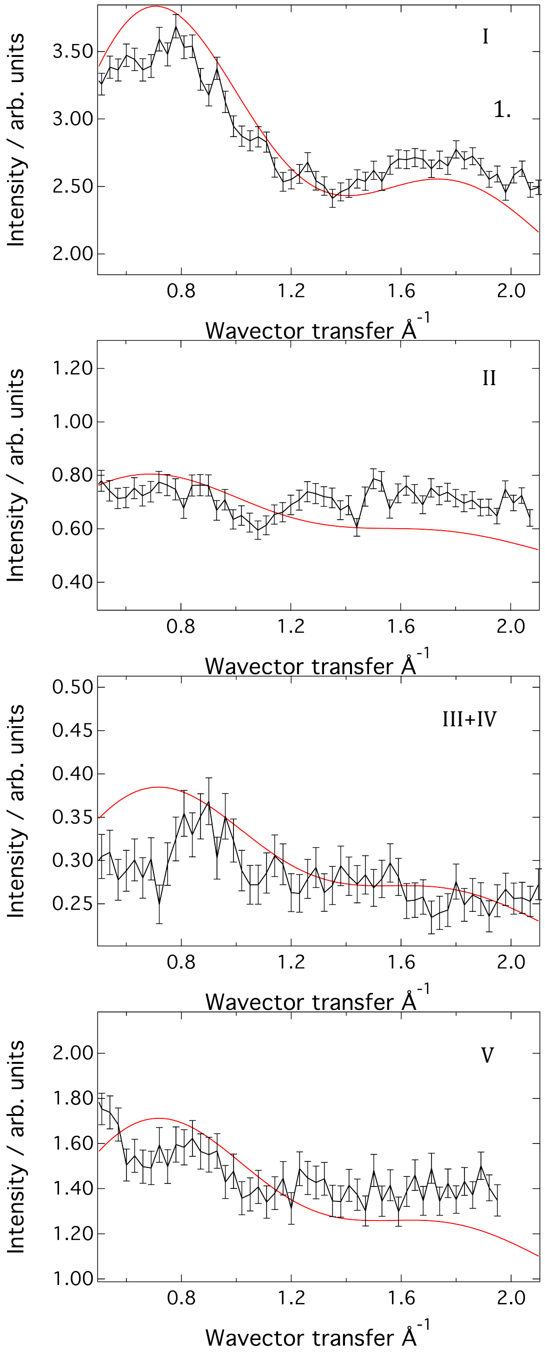

Figure 8. Q-dependence for compound **2** with corresponding peaks labelled in energy spectra, measured (black) and simulated (red).

Chapter 3 INS Study of Cr_7Co

3.1 Cr_7Co Background

To improve upon the remarkable properties of Mn_{12} two general routes have been explored. The first has been to try and exploit high spin 3*d* metals through classical coordination chemistry to obtain large total spin molecular ground states[67]. After the properties of Mn_{12} were first comprehended this avenue was immediately explored, however the complete quenching of the orbital momentum and subsequent small single-ion anisotropy has resulted in relatively meagre energy barriers to the retention of the magnetisation. A more modern approach has been to choose rare-earth ions to take advantage of their large anisotropies. However the small extension of the 4f orbitals leads to weaker exchange interactions and often prevents the construction of high total spin ground states that are well isolated from the excited states.

An alternative option is to try and combine nearly isotropic high-spin ions that are strongly exchange-coupled to very-anisotropic 3*d* ions such as Co^{2+} where the orbital angular momentum is unquenched. If the large anisotropy of an anisotropic 3*d* ion can be transmitted to the rest of the molecule, then it would open up a gateway to obtaining molecules with a large spin ground state that are also highly anisotropic.

Such an example of a molecule exists in the form of an AF molecular ring deriving from the parent compound Cr_8, this time by the addition of divalent Co to the reaction mixture it is possible to synthesise

$[Cr_7CoF_8(O_2C^tBu_{16})]$[23]. This molecule again has an S=1/2 ground state and crystallises in the I_4 space group.

The chemical versatility of the chromium based AF heterometallic rings represent wonderful opportunities to study finite exchange coupled systems and have amassed a large number of different Cr_7M rings with Ni, Co, Mn, Fe, Zn, Cd, Cu and Mg forming such examples. This results in a playground of different spin structures with different anisotropies. The rich physics displayed by these AF ring structures has led to many elegant experiments including the direct extraction of the spin dynamics in the homometallic $[Cr_8CoF_8(O_2C^tBu_{16})]$ ring[47] and represent a wonderful opportunity to analyse the controlled chemical tweaking of the underlying physics throughout these finite quantum systems.

In this work we use 4D-INS to investigate the spin dynamics in the $[Cr_7CoF_8(O_2C^tBu_{16})]$ ring to uncover how much anisotropy can be delivered into the ring through the insertion of this Cr(II) ion.

Journal Name

ARTICLE

Spin dynamics of a Cr_7Co ring probed by 4D-INS

S. Ansbro[a,b], E. Garlatti[c], A. Chiesa[c,d], T. Guidi[e], D. Albertini[c], H. Mutka[b], J. Ollivier[b], P. Santini[c], G. Amoretti[c], S. Carretta[c], G. Timco[a], I.J. Vitorica-Yrezabal[a], R.E.P. Winpenny[a].

Received 00th January 20xx,
Accepted 00th January 20xx

DOI: 10.1039/x0xx00000x

www.rsc.org/

A detailed characterisation of the magnetic properties of a Cr_7Co antiferromagnetic (AF) ring has been obtained using inelastic neutron scattering (INS). This is a model system to understand how the insertion of a highly anisotropic Co ion strongly coupled to the neighbouring Cr ions affects the spin dynamics of the molecule. The full energy and momentum transfer for the low-lying excited spin states has been accessed through single crystal 4D-INS, allowing us to obtain a univocal fit from the vast amount of information extracted. The data are also shown to be consistent with DFT calculations and in-field measurements, reinforcing the validity of the model deduced. We find an anisotropy induced splitting almost 5 times as large if compared to the parent Cr_7Mn ring, thus paving the way for a new route to increase the anisotropy barrier of molecular nanomagnets: Combine high-spin nearly isotropic ions strongly exchange-coupled to a few very-anisotropic 3d ions like Co^{2+}.

I Introduction

Molecular nanomagnets are metal-organic compounds where the metallic cores are isolated into zero-dimensional units by bulky organic ligands.[1] The AF wheel family of molecular nanomagnets is a prominent example since they are leading candidates to investigate the cross-over regime between classical and quantum physics. For example, they have been proposed as candidates for observing the quantum tunnelling of the Néel vector[2,3,] even if the exact conditions necessary for this to occur are still a subject of debate[4,5]... Of particular interest are Cr based rings. These Cr based rings derive from the substitution of one Cr(iii) ion in the parent homometallic $Cr_8[F_8(O_2C^tBu_{16})]$ wheel. This substitution changes the ground state from $S = 0$ to an $S \neq 0$ depending on the choice of ion substituted into the ring[6]. Molecules can then we synthesised with a range of different spin ground states and then their properties can be further chemically enhanced for application by additional substitutions[7]. Significant examples of these Cr based rings are Cr7Ni (S=1/2) and Cr7Cd (S=3/2) which have been selected as molecules to try and engineer for applications such as qubits[8,9] and for low temperature magnetic refrigeration respectively[10]. The tremendous potential of these substitutions have been well characterised and studied, however the substitution of Co(II) into this ring also represents yet another particularly interesting case. As well as inspecting the change in the spin dynamics (partly owing to the unquenched orbital moment) it also represents a potential pathway to generating effective SMMs, since it can satisfy the need for the strongly exchange coupled highly anisotropic molecular units required[1]. The issue with general approaches to building SMMs is that usually high spin *3d* ions such as Fe^{3+}, Mn^{2+} and Cr^{3+} are utilised to obtain a large spin ground state[11],[12]. However the small single ion anisotropies resulting from the quenching of the orbital angular momentum result in small anisotropy barriers[13]. To overcome this problem some have looked to increase this anisotropy barrier by exploiting rare-earth elements[14,15], however the small extension of the f-orbitals often makes obtaining high total spin molecular ground states difficult. In Cr_7Co the substitution of a highly anisotropic Co(II) *3d* ion into this Cr ring could transmit this anisotropy into the lowest molecular eigenstates of the wheel, giving rise to an effective methodology for building future SMMs.

The assessment of how efficient this transmission mechanism is can be examined through the spin energy spectrum, which as has been shown can be accurately obtained from inelastic neutron scattering (INS). In particular 4D-INS has been demonstrated to be an incredibly powerful tool in probing the spin dynamics of molecular nanomagnets[16,17] via the extraction of the huge phase

---

[a] School of Chemistry, The University of Manchester, Oxford Road, Manchester, M13 9PL, UK.
[b] Institut Laue-Langevin, 71 Avenue des Martyrs CS 20156, Grenoble, France.
[c] . Dipartimento di Scienze Matematiche, Fisiche e Informatiche University of Parma, 43124 Parma, Italy.
[d] Institute for Advanced Simulation, Forschungszentrum Jülich, Germany.
[e] ISIS facility, Rutherford Appleton Laboratory, Chilton, Didcot, OX11 0QX, Oxfordshire, UK.

† Footnotes relating to the title and/or authors should appear here.
Electronic Supplementary Information (ESI) available: [details of any supplementary information available should be included here]. See DOI: 10.1039/x0xx00000x

space (E,Q_x,Q_y,Q_z) dependence of the scattered cross section, thanks to modern position-sensitive detectors, and so we look to utilise the technique here.

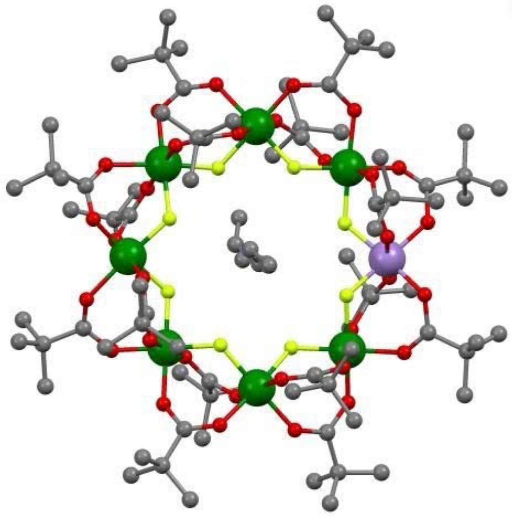

Figure 1 shows the molecular structure of $Cr_7Co[F_8(O_2C^tBu_{16})]$ antiferromagnetic ring (purple, Cr; green, Cr; yellow, F; red, O; light blue, N; grey, C; all H atoms omitted for clarity).

II Experimental

The structure of the molecules have been determined using X-ray diffraction analysis. Data were collected at 100K using a Mo-K radiation source on an Agilent Supernova. The observed Bragg peaks could be indexed in the tetragonal I4 space group with the following lattice parameters obtained at 100 K.

a=b=19.9066(6) Å and c=16.1991(9) Å

with the metal ions forming the shape of an almost regular planar octagon with each metal in an octahedral environment bridged on the inside by 8 fluorides and by 16 pivalates on the outside.

In order to characterise the parameters defining the effective spin-Hamiltonian describing the system INS measurements have been performed using the IN5 time-of-flight (ToF) spectrometer at the Institut Laue-Langevin and the LET ToF spectrometer at the ISIS neutron facility.

Preliminary variable temperature measurements were first performed on 2 g of powder sample sealed in an annular sample can at the ILL in Grenoble, France over a temperature range of 1.5-15K in order to yield information on the energetic origin of different transitions. These measurements were taken using a wavelength of 3.2 Å inside a standard "Orange" liquid-4He crystostat with the scattering intensity integrated over all detector angles to obtain the energy spectra. Once it was clear that the signal response was strong and the magnetic transitions clearly visible, a 2g single crystal sample was prepared and again measured using IN5. The sample was measured at 1.5 K with the **c**-axis perpendicular to the horizontal scattering plane which rested on a specially made shelf inside the annular sample can, surrounded by excess solvent and sealed under a He atmosphere. The Q-dependence of the excitations were surveyed by rotating the sample throughout the full 360 degrees and measured at every degree as required by the 4D-INS technique. These measurements were undertaken using an incident wavelength of 3.2 Å and also with a 6.5 Å measurement. The full $S(\mathbf{Q},\omega)$ phase space was then reconstructed in the HORACE analysis suite by concatenating each run[18]. Further INS experiments were then conducted on another single crystal sample at ISIS using LET. This time the experiment determined the field-dependence on the magnetic transitions, with the crystal oriented with the scattering plane and the magnetic field applied in the plane of the rings. The field was applied over a range of 0-7T with measurements taken using a 7.4 and 5.2 Å incident energy corresponding to a resolution of 0.03 and 0.07 meV respectively.

III The Hamiltonian Model

The microscopic magnetic properties of AF molecular nanomagnetic rings are well described by effective spin-Hamiltonians and for the Cr_7Co system the following spin-Hamiltonian is used.

$$\begin{aligned}
&\hat{H} \\
&= \sum_{i=1}^{6} J_{Cr-Cr}\hat{s}_i \cdot \hat{s}_{i+1} + J_{Cr-Co}\hat{s}_{Co} \cdot (\hat{s}_1 + \hat{s}_7) \\
&+ \sum_{i=1}^{7} d_{Cr}\hat{s}_{z,i}{}^2 + \hat{s}_{Co} \\
&\cdot \left({R_{site,1}}^{-1} \begin{pmatrix} -D_{local}+E_{local} & 0 & 0 \\ 0 & -D_{local}-E_{local} & 0 \\ 0 & 0 & 2D_{local} \end{pmatrix} R_{site,1} \right) \\
&\cdot \hat{s}_1 + \hat{s}_{Co} \\
&\cdot \left({R_{site,7}}^{-1} \begin{pmatrix} -D_{local}+E_{local} & 0 & 0 \\ 0 & -D_{local}-E_{local} & 0 \\ 0 & 0 & 2D_{local} \end{pmatrix} R_{site,7} \right) \\
&\cdot \hat{s}_7 + \mu_B \sum_{i=1}^{8} \hat{s}_i \cdot \left({R'_{site}}^{-1} g_{local} R'_{site} \right) \cdot B \qquad (1.0)
\end{aligned}$$

where $site = 1/8$

The two initial (leading) terms in the Hamiltonian describe Heisenberg-Dirac isotropic AF exchange coupling between nearest neighbour metal ions in the Cr_7Co ring. The Cr-Cr exchange pair couplings around the ring have been assumed equivalent, as in the isostructural parent Cr8 compound (1.46 meV). Both Cr-Co exchange couplings are also considered equivalent. The next term describes single ion axial anisotropy for Cr s=3/2 ions, with d_{Cr} again based on that found in the parent compound (-0.038 meV). The last term describes the

Zeeman interaction. R_{site} and R'_{site} are rotation matrices relating the local reference frame to the molecular reference frame that are dependent on individual site positions. The principle axis of the molecular reference frame Z is perpendicular to the plane of the wheel.

DFT calculations based on the approach described in [PRL 110, 157204 (2013)][19] were used as a guide for fitting the spin Hamiltonian parameters. According to ab-initio calculations, the Co ion can be described at low temperature as an effective spin doublet, separated by about 180 K from the first excited doublet. Our first-principles approach also predicts an isotropic Cr-Co exchange interaction of 21 K and anisotropic exchange with axial and rhombic local terms D = 0.48 meV and E = 0.41 meV. These parameters, as well as the principal values of the Co g tensor and the orientation of the main anisotropy axes were used as a guide for the fitting of the spin Hamiltonian parameters, based on the inelastic neutron scattering data (I vs ω, I vs **Q**, powder and field dependent measurements). Although this is the Hamiltonian with the least amount of parameters necessary to accurately reproduce the vast amount of data extracted, DFT calculations show there to be a sizeable Dzyaloshinskii-Moriya interaction. This is a second-order superexchange term that acts only through the mixing of states with different spin-multiplets. These effects are significantly weaker than those of anisotropic exchange and thus it is not necessary to include such effects to reproduce the data observed.

The fitting procedure was based on the diagonalization of the full spin Hamiltonian. The anisotropy mixes states with different S and M so that the total spin S is not a good quantum number and the total Hamiltonian cannot be diagonalised within each 2S+1 block. Therefore the isotropic exchange Hamiltonian was diagonalised in the full Hilbert space; then anisotropic terms were included on spin multiplets below 120 K, thus reducing the numerical challenge of the calculation. We have checked that higher energy cut-offs do not produce visible effects in the calculated spectra. Spectra were computed using a Gaussian line shape with a FWHM equal to the resolution function with an additional component associated with strain effects in the exchange coupling amongst the ensemble average.

The Co ion is delocalised around the ring over all 8 sites and thus every site has the same occupation probability. Hence the inelastic neutron scattering cross-section was computed as the sum of the five different contributions arising from the inequivalent positions of the Co ion.

IV Experimental Results and Analysis

The results of the preliminary variable temperature powder measurements on IN5 with their accompanying fits are shown below in figure 2

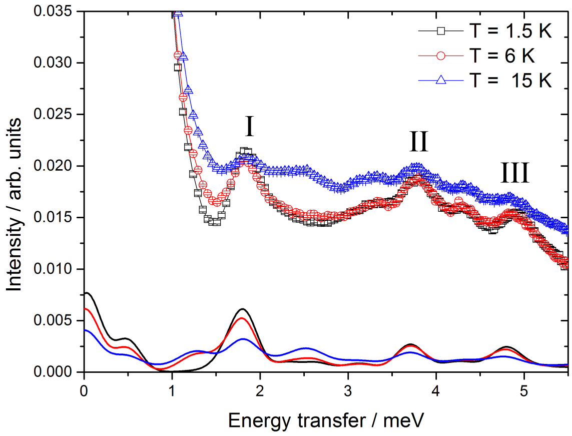

Figure 2. Variable temperature energy spectrum for the Cr_7Co powder sample measured at a wavelength of 3.2 Å with marked lines (measured) and smooth lines (simulated).

The measurement of the powder sample shows several magnetic transitions reasonably well resolved but with a sizeable background from the incoherent scattering which occurs due to the relatively large hydrogen content from the organic ligand groups. The collection of data over the demonstrated temperature range allows us to ascertain that the transitions at 1.8, 3.8 and 4.7 meV are from the ground state and that the other neighbouring peaks which are buried in the measured spectra are a result of transitions from excited states. All 3 main peaks observed in the powder spectrum **I, II and III** are from the ground S=1 state going to the S=2 excited state and are referenced in the energy level diagram in figure 3.

The simulation produces the peaks in the correct positions and form, which were obtained using J_{Cr-Co} =1.64 meV which is slightly larger than the neighbouring J_{Cr-Co} interactions. A best fit is obtained with D_{local}=-0.4 meV and E_{local}=-0.689 meV. The energy level diagram resulting from this model is shown below in figure 3.

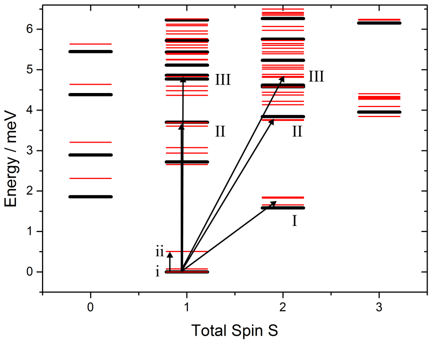

Figure 3. Energy of the lowest isotropic spin eigenstates as a function of the total spin (black), with transitions corresponding to those observed in the spectra labelled with anisotropy included in the calculation (red).

The following 4D-INS single crystal measurement was also carried out on IN5 to extract the full phase space with the obtained energy spectra shown below in figure 4.

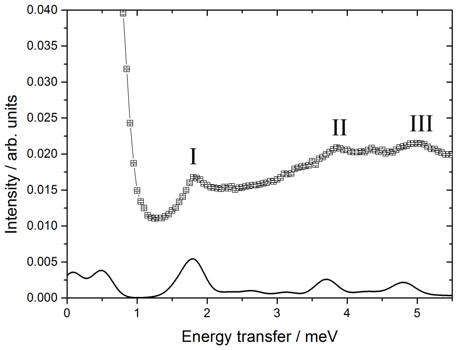

Figure 4. INS spectrum measured at 1.5 K for the single crystal Cr_7Co measured on IN5 using a wavelength of 3.2 Å and integrated over all scattering angles.

Whilst the use of a single crystal results in a heavier background from the incoherent scattering contribution the measurement shows that the scan is consistent with that previously measured on the powder data with the main 3 transitions **I,II** and **III** all accounted for and no extra unexpected features.

Scans were also conducted again at 1.5 K but this time with a higher resolution wavelength of 6.5 Å in order to resolve the lower energy transitions which were previously buried in the elastic line and can be seen below in figure 5.

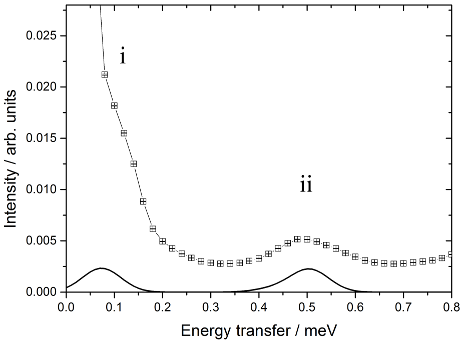

Figure 5. INS spectrum measured at 1.5 K for the single crystal Cr_7Co measured on IN5 using a wavelength of 6.5 Å and integrated over all scattering angles.

Here we have managed to resolve two features by using the higher resolution setting, one peak at 0.5 meV and another very low energy peak buried in the elastic line at 0.07 meV both corresponding to intramultiplet transitions **i** and **ii** in the ground state S=1 multiplet (see level diagram in Fig. 3).

Although the energy spectra (integrated over Q) set constraints on the possible exchange terms they are not truly selective and so we look to the full 4D (E,Qx,Qy,Qz) phase space for the lowest energy transitions, which have been fully extracted. The large quantity of hydrogen provides a large incoherent scattering contribution which presents a sizeable obstacle and has to be separated from the magnetic signal; furthermore the irregular shape of the crystal contributes an angle-dependet attenuation factor which must also be corrected for. This is considered by taking the self-shielding projected onto the local non-magnetic data, near a magnetic transition and then normalising through the transition by it. The transition is then fitted for each and every point through the truncated Q-space with a Gaussian and local background to separate the magnetic behaviour from the non-magnetic. The raw data for such a map, extracted from the first peak shown in the 3.2 Å spectrum at 1.8 meV is shown below in figure 6 along with the same map after this cleaning process has been completed.

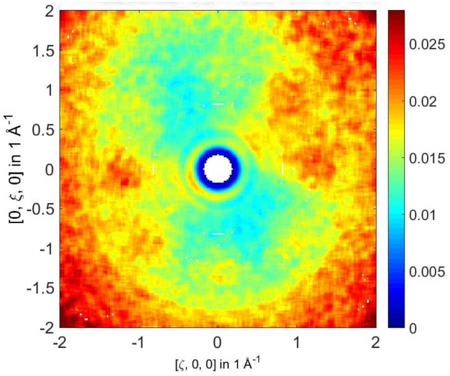

Figure 6. Map extracted for the peak at 1.8 meV before data treatment, the large quantity of H in this molecular nanomagnet results in an incoherent background which dominates the phase space.

The extracted map after clean up and the accompanying simulation are shown below in figure 7-8

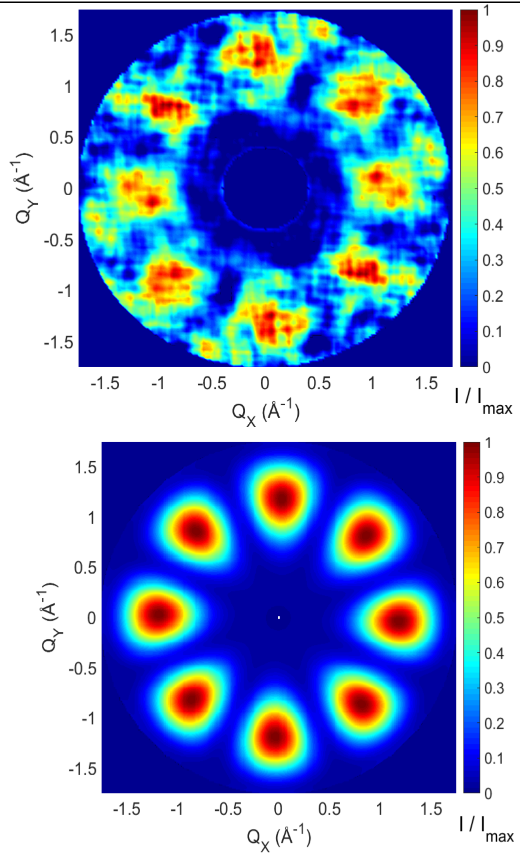

Figure 7. Extracted constant energy plot of the neutron scattering intensity of the observed excitation at 1.8 meV for the 3.2 Å data in the single crystal of Cr_7Co after data treatment. Data have been integrated over the full experimental Q_z range measured on IN5 of -0.2 to 0.2 Å with the colour bar displaying the transition intensity.

The data cleaning process allows the map to be reproduced remarkably well, with the correct positions of the modulations. This process was repeated for all visible transitions and thus further maps were extracted from the two peaks in the 6.5 Å data and are shown below.

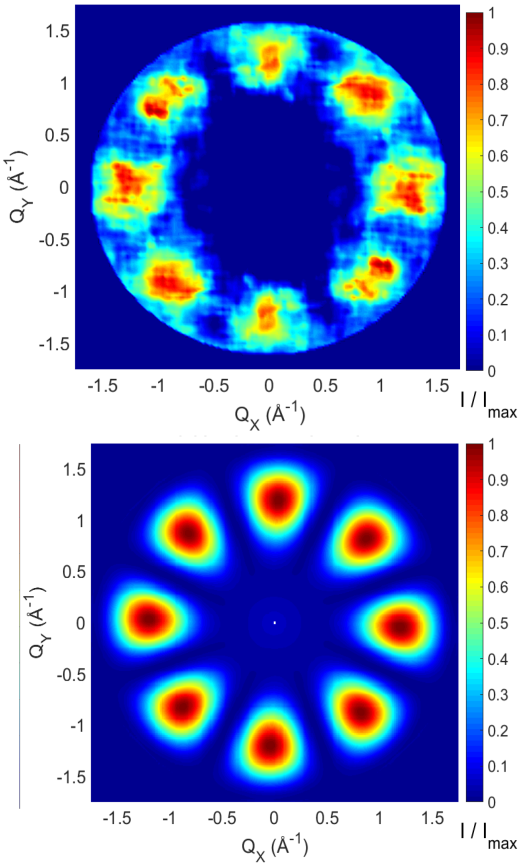

Figure 8. Extracted constant energy plot of the neutron scattering intensity of the observed excitation at 0.1 meV for the 6.5 Å data in the single crystal of Cr_7Co after data treatment. Data have been integrated over the full experimental Q_z range measured on IN5 of -0.2 to 0.2 Å with the colour bar displaying the transition intensity.

In general the positions and intensities of the modulations are very well reproduced. The peak at 1.8 meV was particularly difficult to extract the map for, due to its proximity to the elastic line. The final peak measured at 0.5 meV in the 6.5 Å spectrum is shown overleaf.

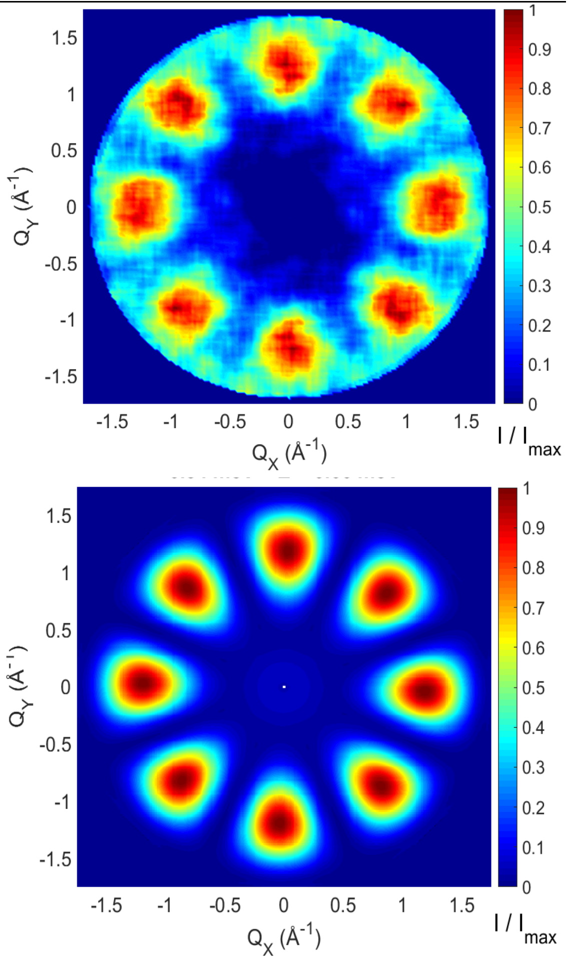

Figure 9 shows the extracted constant energy plot of the neutron scattering intensity of the observed excitation at 0.5 meV for 6.5 Å data in the single crystal of Cr$_7$Co after data treatment. Data have been integrated over the full experimental Q_z range measured on IN5 of -0.2 to 0.2 Å with the colour bar displaying the transition intensity.

As can be seen in the energy spectra, the local background of the 0.5 meV peak is comparatively low and significantly far from the elastic line, therefore the map can be extracted much more cleanly. It is very well reproduced with the positions and intensities of the modulations finely accounted for, the general form of the regions of intensity are also very well reproduced by the model employed. Attempts to extract the higher energy peaks, namely **II** and **III** were unsuccessful due to the larger local background associated with them.

Lastly single crystal measurements have also been made under the application of a magnetic field in order to test that the field dependence is consistent in accordance with that suggested from the other measurements taken to complete the spin-Hamiltonian model. The magnetic field was applied in the plane of the ring, since the Co is delocalised around the ring the angle between the field and the anisotropic and g-tensor changes and thus the rotation matrices are necessary to relate the local reference frames to the molecular frame. The spectra and their field dependence are shown below in figure 10.

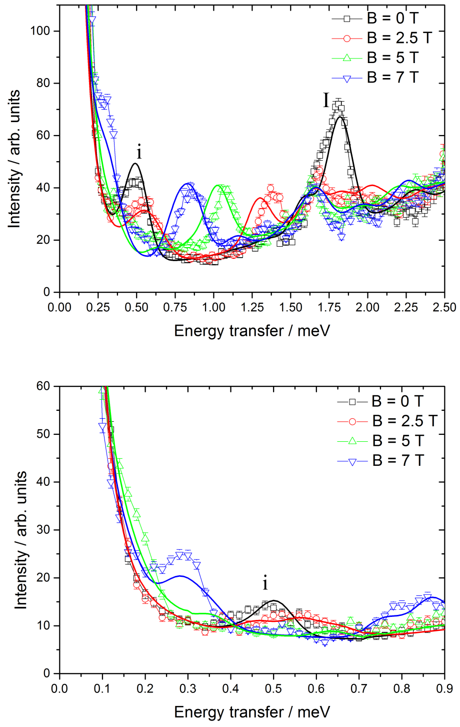

Figure 10 Variable temperature energy spectrum for the Cr$_7$Co single crystal sample measured at 1.8K with a wavelength of 5.2 Å (top) and 7.4 Å (bottom) with marked lines (measured) and smooth lines (simulated) for a variety of field values

The measured data is fitted well by the spin-Hamiltonian model and shows excellent agreement for both peak position and intensity over a range of magnetic fields. The g-tensor for the Co(II) ion is taken from EPR measurements of the isostructural Ga$_7$Co ring. where a value of g_{Co}=6.8,2.9 and 2.7 is found for g_x, g_y and g_z respectively, g_{Cr}=1.98 is as measured from this molecules parent compounds.

IV Discussion

Through INS we were able to obtain a good quantity and quality of data, which we have been able to fit well with the adopted approach. The relatively large quantity of H in these molecules does induce some issues with the incoherent scattering and so for some of the higher energy peaks where there was a particularly large background and so we were unable to extract the phase space dependence cleanly for these peaks. Nonetheless we have still extracted a large amount of information and are able to characterise the magnetic character of this compound in the lowest eigenstates to show that the molecular spin ground state of the ring is an S=1 state accomplished through antiferromagnetic exchange. The J_{Co-Cr} is found to be approximately 10% greater than the other J_{Cr-Cr} couplings around the ring, thus, as expected we are able to form strong exchange interactions between the Cr-Co pairs. The accuracy of this model is reflected in its ability to successfully reproduce the complexities of the 4D phase space and the in-field spectra and is the one with the simplest parameter set. As expected the lowest eigenstates of this even membered spin ring closely follow the expected energy distribution for L-band states. Where the energy of this parabolic band has energies governed by the Landé interval rule $E_S = \Delta[S(S+1) - S_0(S_0+1)]/[S_1(S_1+1) - S_0(S_0+1)]$ where Δ is the energy of the first excited state, S_0 is the spin of the ground state and S_1 the spin of the first excited level.

If we compare this compound to a related wheel, namely Cr_7Mn where the ground state is also an S=1 [20], we find that the anisotropy induced splitting for that case is roughly 0.1 meV. Substitution by this even more anisotropic Co(II) ion increases the anisotropy induced splitting to roughly 0.5 meV.

Hence, our extensive INS study demonstrates that Cr7Co is a model system to study how high Co anisotropy can be transferred to the whole molecule. This could make Cr7Co the forefather of a new generation of SMMs, in which high-spin isotropic ions are strongly exchange-coupled to anisotropic 3d ions.

With deuteration it will be possible to extract even more information from the higher energy peaks, to verify that the model is indeed univocal with some of the higher energy transitions, however the process of cleaning the data by taking into account the self-attenuation as well as fitting the transition for each Q-point allows one to separate sufficiently the magnetic transition from reasonably heavy non-magnetic background.

V Conclusion

We have used inelastic neutron scattering to successfully characterise and probe the spin dynamics in the Cr_7Co AF ring; we have found the minimum number of parameters required to describe the observed behaviour. What we find is that the insertion of the highly anisotropic Co(II) induces a splitting of around 0.5 meV, around 5 times that observed in the isostructural Cr_7Mn ring. This is therefore a potential method to achieving highly anisotropic SMMs by maintaining strong exchange interactions and transmitting the single ion anisotropy through the inserted ion. INS remains the perfect tool to quantify how much anisotropy can be transferred into the lowest eigenstates of a system by such an insertion. The ability to extract such vast amounts of information through the 4D-INS measurements as well as coupling this with in-field data allows us to model the data with precision and reliability.

References

[1] D. Gatteschi, R. Sessoli, and J. Villain, *Molecular Nanomagnets* (Oxford University Press, **2006**).

[2] A. Chiolero and D. Loss, *Phys Rev. Lett.* **1998**, *80*, 169. [3]

[3] O. Waldmann, T.C. Stamatatos, G. Christou, H.U. Güdel, I. Sheikin, H. Mutka, Phys Rev. Lett. 2009, 102, 157202.

[4] R.E.P. Winpenny, Molecular Cluster Magnets (World Scientific Publishing Company, Singapore 2011).

[5] O. Waldmann, *Phys. Rev. B* **2002**, *65*, 024424.

[6] F.K. Larsen, E.J.L. McInnes, H. El Mkami, J. Overgaard, S. Piligkos, G. Rajaraman, E. Rentschler, A.A. Smith, G.M. Smith, V. Boote, M. Jennings, G.A. Timco, R.E.P. Winpenny, Angewandte Chemie-International Edition **2003**, 42, 101.

[7] A. Ardavan, O. Rival, J.J.L. Morton, S.J. Blundell, A.M. Tyryshkin, G.A. Timco, R.E.P. Winpenny, Phys Rev. Lett. 2007, 98, 057201.

[8] F. Troiani, A. Ghirri, M. Affronte, S. Carretta, P. Santini, G. Amoretti, S. Piligkos, G. Timco, and R.E.P. Winpenny, Phys Rev. Lett. **2005**, 94, 207208.

[9] F. Troiani, M. Affronte, S. Carretta, P. Santini, and G. Amoretti, Phys Rev. Lett. **2005**, 94, 190501.

[10] M. Affronte, A. Ghirri, S. Carretta, G. Amoretti, S. Piligkos, G.A. Timco, R.E.P. Winpenny, Appl. Phys. Lett. **2004**, 84, 3468.

[11] S. Accorsi, A-L Barra , A. Caneschi, G. Chastanet, A. Cornia, A.C. Fabretti, D. Gatteschi, C. Mortalò, E. Olivieri, F. Parenti, P. Rosa, R. Sessoli, L. Sorace , W. Wernsdorfer , L. Zobbi, J. Am. Chem. Soc. **2006**, 128, 4742.

[12] A. Cornia, L. Rigamonti, S. Boccedi, R. Clérac, M. Rouzieres, L. Sorace, Chem. Commun. **2014**, 50, 15191.

[13] D.N. Woodruff, R.E.P. Winpenny, R.A. Layfield, *Chem. Rev.* **2013**, 113, 5110.

[14] L. R. A and M. Muralee, *Lanthanides and Actinides in* Molecular Magnetism (Wiley VCH, Germany **2015**).

[15] J. Tang and Z. Peng, *Lanthanide Single Molecule Magnets* (Springer, **2015**).

[16] E. Garlatti, T. Guidi, S. Ansbro, P. Santini, G. Amoretti, J. Ollivier, H. Mutka, G. Timco, I.J. Vitorica-Yrezabal, G.F.S. Whitehead, R.E.P. Winpenny, S. Carretta, Nat. Commun.

[17] M.L. Baker, T. Guidi, S. Carretta, J. Ollivier, H. Mutka, H.U. Güdel, G.A. Timco, E.J.L. McInnes, G. Amoretti, R.E.P. Winpenny, P. Santini, Nature Physics **2012**, 8, 906.

[18] R.A. Ewings, A. Buts, M.D. Le, J. van Duijn, I. Bustinduy, T.G. Perring, Nuclear Instruments & Methods in Physics Research Section a-Accelerators Spectrometers Detectors and Associated Equipment **2016**, 834, 132.

[19] A. Chiesa, S. Carretta, P. Santini, G. Amoretti, and E. Pavarini, Phys Rev. Lett. **2013**, 110, 157204.

[20] R. Caciuffo, T. Guidi, G. Amoretti, S. Carretta, E. Liviotti, P. Santini, C. Mondelli, G. Timco, C.A. Muryn, R.E.P. Winpenny, *Phys. Rev. B* **2005**, *71*, 174407.

Chapter 4 INS Study of Mn_{12}

4.1 Mn_{12} Background

The archetypical SMM, Mn_{12} is composed of a central $Mn^{IV}O_4$ cubane and an outer Mn_8^{III} ring has been the motivation for some hundreds of studies, yet the spin Hamiltonian describing the system has been surprisingly difficult to formulate. Whilst trial Hamiltonians have been fitted to INS, EPR and magnetometry data separately, a universal model to explain the data for all of these has been left wanting and is still a matter of debate[64-66].

Despite the excitement over the discovery of Mn_{12}'s magnetic properties, substantial improvements to the SMM qualities such as the blocking temperature (highest temperature at which the hysteresis loops are observed) have failed to be realised. In order to create better functioning SMMs, the barrier to relaxation needs to be raised and this has been the main focus of research in molecular magnetism for the past 20 years. The anisotropy barrier for integer spin systems is governed by

$$U_{eff} = |D|S^2 \tag{4.1}$$

Where U_{eff} is the energy of the anisotropy barrier, D is the axial anisotropic parameter and S is the total spin quantum number.

In polymetallic cages such as Mn_{12} the major contribution to the D parameter originates from the single ion anisotropy. In Mn_{12}, the Mn(III) ions are Jahn-Teller distorted. These Jahn-Teller axes are frequently aligned and so their individual zero field splittings can construct to give a large D, making them highly effective building blocks for SMMs and ones which are often exploited for such practice. The inherent large number of unpaired electrons in high spin Mn ions of various oxidation states pertains to the generation of large total spin ground states. This is aided further by the likelihood of ferro- or ferrimagnetic interactions[56].

Two major processes contribute to the crossing of this barrier and hence loss of magnetisation retention in zero-field. At higher temperatures the most important is the thermal activation, which obeys the Arhenius relationship

$$\tau = \tau_0 e^{\frac{U_{eff}}{k_B T}} \tag{4.2}$$

Where τ is the relaxation time and τ_0 is the time constant

The activation barrier for Mn_{12} is shown below in figure 15

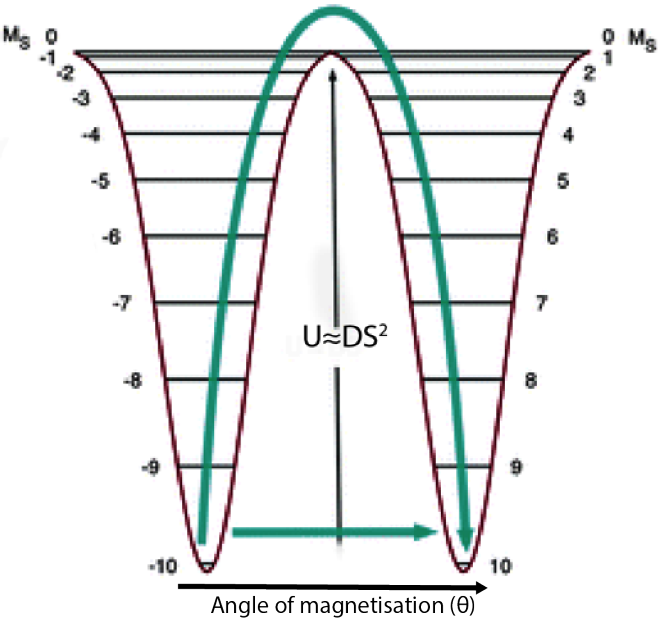

Figure 15. Schematic of the activation barrier in Mn_{12}

The other important process that opposes the magnetisation retention is the quantum tunnelling of the magnetisation through the barrier, which occurs at specific field values[7].

In order to understand the essential characteristics of this archetypical material, it is of the upmost importance that the spin Hamiltonian for the system is finally deciphered. One particularly powerful way to tackle this is through 4D-INS, which allows one to achieve a model with a much higher degree of certainty than is possible with simply an energy spectrum alone due to the complexity of the vectorial Q-dependence of the $S(Q,\omega)$ function. The following work achieves this and uses the technique to portray the propagation of individual Mn spins around the magnetic ground state.

Fingerprints of Mn_{12}, the forefather of molecular nanomagnets

A. Chiesa[1], S. Carretta[1], T. Guidi[2], S. Ansbro[3], G. A. Timco[3], I. Vitorica-Yrezabal[3], E. Garlatti[1], G. Amoretti[1], R. E. P. Winpenny[3] and P. Santini[1]

1 Dipartimento di Scienze Matematiche, Fisiche ed Informatiche, Università di Parma, I-43124 Parma, Italy
2 ISIS facility, Rutherford Appleton Laboratory, OX11 0QX Didcot, UK
3 School of Chemistry and Photon Science Institute, The University of Manchester, M13 9PL Manchester, UK

The ability to store magnetic information in a single molecule was reported for the first time by Sessoli et al. in a polymetallic cage complex known as Mn_{12} (1). **Many further breakthroughs followed from studies of this molecule, including the observation of macroscopic quantum tunneling of magnetization** (2), **and the discovery that Mn_{12} can be used to build devices based on the Grover algorithm** (3). **The phrase "single molecule magnet" (SMM) was invented to describe the physics observed for Mn_{12}, and studies on this molecule have inspired an entire field spanning chemistry, physics and nanotechnology, which continues to produce remarkable science. Recent examples include the observation of Rabi oscillations on an individual molecule** (4), **the understanding and control of environmental decoherence** (5) **or the incorporation in graphene nanodevices** (6). **However, the great potential of complex polycentric molecules is still largely unexplored due to the difficulty to determine the interactions within the core. Mn_{12} is a particularly striking example: in spite of hundreds of papers there is not even an unambiguous description for the leading interactions of this archetypal molecule, twenty-five years after it fathered a new field of science. Here we close this long-standing unresolved case: we exploit four-dimensional inelastic neutron scattering** (7) **to portray how individual Mn spins fluctuate around the magnetic ground state, and we thus pinpoint the exchange couplings of Mn_{12} for the first time. The highly selective power of these experiments arises from their unrivaled capability to extract information at the subnanometric scale, where the spin precession patterns are unambiguous fingerprints of the magnetic Hamiltonian. Our results open unprecedented prospects in understanding magnetic spin clusters and motivate the synthesis of new polycentric nanostructures, where the pattern of interactions is optimal for specific fundamental issues or applications.**

Molecular nanomagnets (MNMs) (8) (9) (10) (11) (12) (13) (14) (15) (16) (17) are spin clusters whose phenomenology results from a number of interactions in the magnetic core, where isotropic exchange couplings are usually leading and various types of anisotropic single- and two-ion terms act perturbatively. Molecules displaying magnetic remanence like Mn_{12} are usually described in terms of phenomenological "giant spin" models, where a single quantum spin **S** ($S=10$ in Mn_{12}) represents the magnetic core as a whole (18) (19). Although this approach is cost-effective in terms of model complexity, it leaves in the shadows the nature of the giant spin at the atomic level, hindering the tailoring of the magnetic core for improved performance in fundamental or applicative issues (20). Moreover, the many-body character of the core emerges clearly even in the low-energy physics [e.g., (21) (10)].

In spite of an unequalled number of theoretical and experimental investigations of Mn_{12}, no sound determination exists of the exchange couplings between the various Mn ions, which are the leading interactions within the cluster. Hence, the debate about Mn_{12} is still completely open, as witnessed by recent studies (22) (23) (24). Most of the proposed models are based on a set of four isotropic exchange parameters, reported in the schematic representation in Fig. 1a (with J_4=J_4'). The spin Hamiltonian also includes anisotropic terms accounting for the uniaxial behavior of the system and it reads:

$$H = \sum_{<m,n>} J_{mn} \mathbf{s}_m \cdot \mathbf{s}_n + d \sum_{m=5}^{12} s_{zm}^2 \qquad (1)$$

where the pairs of ions included in the first sum are indicated in Fig. 1a and zero-field splitting terms are considered only on the eight highly-anisotropic Mn^{3+} ions. We have checked that more complex choices for the anisotropic term (e.g., small non-axial terms or higher-order contributions) do not significantly affect the determination of exchange constants and are here neglected for simplicity (see Methods).

As stated above, a firm set of parameters for Eq. (1) could not be found yet. Indeed, the known excitation energies (25) only provide a coarse characterization of the spin Hamiltonian through its eigenvalues. In particular, they lack the selective information associated with the structure of eigenvectors, i.e., how individual atomic spins move when excitations are triggered. Here we use the four-dimensional inelastic neutron scattering (4D-INS) technique (7) to extract such information for the low-energy transitions shown in Fig. 1b. The power of the technique comes from the capability to measure the scattering cross-section S(E, **Q**) over large portions of the energy-wavevector (E, **Q**) space, yielding a faithful portray of spin fluctuations on the space- and time-scales characterizing the internal dynamics of the magnetic core. This experimental information fingerprints the eigenstates of the spin Hamiltonian, thus enabling us to fix the value of exchange couplings univocally for the first time.

We have studied specifically Mn_{12}-^{t}BuAc (full formula $[Mn_{12}O_{12}(O_2CCD_2C(CD_3)_3)_{16}(CD_3OD)_4]\bullet(C_2H_5)_2O$) which crystallises with S_4 symmetry, and it is the deuterated analog of the isostructural $[Mn_{12}O_{12}(O_2CCH_2Bu^t)_{16}(MeOH)_4]\bullet MeOH$ molecule (26). Single crystals large enough for 4D-INS studies were grown by slow evaporation, under N_2 at ambient temperature, of a solution of the Mn_{12}-^{t}BuAc compound dissolved in a mixture of diethyl ether/methanol-d_4 in presence of a small amount of deuterated *t*-butylacetic acid. Measurements have been performed on the high-resolution LET spectrometer at ISIS, on a collection of oriented single crystals (see Methods). Figure 1b shows INS spectra taken at T = 1.5 K at two different incident neutron wavelengths, with five peaks clearly distinguishable between 1 and 10 meV. Previous INS studies of related Mn_{12} molecules (25) have assigned these peaks to transitions from the ground spin doublet $\left|S=10, M=\pm 10\right\rangle$, as the population of any other state is negligible at this temperature. For example, the lowest-energy peak (labeled **I**) at 1.25 meV represents the intra-multiplet transition to the $\left|S=10, M=\pm 9\right\rangle$ doublet.

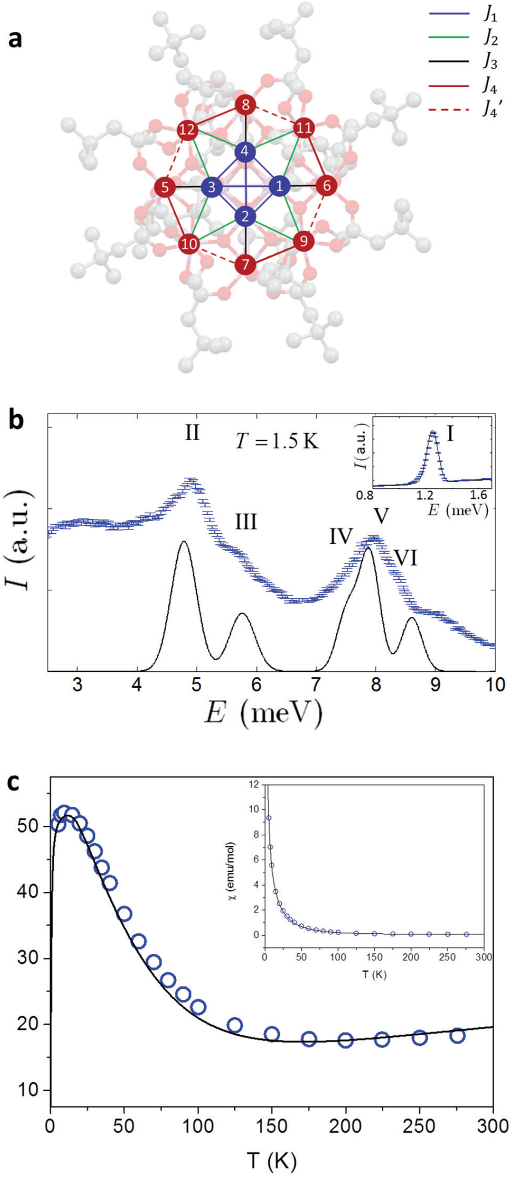

Figure 1 | The Mn_{12} nanomagnet. **a,** Scheme of the Mn_{12}-tBuAc molecule, with different lines representing the relevant different exchange interactions. Red circles: Mn^{3+} ions (s=2). Blue circles: Mn^{4+} ions (s=3/2). Seven distinct exchange constant are allowed by the S_4 symmetry of the molecule, but most models assume only four parameters (J_{1-4} with $J_4' = J_4$) because of similarities in some exchange paths. **b,** INS spectrum collected on LET at 1.5 K, using 15.4 meV (and 4.2 in the inset) incident neutron energy. The continuous line is the corresponding simulation with the best-fit parameters (in meV) $J_1 = -1.2$, $J_2 = 3.2$, $J_3 = 6.6$, $J_4 = 0.55$, $J_4' = 0.30$, $d = -0.315$. Eigenstates are listed in Extended Data Table 1. Peak **I** corresponds to a transition between states M = ±10 and M = ±9 of the ground S=10 multiplet. The slight asymmetry of the peak is due to the instrumental resolution function of the TOF spectrometer. Peaks **II**-**VI** are inter-multiplet transitions to different excited S=9 multiplets. The broad peak at 3 meV is a phonon, as shown by the monotonic increase as Q^2 of the associated form factor. **c,** χT vs. T (inset: χ vs. T). Calculations with the best-fit parameters (lines) are in very good agreement with experiments [dots, (26)].

Using the 4D-INS technique we can obtain far more information (Figure 2). 4D-INS data reported in Figure 2a directly demonstrate (see the discussion of Figure 3e below) that excitation **I** corresponds to a precession of the giant spin around the anisotropy axis, with its internal structure kept rigid. As discussed in (27) and in Methods section, this information is equivalent to that contained in the distribution of the giant-spin moment over different Mn ions, i.e., the set of expectation values $\pm\mu_n = \langle S = 10, M = \pm 10|s_{zn}|S = 10, M = \pm 10\rangle$. The measured form-factor (i.e., the **Q**-dependence of the scattering intensity) of Fig. 2a enables us to extract the set of $\mu_n$values in the inset, which are in line with those determined by neutron diffraction (28) and NMR (29). The moment distribution reveals ferromagnetic correlations among the four Mn^{4+} and among the eight Mn^{3+} spins, with the two sets antiferromagnetically correlated to each other. However, the Mn^{3+} and Mn^{4+} moments are significantly below saturation (see Extended Data Table 1), indicating that the spins are not locked in a maximally-aligned state due to quantum fluctuations.

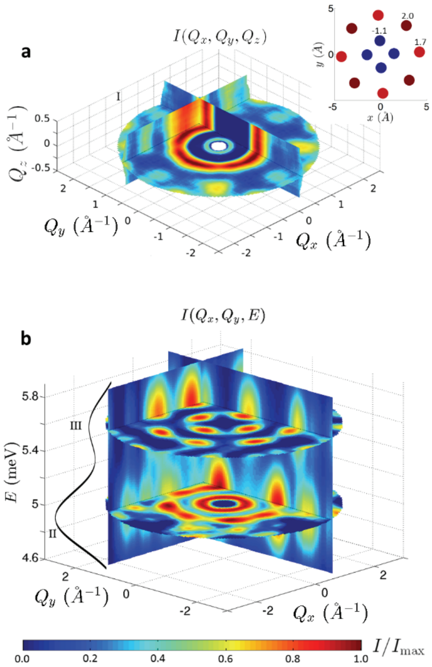

Figure 2 | Exemplary 4D INS data. **a,** Form factor for the intra-multiplet transition $|S = 10, M = \pm 10\rangle \rightarrow |S = 10, M = \pm 9\rangle$, i.e., S(E,**Q**) for E=1.25 meV (giant-spin excitation **I**). The inset shows the equivalent real-space information, that is the distribution of the static magnetization of the giant spin over the three inequivalent Mn sites, $\mu_n = \langle S = 10, M = 10|s_{zn}|S = 10, M = 10\rangle$. The values (in μ_B) μ_1=-1.2 (2), μ_6=1.7 (0.15) and μ_{11}=2 (0.15) are extracted directly from the form-factor and compare well with polarized neutron diffraction (-1.17, 1.84, 1.90) (28) and NMR (-1.3, 1.8, 1.8) (29) data on a slightly different variant of Mn_{12}. **b,** S(E,**Q**) as a function of Q_x, Q_y and E, and integrated over the full Q_z range. The energy window contains the intermultiplet peaks **II** and **III** of Fig. 1b.

This local distribution of moments is stable over a range of exchange constants and hence is not sufficient to fix the magnitude of the exchange interactions J_{mn} uniquely. It is intuitively clear that exchange is probed more effectively through excitations that break the internal alignment of Mn spins in their ground state. Just like spin waves in bulk magnetic compounds, their energies and structure directly reflect the values of exchange constants. These excitations correspond to peaks **II-VI** in Fig. 1b and represent inter-multiplet transitions between the ground $\left|S=10,M=\pm10\right\rangle$ doublet and a set of excited $\left|S=9,M=\pm9\right\rangle$ doublets. Although these **Q**-integrated energy spectra, together with susceptibility (Fig. 1c), provide constraints on the set of exchange constants, they are not selective. Conversely, a clear identification of the $\left|S=9\right\rangle$ wavefunctions is achieved thanks to the measured **Q** dependencies, which contain detailed information on the composition and symmetry of the states involved in the transition. For example, Fig. 2b shows S(E,**Q**) as a function of Q_x, Q_y and E, and integrated over the full Q_z range. The energy interval spans peaks **II** and **III** of Fig. 1b, while constant-energy cuts of S(E,**Q**) for E corresponding to all the peaks in Fig. 1 are shown in Fig.3. The great amount of information available in these experimental data is immediately evident.

The S(E,**Q**) data fully characterize the low-lying multiplets, and make it possible to identify the five exchange parameters. The simulation of these data (Figure 3c) unequivocally establishes the five exchange parameters (in meV): J_1 = -1.2(1), J_2 = 3.2(2), J_3 = 6.6(3), J_4 = 0.55(5), J_4' = 0.30(5). The agreement between calculation and experiment is very good and this model fits also the magnetic susceptibility (Figure 1c) and peak positions (Figure 1b). There is just a slight discrepancy for the position of peak **VI**, whose fine-tuning requires additional small parameters in Eq. (1) (see Methods). As expected in broad terms from the internal structure of the giant-spin (Fig. 2a), antiferromagnetic couplings between Mn^{3+} and Mn^{4+} ions are leading. The coupling between the four Mn^{4+} ions is ferromagnetic, whereas that between the eight Mn^{3+} ions is weakly antiferromagnetic.

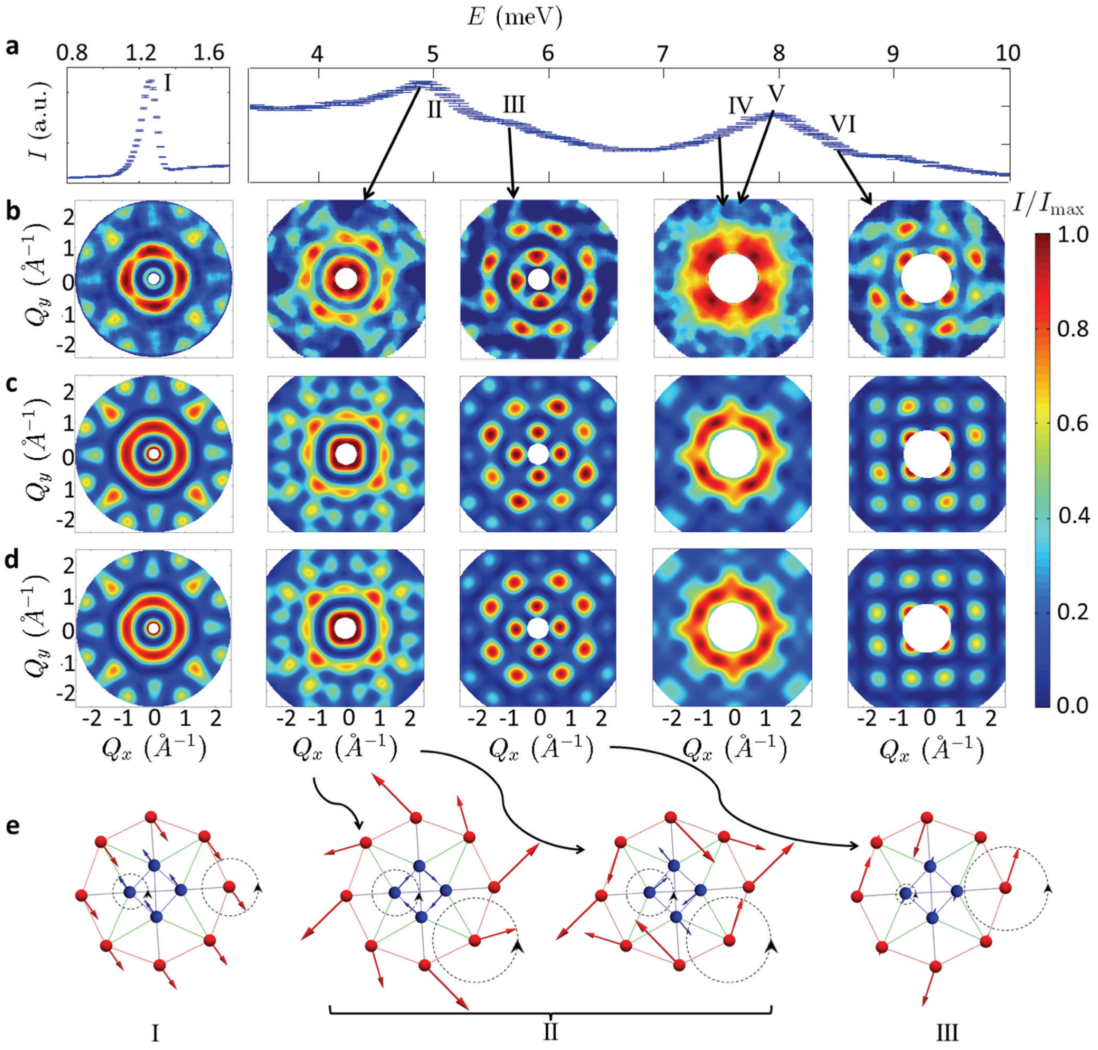

Figure 3 | Portrays of eigenvectors. **a,** INS energy spectrum. **b,** constant-energy cuts for S(E,**Q**), integrated over the full Q_z range, obtained from measurements at incident neutron energies of 4.2 meV (first column, peak **I**) and 15.4 meV (peaks **II**, **III**, **IV**, **V**, **VI**). Each map is normalized to its maximum. **c,** corresponding simulated maps, obtained with parameters (in meV) J_1 = -1.2 (1), J_2 = 3.2 (2), J_3 = 6.6 (3), J_4 = 0.55 (5), J_4' = 0.30 (5) , d=-0.315 (2). Eigenstates are listed in Extended Data Table 1. Row **d** highlights the effect of a slight variation of exchange parameters (J_4=J_4'=0.42 meV is assumed). Peaks **IV** and **V** are too close in energy to extract individual maps, and only their sum is addressed. **e**: precession pattern of the individual Mn spins for excitations **I**, **II** and **III**. For each excitation, arrows represent the twelve vectors $\left(\langle s_{xn}\rangle(t), \langle s_{yn}\rangle(t)\right)$ describing the spatial pattern of the spins preceding around *z*, after a resonant perturbation has brought a molecule from its $M = 10$ ground state into a superposition state with a small component on the corresponding excited $M = 9$ state. All the spins precede with the same frequency *E/h* and dashed circular arrows indicate the direction of the spin precessions for two representative sites. Preparing the system in an initial state with opposite M would induce an opposite precession of the spins. The two panels for excitation **II** correspond to a pair of degenerate states (Extended Data Table 1). For peaks **IV**, **V** and **VI** experimental form factors are more noisy or unresolved. Their precession pattern is not directly deduced from data, and is obtained by simulations of the best-fit Hamiltonian (Extended Data Fig. 2).

The information on eigenstates is so rich that even subtle variations of exchange parameters alter these maps. For instance, a single parameter is usually assumed for the external Mn^{3+} ring, i.e., $J_4=J_4'$ in Fig. 1a. Although these constants are an order of magnitude smaller than the leading ones, we can quantify J_4 and J_4' separately. The effect of the difference J_4-J_4' stands out in Fig. 3, showing also (panel d) simulations obtained with $J_4=J_4'$ = 0.42 meV. The intensity distribution in the intermultiplet maps is noticeably different, reflecting a change in composition of the excited S=9 multiplets. It is worth noting that small model variations of this type have significant impact on these maps, but negligible effects on the energy spectrum and susceptibility.

The information on eigenstates collected in reciprocal space (E, $\mathbf{Q}$) can be made intuitive by using an equivalent description in terms of time and position variables, i.e., by portraying the precession pattern of the twelve Mn spins associated with each excitation. Indeed, the **Q** dependence of a peak at energy E reflects the spatial pattern of the spins preceding around z with frequency E/h, after a resonant perturbation has brought a molecule from its $M = 10$ ground state into a superposition state with a small component on the corresponding excited $M = 9$ state (see Methods). Such patterns directly extracted from experimental data are shown in Fig. 3e and represent the molecular counterpart of spin wave excitations occurring in a bulk ferromagnet. The difference in the spin dynamics associated to the various transitions is evident: in transition **I** all the spins rigidly precess conserving the same total-spin modulus of the ground state, as expected for a giant spin excitation. Conversely, the precession pattern of all the other peaks is characterized by a zero total spin, demonstrating the inter-multiplet nature of the transitions. In addition, the different symmetries of the excited states (labeled with k in Extended Data Table I) produce clear signatures in the precession patterns.

The present results finally characterize the exchange interactions in the archetypal SMM Mn_{12} enabling to draw for the first time a sound picture of the eigenstates beyond the giant spin model. This will be the starting point to address important issues in the understanding of this molecule, which are still not really solved after more than twenty years of research. For instance, the relaxation dynamics of Mn_{12} should be influenced by the low-lying excited multiplets, partially overlapping with the ground one (e.g., these lead to additional relaxation and tunneling pathways with respect to the giant spin model). In general, these results open remarkable perspectives in understanding nanomagnets with complex polycentric core. These are still relatively little explored and understood but are of fundamental importance, with potential applications in the longer term. We mention among others molecules where the role of anisotropy is not perturbative, like in presence of Co (30) or f-electron ions (17). These can convey their large anisotropy through exchange to the whole core, thus producing large anisotropy barriers or exotic magnetic states (e.g., toroidal or chiral). On the opposite side, we mention small-anisotropy molecules where the pattern of exchange couplings results in frustration, which is important both for fundamental and applicative issues (15). More generally, experiments such as the present one show that 4D-INS is an unrivalled tool for characterizing magnetic clusters where the size and complexity of the spin structure make impossible or ambiguous the interpretation by more conventional routes.

1. Sessoli, R., Gatteschi, D., Caneschi, A. & Novak, M. A. Magnetic bistability in a metal-ion cluster. Nature 365, 141-143 (1993).

2. Thomas, L., Lionti, F., Ballou, R., Gatteschi, D., Sessoli, R. & Barbara, B. Macroscopic quantum tunnelling of magnetization in a single crystal of nanomagnets. Nature 383, 145-147 (1996).

3. Leuenberger, M. N. & Loss, D. Quantum computing in molecular magnets. Nature 410, 789-793 (2001).

4. Thiele, S., Balestro, F., Ballou, R., Klyatskaya, S., Ruben M. & Wernsdorfer, W. electrically driven nuclear spin resonance in single-molecule magnets. Science 344, 1135-1138 (2014) .

5. Shiddiq, M., Komijani, D., Duan, Y., Gaita-Ariño, A., Coronado, E. & Hill, S. Enhancing coherence in molecular spin qubits via atomic clock transitions. Nature, 531, 348–351 (2016) .

6. Cervetti, C., Rettori, A., Pini, M. G., Cornia, A., Repolles, A., Luis, F., Dressel, M., Rauschenbach, S., Kern, K., Burghard, M. & Bogani, L. The classical and quantum dynamics of molecular spins on graphene. Nature Mater. 15, 164-168 (2016).

7. Baker, M. L., Guidi, T., Carretta, S., Ollivier, J., Mutka, H., Güdel, H. U., Timco, G. A., McInnes, E. J. L., Amoretti, G., Winpenny, R. E. P., Santini, P. Spin dynamics of molecular nanomagnets unravelled at atomic scale by four-dimensional inelastic neutron scattering. Nature Phys. 8, 906 (2012).

8. Wernsdorfer, W. & Sessoli, R. Quantum phase interference and parity effects in magnetic molecular clusters. Science 284, 133-135 (1999).

9. Wernsdorfer, W., Murugesu, M. & Christou, G. Resonant Tunneling in Truly Axial Symmetry Mn12 Single-Molecule Magnets: Sharp Crossover between Thermally Assisted and Pure Quantum Tunneling. Phys. Rev. Lett. 96, 057208 (2006).

10. Carretta, S., Guidi, T., Santini, P., Amoretti, G., Pieper, O., Lake, B., van Slageren, J., El Hallak, F., Wernsdorfer, W., Mutka, Russina, H. M., Milios, C. J. & Brechin, E. K. Breakdown of the Giant Spin Model in the Magnetic Relaxation of the Mn6 Nanomagnets. Phys. Rev. Lett. 100, 157203 (2008).

11. Furrer, A. & and Waldmann, O. Magnetic cluster excitations. Rev. Mod. Phys. 85, 367 (2013).

12. Luzon, J., Bernot, K., Hewitt, I. J., Anson, C. E., Powell, A. K. & Sessoli, R. Spin chirality in a molecular dysprosium triangle: the archetype of the noncollinear ising model. Phys. Rev. Lett. 100, 247205 (2008).

13. Ungur, L., Langley, S. K., Hooper, T. N., Moubaraki, B., Brechin, E. K., Murray, K. S. & Chibotaru, L. F. Net toroidal magnetic moment in the ground state of a {Dy6}-triethanolamine ring. J. Am. Chem. Soc. 134, 18554-7 (2012).

14. Garlatti, E., Guidi, T., Ansbro, S., Santini, P., Amoretti, G., Ollivier, J., Mutka, H., Timco, G., Vitorica-Yrezabal, I., Whitehead, G., Winpenny, R. & Carretta, S. Portraying entanglement between molecular qubits with four-dimensional inelastic neutron scattering. Nature Commun. 8:14543 (2017).

15. Schröder, C., Schmidt, H.-J., Schnack, J. & Luban, M. Metamagnetic Phase Transition of the Antiferromagnetic Heisenberg Icosahedron. Phys. Rev. Lett. 94, 207203 (2005).

16. Carretta, S., Santini, P., Amoretti ,G., Guidi, T., Copley, J. R., Qiu, Y., Caciuffo, R., Timco G. & Winpenny, R. E. Quantum oscillations of the total spin in a heterometallic antiferromagnetic ring: evidence from neutron spectroscopy. Phys. Rev. Lett. 98, 167401 (2007).

17. Dutkiewicz M. S., Farnaby, J. H., Apostolidis, C., Colineau, E., Walter, O., Magnani, N., Gardiner, M. G., Love, J. B., Kaltsoyannis, N., Caciuffo, R. & Arnold, P. L. Organometallic neptunium(III) complexes. Nature Chem. 8, 797-802 (2016).

18. Caciuffo, R., Amoretti, G., Murani, A., Sessoli, R., Caneschi, A. & Gatteschi, D. Neutron Spectroscopy for the Magnetic Anisotropy of Molecular Clusters. Phys. Rev. Lett. 81, 4744 (1998).

19. Mirebeau, I., Hennion, M., Casalta, H., Andres, H., Güdel, H. U., Irodova, A. V. & Caneschi, A. Low-Energy Magnetic Excitations of the Mn12-Acetate Spin Cluster Observed by Neutron Scattering. Phys. Rev. Lett. 83, 628 (1999).

20. Molecular Magnetic Materials: Concepts and Applications (eds Sieklucka, B., & Pinkowicz, D.) (Wiley-VCH, 2017).

21. Barra, A.-L., Caneschi, A., Cornia, A., Gatteschi, D., Gorini, L., Heiniger, L.-P., Sessoli, R. & Sorace, L. The Origin of Transverse Anisotropy in Axially Symmetric Single Molecule Magnets. J. Am. Chem. Soc. 129, 10754-10762 (2007).

22. Mazurenko, V., Kvashnin, Y. O., Jin, F., De Raedt, H. A., Lichtenstein, A. I. & Katsnelson, M. I. First-principles modeling of magnetic excitations in Mn12 . Phys. Rev. B 89, 214422 (2014).

23. Tabrizi, S. G., Arbuznikov, A V.. & Kaupp, M. Understanding Thermodynamic and Spectroscopic Properties of Tetragonal Mn12 Single-Molecule Magnets from Combined Density Functional Theory/Spin-Hamiltonian Calculations. J. Phys. Chem. A 120, 6864-6879 (2016).

24. Hanebaum, O. & Schnack, J. Thermodynamic observables of Mn12-acetate calculated for the full spin Hamiltonian. Phys. Rev. B 92, 064424 (2015).

25. Chaboussant, G., Sieber, A., Ochsenbein, S., Güdel, H.-U., Murrie, M., Honecker, A., Fukushima, N. & Normand, B. Exchange interactions and high-energy spin states in Mn12-acetate. Phys. Rev. B 70, 104422 (2004).

26. Lampropoulos, C., Murugesu, M., Harter, A. G., Wernsdofer, W., Hill, S., Dalal, N. S., Reyes, A. P., Kuhns, P. L., Abboud, K. A. & and Christou, G. Synthesis, Structure, and Spectroscopic and Magnetic Characterization of $[Mn_{12}O_{12}(O_2CCH_2Bu^t)_{16}(MeOH)_4]\cdot MeOH$, a Mn12 Single-Molecule Magnet with True Axial Symmetry. Inorg. Chem. 52, 258-272 (2013).

27. Waldmann,O., Bircher, R., Carver, G., Sieber, A., Güdel, H. U. & Mutka, H. Exchange-coupling constants, spin density map, and Q dependence of the inelastic neutron scattering intensity in single-molecule magnets. Phys. Rev. B 75, 174438 (2007).

28. Robinson, R. A., Brownd, P. J., Argyriou D. N., Hendrickson, D. N. & Aubin, S. M. J. Internal magnetic structure of Mn12 acetate by polarized neutron diffraction. J. Phys.: Condens. Matter 12, 2805 (2000).

29. Furukawa, Y., Watanabe, K., Kumagai, K., Borsa, F. & Gatteschi, D. Magnetic structure and spin dynamics of the ground state of the molecular cluster Mn12O12 acetate studied by 55Mn NMR. Phys. Rev. B 64, 104401 (2001).

30. Murrie, M. Cobalt(II) single-molecule magnets. Chem. Soc. Rev. 39, 1986–1995 (2010).

Acknowledgments

We gratefully acknowledge Dr. Peixun Li for the preparation of deuterated products. A.C., S.C., E.G., G.A. and P.S acknowledge financial support from the FIRB Project No. RBFR12RPD1 and PRIN Project 2015 No. HYFSRT of the Italian Ministry of Education and Research. G.T., I.J.V.-Y. and R.E.P.W. thank the EPSRC(UK) for support, including funding for an X-ray diffractometer (grant number EP/K039547/1).

Author Contributions

S.C., T.G., G.A., R.E.P.W. and P.S. conceived and proposed the experiment. T.G. and S.A. performed the experiment on crystals synthesized by G.T. after discussion with R.E.P.W. The structure determination and crystal alignment were performed by I.J.V.-Y. Data treatment was made by A.C., S.C., T.G. and S.A. Calculations and fits were performed by A.C., S.C., E.G., G.A. and P.S., while A.C., S.C. and P.S. wrote the manuscript with inputs from all coauthors.

METHODS

Materials. Unless stated otherwise, all reagents and solvents were commercially available and used as received. Deuterated *t*-butylacetic acid $(CD_3)_3CCD_2COOH$ (D%=97%) was supplied by the ISIS Deuteration Facility (formerly the Oxford Isotope facility UK) and methanol-D4 (D%=98.8%) was purchased from Sigma-Aldrich. $[Mn_{12}O_{12}(O_2CMe)_{16}(H_2O)_4]\cdot 2MeCO_2H\cdot 4H_2O$ (**1**) was prepared as described in Lis, T. Acta Crystallogr., Sect. B: Struct. Sci. 1980, 36, 2042.

Synthesis. The synthesis and crystallization of $[Mn_{12}O_{12}(O_2CCD_2C(CD_3)_3)_{16}(CD_3OD)_4]$ were adapted from published methods (26). Vacuum-dried powder of **1** (1.0 g) was stirred with CD_3OD (85 mL) at∼30°C for 10 min, then the $(CD_3)_3CCD_2COOH$ (10 mL) was added and the reaction mixture was stirred at ∼30°C for 1 hour and the solution was filtered. The filtrate was allowed to stand undisturbed for 5 days at ambient temperature, during which time black needles of Mn_{12}-^{t}BuAc•CD_3OD slowly grew. These were collected by filtration, washed with CD_3OD (3 x 3 mL), and dried in N_2 flow; the yield was 1.07g (~70%). Single-large crystals preparation of Mn_{12}-^{t}BuAc: 1.0g of $[Mn_{12}O_{12}(O_2CCD_2C(CD_3)_3)_{16}(CD_3OD)_4]$ was dissolved in diethyl ether (30 mL) and filtered. To the filtrate were added CD_3OD (10 mL) and $(CD_3)_3CCD_2COOH$ (0.1 mL), and the solution was stirred briefly. Then the solution was left undisturbed at ambient temperature under a flow of nitrogen for slow evaporation for one week, during which time several large well-shaped needle-shaped crystals grew alongside many small crystals.

Elemental analysis for single several crystals dried in a flow of N_2, calculated (%) for $C_{100}D_{192}Mn_{12}O_{48}$,Mn 21.86, C 39.84; found: Mn 21.43, C 40.17. To obtain sufficient large crystals of Mn_{12}-^{t}BuAc for the INS experiment, the synthesis was repeated twice and the crystallizations several times. Analytical data were obtained by the microanalysis laboratory at the University of Manchester—carbon, hydrogen, nitrogen analysis (CHN) by a Flash 2000 elemental analyser and metals analysis by Thermo iCap 6300 inductively coupled plasma optical emission spectroscopy (ICP-OES).Thermo Fisher Scientific "Exactive Plus EMR Orbitrap" mass spectrometer was used for mass spectrometry analysis. A standard Electrospray/ APCI techniques have delivered poor results. The ion source was instead modified to include a krypton lamp generating photons of ~10 eV. The samples were dissolved in toluene and injected into the mass spectrometer ion source. Created photoions were detected using electrostatic trap with mass resolution (~140000) and a precision of <5 ppm for mass measurements.

X-ray Crystallography. Single crystal X-ray diffraction data were collected at a temperature of 150 K using Mo-Kα radiation on an Agilent Supernova, equipped with an Oxford Cryosystems Cobra nitrogen flow gas system. Data were measured using CrysAlisPro suite of programs.

X-ray data was processed and reduced using CrysAlisPro suite of programs for crystal Mn_{12}. An absorption correction was performed using empirical methods based upon symmetry-equivalent reflections combined with measurements at different azimuthal angles using SCALE3 ABSPACK. The crystal structure was solved and refined against all F^2 values using the SHELX and Olex 2 suite of programs (31)(32). All the non-hydrogen atoms were refined anisotropically. Hydrogen atoms were placed in calculated positions and refined using idealized geometries (riding model) and assigned fixed isotropic displacement parameters. The C-C and C-O distances of the diethyl ether solvent molecule were restrained using DFIX command. The atomic displacement parameters were also restrained using SHELX commands SIMU and RIGU. Crystallographic information can be found in Extended Data Table 2.

CCDC 1544899 contains the supplementary crystallographic data for this paper. These data can be obtained free of charge via www.ccdc.cam.ac.uk/conts/retrieving.html (or from the Cambridge Crystallographic Data Centre, 12 Union Road, Cambridge CB21EZ, UK; fax: (+44)1223-336-033; or deposit@ccdc.cam.ac.uk).

Neutron scattering experiments. The INS measurements were performed on the LET time-of-flight spectrometer at the at ISIS neutron spallation source (33). The LET instrument is characterized by a π–steradiants bank of position sensitive detectors divided in about 10^5 pixels, covering 180° in the horizontal plane and ±30° out-of plane. A collection of deuterated single crystals were aligned on Aluminum sample holder with the ab-plane horizontal. The presence of both orientations of the [001] axis in the collection of crystals was taken into account in the simulations. The dimensions of the crystals ranged from a minimum of 4 mm^3 to a maximum of 40 mm^3. Measurements were performed by rotating the crystals (in steps of 2^o) about the vertical axis, labelled *z* in the laboratory frame.

The intramultiplet excitation **I**, centered at 1.2 meV, was studied with E_i = 4.2 meV, yielding an energy resolution (full-width at half-maximum) of 0.06 meV at the elastic line. Higher-energy intermultiplet transitions **II-VI** were detected by using E_i = 15.4 meV, corresponding to a resolution of 0.8 meV at the elastic line. Measurements for different rotation angles were then combined using the HORACE analysis suite (34). Corrections for attenuation as a function of rotation and scattering angle were performed by using the intensity modulations of the background signal.

To extract the maps of Fig. 2b and 3, for each (Q_x, Q_y) the energy dependence was fitted with gaussians plus a background contribution. This allowed us to separate excitations close in energy (like peaks **II** and **III**), and the **Q**-dependence of the inelastic peaks from that of the background. Since excitations **IV** and **V** are too close in energy to extract individual maps, only their sum was considered.

This Mn_{12} variant implies a fourfold symmetry in the (Q_x, Q_y) dependence of the intensity of magnetic excitations (see Extended Data Fig. 1). We have exploited the fourfold axis and summed together the cross-sections obtained for wavevectors equivalent by rotations, in order to improve data statistics. The data in Fig. 2 and 3 have been plotted exploiting the fourfold symmetry for presentation purposes.

Calculation techniques. Since the dimension of the full Hilbert space of Mn_{12} is huge (10^8), and a large number of calculations is needed to fit the model parameters, we have exploited group theory, Lanczos diagonalization and irreducible tensor operators techniques. The latter are useful to take advantage of the isotropic nature of the dominant term in the Hamiltonian. In addition, a parallelization on several cores has been employed in the exploration of the parameters space. At last, the magnetic susceptibility has been calculated by the finite-temperature Lanczos method (24) at high and intermediate temperatures, while exact diagonalization of the lowest multiplets has been employed in the low temperature region (where anisotropy becomes relevant).

Determination of the model parameters. Information on the spectrum of Eq. (1) is obtained, at low energy, from INS data (Fig. 1b and 3b) and, at higher energies, from the room-temperature susceptibility [Fig. 1c, $\chi T \sim 20$ emu/mol (26)]. The latter provides a single, integrated piece of information on the structure of the spectrum in the high-*E* region not investigated in the present experiment. The structure of the eigenstates of Eq. (1), extracted from the maps of Fig. 3b, is crucial for a univocal fit. Indeed, we find several regions of the parameters space fitting the INS spectrum well, but we can restrict to a single one only by comparing the corresponding form factors with the measured ones. After identifying the best region, we use iteratively perturbation theory (with respect to small parameters variations) and full calculations to fine-tune the values of exchange couplings. As far as anisotropy is concerned, its primary effect is that of a first-order perturbation with respect to exchange, producing a splitting of the various total-spin multiplets. The effect on the probed wavefunctions is small, implying that the maps of Figs. 2 and 3 (as well as the local moment distribution) are set by exchange and depend little on the anisotropic part of the Hamiltonian. For the model of Eq. (1), the value of *d* can thus be determined independently of exchange parameters, and is fixed by the energy of peak **I**. Within this model the position of peak **VI** (Fig. 1b) cannot be perfectly reproduced, and it is overestimated by about 3% with the final parameters set. Removing this small discrepancy requires a more complex anisotropic part in Eq. (1). For example, small nonaxial terms might mix the $|S=9, M=\pm 9\rangle$ states (peak **VI**) with nearby $|S=8, M=\pm 8\rangle$ states (not visible in INS), and result in a slight decrease in energy of peak **VI** without affecting its INS form-factor. The best-fit exchange parameters will then remain the same we determined.

Extracting real-space information from form factors. The zero-temperature INS cross-section is

$$S(E,\mathbf{Q}) \propto \sum_{\alpha,\beta}\left(1-\frac{Q_\alpha Q_\beta}{Q^2}\right)\sum_p\sum_{m,n} F_n(Q)F_n(Q)\exp(i\mathbf{Q}\cdot\mathbf{R}_{mn})\langle 0|s_{\alpha m}|p\rangle\langle p|s_{\beta n}|0\rangle\delta(E-E_p), \quad (2)$$

where $|0\rangle$ is the ground state, *p* labels excited states (of energy E_p), *m* and *n* run over the twelve Mn ions, $\mathbf{R}_{mn}$ are relative positions and F_n are single-ion form factors. In axial symmetry [Eq. (1)], $\alpha \equiv \beta = x, y$. $S(E,\mathbf{Q})$ depends on the molecular structure through $\mathbf{R}_{mn}$, whereas the spin-Hamiltonian [Eq. (1)] sets E_p and eigenvectors $|p\rangle$. If the effect of anisotropy is perturbative, the Wigner-Eckart theorem allows one to parametrize the matrix elements of local spins in terms of reduced matrix elements, e.g.,

$$\langle 0|s_{xn}|p\rangle \equiv \langle \alpha, S, M=10|s_{xn}|\alpha', S', M'=9\rangle = \frac{(-1)^{S-M+1}}{\sqrt{2}}\begin{pmatrix} S & 1 & S' \\ -M & 1 & M' \end{pmatrix}\langle \alpha, S\| \, T^1(n)\|\alpha', S'\rangle$$

In Mn_{12}, for each INS transition there are three independent reduced elements $\langle \alpha, S\|T^1(d)\|\alpha', S'\rangle$, corresponding to three inequivalent Mn sites. Thus, form factors (Figs. 2 and 3) provide information on the structure of the spin-multiplets through these elements, whose value is set by the exchange parameters in Eq. (1). It is worth to note that the $\langle \alpha, S\|T^1(d)\|\alpha', S'\rangle$ coefficients can be directly extracted by fitting the measured $\mathbf{Q}$ dependence of each transition with Eq. (2), where they constitute the only unknown quantities. For the intramultiplet peak **I**, this real-space information is equivalent to that contained in the static local-moments distribution, $\langle 0|s_{zn}|0\rangle$, which can then be inferred directly from INS data (Fig. 2a).

For any INS transition, the corresponding excitation can be visualized by the oscillation pattern of Mn spins inferred by its form-factor. If we imagine a set of molecules in their ground state $|0\rangle$ (either $|M = 10\rangle$ or $|M = -10\rangle$) brought to a superposition state $\alpha|0\rangle + \beta|p\rangle$ (e.g., by a weak pulse of inhomogeneous transverse field of frequency $E_p/\hbar$), the subsequent evolution of the average local moments ($\langle s_{xn}\rangle(t)$ and $\langle s_{yn}\rangle(t)$) describes a precession of the twelve spins about the *z* axis (Figs. 3e and Extended Data Fig. 2). This is analogous to the Larmor precession of a single spin or to that characterizing spin wave excitations in a bulk ferromagnet. These precession patterns are in a one to one correspondence with the form factor $S(E_p, \mathbf{Q})$, as both are set by the three reduced matrix elements. For a generic weak perturbation (e.g., a δ-pulse), the resulting motion is a weighted superposition of these single-frequency contributions. In the case of doubly-degenerate final states $|p\rangle$, like for peaks **II** and **V**, (two-dimensional representations, see Extended Data Table 1), the set of reduced elements for the two states are related by symmetry to each other, hence the total form factor is still parametrized by three coefficients.

31. Sheldrick, G. M. Crystal structure refinement with SHELXL. Acta Crystallogr., 2015, C71, 3-8.

32. Dolomanov, O. V., Bourhis, L. J., Gildea, R. J., Howard, J. A. K., Puschmann, H. OLEX2: a complete structure solution, refinement and analysis program, J. Appl. Cryst., 2009, 42, 339–341.

33. Bewley, R. I., Taylor, J. W., Bennington, S. M. LET, a cold neutron multi-disk chopper spectrometer at ISIS. Nuclear Instruments and Methods in Physics, 637 128-134 (2011).

34. Ewings, R. A., Buts, A., Lee, M. D., van Duijn, J., Bustinduy, I. & Perring, T. G. Horace: Software for the analysis of data from single crystal spectroscopy experiments at time-of-flight neutron instruments. Nuclear Instruments and Methods in Physics Research Section A: Accelerators, Spectrometers, Detectors and Associated Equipment, 834 132-142 (2016).

EXTENDED DATA

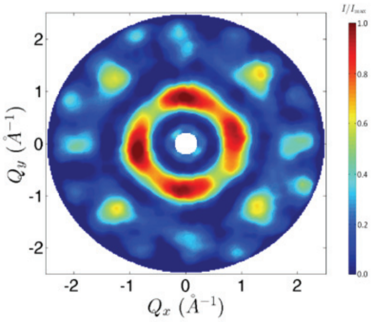

Extended Data Figure 1 | Measured Q_x-Q_y dependence of the form factor for peak I. The expected C_4 symmetry of the map is clear within experimental errors. This allows us to fold the map into a single quarter in order to increase the statistics of the data. Data are integrated over the full Q_z range.

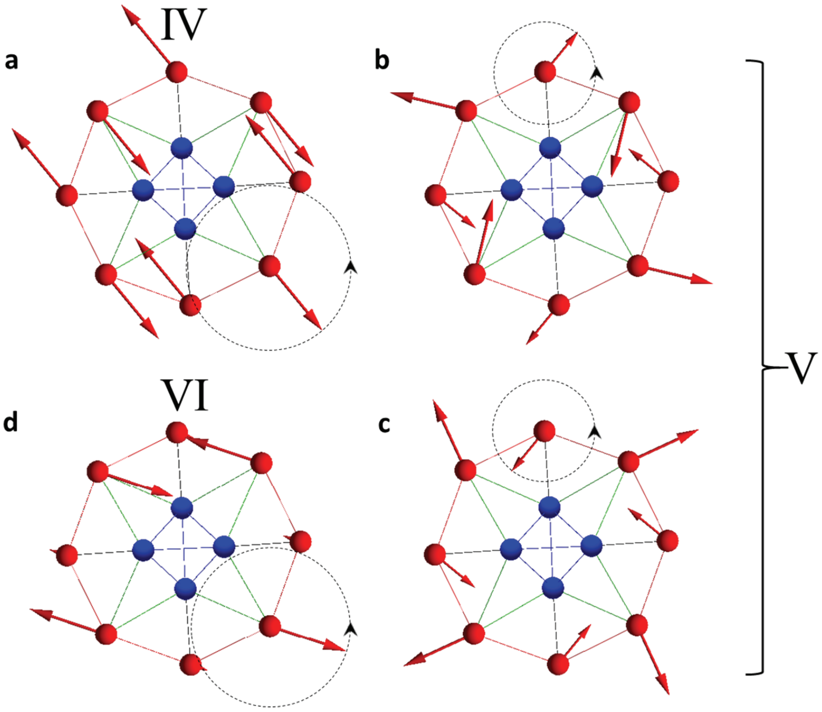

Extended Data Figure 2 | Precession pattern for high-energy excitations. The pattern is shown for spin excitations corresponding to peaks **IV** (**a**), **V** (**b**, **c**) and **VI** (**d**).

State	**Composition (main contributions)**	**E (meV)**
$\left\|S=10,\ k=0\right\rangle$	$\left\|6,16\right\rangle(65\%),\quad \left\|5,15\right\rangle(26\%),\quad \left\|4,14\right\rangle(5\%)$	0
$\left\|S=9,\ k=\pm\pi/2\right\rangle$ *	$\left\|6,15\right\rangle(53\%),\quad \left\|5,14\right\rangle(31\%),\quad \left\|4,13\right\rangle(7\%)$	4.79
$\left\|S=9,\ k=\pi\right\rangle$	$\left\|6,15\right\rangle(58\%),\quad \left\|5,14\right\rangle(30\%),\quad \left\|4,13\right\rangle(7\%)$	5.77
$\left\|S=9,\ k=0\right\rangle$	$\left\|6,15\right\rangle(64\%),\quad \left\|5,14\right\rangle(27\%),\quad \left\|4,13\right\rangle(5\%)$	7.52
$\left\|S=9,\ k=\pm\pi/2\right\rangle$ *	$\left\|6,15\right\rangle(63\%),\quad \left\|5,14\right\rangle(27\%),\quad \left\|4,13\right\rangle(3\%)$	7.90
$\left\|S=9,\ k=\pi\right\rangle$	$\left\|6,15\right\rangle(63\%),\quad \left\|5,14\right\rangle(27\%),\quad \left\|4,13\right\rangle(5\%)$	8.60

Extended Data Table 1 | Composition of the low-energy multiplets of Mn_{12}. The first column contains total-spin multiplets labeled with their total spin *S* and symmetry *k*. A rotation by π/2 around the z-axis multiplies the state by a phase factor e^{ik}. Stars indicate two-fold degenerate total-spin multiplets. The second column reports the composition of these multiplets in terms of $\left|s_i, s_e\right\rangle$, the total spins of the internal (Mn^{4+}) and external (Mn^{3+}) sublattices. The last column reports the energy of the M = ± S eigenstates obtained from diagonalization of the Hamiltonian (1).

Crystal colour	dark
Crystal size (mm)	0.65 × 0.28 × 0.27
Crystal system	tetragonal
Space group, *Z*	I-4, *2*
a (Å)	21.4901(4)
c (Å)	15.1885(5)
V (Å^3)	7014.4(3)
Density (Mg.m^{-3})	1.463
Wavelength (Å)	0.71073
Temperature (K)	150
μ(Mo-Kα) (mm^{-1})	1.116
2Θ range (°)	7.344 to 50.63
Reflections collected	12634
Independent reflections (R_{int})	6196 (0.0314)
Least square parameters, *p*	415

No. of restraints, r	60
$R1$ $(F)^{a}$ $I > 2.0\sigma(I)$	0.0355
$wR2(F^2)$,[b] all data	0.0767
$S(F^2)$,[c] all data	1.046

[a] $R1(F) = \Sigma(|F_o| - |F_c|)/\Sigma|F_o|$; [b] $wR2(F^2) = [\Sigma w(F_o^2 - F_c^2)^2/\Sigma wF_o^4]^{½}$; [c] $S(F^2) = [\Sigma w(F_o^2 - F_c^2)^2/(n + r - p)]^{½}$

Extended Data Table 2 | Crystallographic information for Mn12.

Chapter 5 Entanglement Unravelled by INS

5.1 Entangled Dimer Background

The Cr_7Ni antiferromagnetic ring is one of the most widely studied molecular nanomagnets since it represents a prototypical qubit for quantum information processing. A qubit is a two-level quantum mechanical system that analogously takes on the same role in quantum computing that a conventional bit does in classical computing[6]. Qubits differ from our everyday classical counterparts in that instead of just taking on the binary logic states of 0 or 1, they also take on any quantum superposition of these states and thus an N-qubit system is empowered by drawing on 2^N states for computation. In the case of the Cr_7Ni ring, the well-isolated ground state behaves as an effective S=1/2 which splits in a magnetic field, providing a two level system. Furthermore Cr_7Ni has also been shown to have decoherence times long enough for spin manipulation in quantum information processes[31].

The DiVincenzo criteria[68,69] details these properties amongst some of the key requirements for practical quantum information processing and are as follows:

1) *A scalable physical system with well characterised qubits*

We require a system composed of qubits, whose two-level system is well defined. We must also be able to add to the number of qubits accordingly to scale up the processing power.

2) *The ability to initialise the state of the qubits to a simple fiducial state, such as* $|000\ldots\rangle$

This requires us to be able to initiate a calculation from the same reference state which must be a pure state. Much like in classical computing it is necessary to reset in order to perform an accurate computation.

3) *Long relevant decoherence times, much longer than the gate operation time*

Eventually the fragile quantum state will degrade due to external disturbance from its environment and places a limit on the time available to perform a calculation. This is usually the greatest challenge for those looking at potential prototypes for quantum computing.

4) *A "universal" set of quantum gates*

The implementation of gate operations such as the CNOT gate is essential for the implementation of quantum algorithms. For two-qubit gates there exists the necessity to entangle the qubits.

5) *A qubit-specific measurement capability*

The ability to read out each individual qubit after a calculation, without perturbing any of the other qubits.

Whilst Cr_7Ni has been demonstrated to address the majority of these challenges, the necessity to entangle these molecular spin units is still an area in need of further enquiry since this is the essential resource in quantum information processing[70]. One approach to addressing this is through the tying together of the molecular spin units through coordination chemistry. A particularly interesting example of such a molecule is the pyrazine-linked dimer $[Cr_7NiF_3(C_7H_{12}NO_5)(O_2CC(CH_3)_{15})]_2(N_2C_4H_4)$. This molecule therefore represents the tying together of two prototypical qubits, holding them very closely together at a distance of 8.26 Å (through bond)[32].

The natural protection of the spin degrees of freedom, high potential for chemical modification and scalability has allowed such molecular nanomagnets to show great promise over other suggested forms of prototypical qubits. To press onwards though, the identification and quantification of entanglement in these systems is of paramount importance if future suitable molecular spin clusters are to be implemented in these technologies. This paper shows that state-of-the-art INS is ready to address this challenge by going beyond previous indirect macroscopic measurements by directly characterising the inter-ring entanglement through the Q-dependence. It also allows us to go further as we additionally demonstrate a method to quantify this entanglement.

nature COMMUNICATIONS

ARTICLE

Received 13 Jun 2016 | Accepted 10 Jan 2017 | Published 20 Feb 2017 DOI: 10.1038/ncomms14543 OPEN

Portraying entanglement between molecular qubits with four-dimensional inelastic neutron scattering

E. Garlatti[1], T. Guidi[2], S. Ansbro[3,4], P. Santini[1], G. Amoretti[1], J. Ollivier[3], H. Mutka[3], G. Timco[4], I.J. Vitorica-Yrezabal[4], G.F.S. Whitehead[4,†], R.E.P. Winpenny[4] & S. Carretta[1]

Entanglement is a crucial resource for quantum information processing and its detection and quantification is of paramount importance in many areas of current research. Weakly coupled molecular nanomagnets provide an ideal test bed for investigating entanglement between complex spin systems. However, entanglement in these systems has only been experimentally demonstrated rather indirectly by macroscopic techniques or by fitting trial model Hamiltonians to experimental data. Here we show that four-dimensional inelastic neutron scattering enables us to portray entanglement in weakly coupled molecular qubits and to quantify it. We exploit a prototype $(Cr_7Ni)_2$ supramolecular dimer as a benchmark to demonstrate the potential of this approach, which allows one to extract the concurrence in eigenstates of a dimer of molecular qubits without diagonalizing its full Hamiltonian.

---

[1] Dipartimento di Scienze Matematiche, Fisiche ed Informatiche, Università di Parma, I-43124 Parma, Italy. [2] ISIS facility, Rutherford Appleton Laboratory, OX11 0QX Didcot, UK. [3] Institut Laue-Langevin, 71 Avenue des Martyrs CS 20156, Grenoble Cedex 9 F-38042, France. [4] School of Chemistry and Photon Science Institute, The University of Manchester, M13 9PL Manchester, UK. † Present Address: Department of Chemistry, University of Liverpool, Liverpool L69 7ZD, UK. Correspondence and requests for materials should be addressed to S.C. (email: stefano.carretta@fis.unipr.it).

One of the most intriguing aspects of quantum mechanics are entangled states[1–3], which exhibit correlations that cannot be accounted for in classical physics. Entanglement occurs when a composite quantum object is described by a wave function that is not factorized into states of the object's components, making it impossible to describe a part of the system independently of the rest of it.

Recently, the concept of entanglement has been applied to many different areas of quantum many-body physics, including condensed matter[4,5], high-energy field theory[6] and quantum gravity[7]. In particular, the development of quantum information science[4,8] has largely increased the interest in the study of entanglement, since it represents an essential resource for quantum information processing applications. Thus, how to experimentally detect and quantify entanglement has become a crucial step for the development of quantum information protocols. However, experimental measurements of entanglement in complex systems are very difficult, because quantum state tomography[9] requires demanding resources and a high degree of control[10,11]. Recently, many theoretical and experimental works have focused on the detection of entanglement[12–19].

Arrays of weakly coupled molecular nanomagnets represent an ideal playground for investigating quantum entanglement between complex spin systems[4,20]. In particular, supramolecular complexes containing linked antiferromagnetic rings have been demonstrated to be excellent candidates for implementing quantum-computation[21] and quantum-simulation[22] algorithms (see also Supplementary Note 1). A large number of supramolecular complexes of molecular nanomagnets are now being synthesized, but so far entanglement between molecular subunits has only been experimentally demonstrated by exploiting susceptibility as a witness in a $(Cr_7Ni)_2$ dimer or by fitting trial model Hamiltonians to electron paramagnetic resonance data[23]. The dimer (see Fig. 1a) consists of two Cr_7Ni antiferromagnetic rings, and hence is a complex system made of 16 interacting spins, that is, one on each metal site. Strong exchange couplings between the eight spins within each ring lock these spins into a correlated $S=1/2$ ground state[24], which is preserved in the presence of sizeable magnetic fields. Importantly, a weaker inter-ring interaction leads to entanglement between the two composite molecular $S=1/2$ spins. The four-dimensional inelastic neutron scattering technique (4D-INS)[25] has the potential to provide a precise characterization of entanglement in such a system. Indeed, the crosssection directly reflects dynamical correlations between individual atomic spins in the molecule, and distinguishes between intra-ring correlations, associated with the composite nature of the molecular qubits, and inter-ring spin–spin correlations, which are a signature of entanglement between qubits.

Here we use this prototype $(Cr_7Ni)_2$ dimer as a benchmark system to demonstrate the capability of 4D-INS to investigate entanglement between molecular qubits. By assuming the rings maintain the $S=1/2$ ground doublets determined from previous measurements on single-rings[26], the richness of the experimental information enables us to quantify inter-ring entanglement in the eigenstates through the determination of their concurrence. A magnetic field is used to place the system into a factorized ground state of the two rings and test the occurrence of entanglement in a comfortable parameter regime. Indeed, in this way we can univocally attribute the observed inter-ring correlations to the entanglement in the excited states. This is

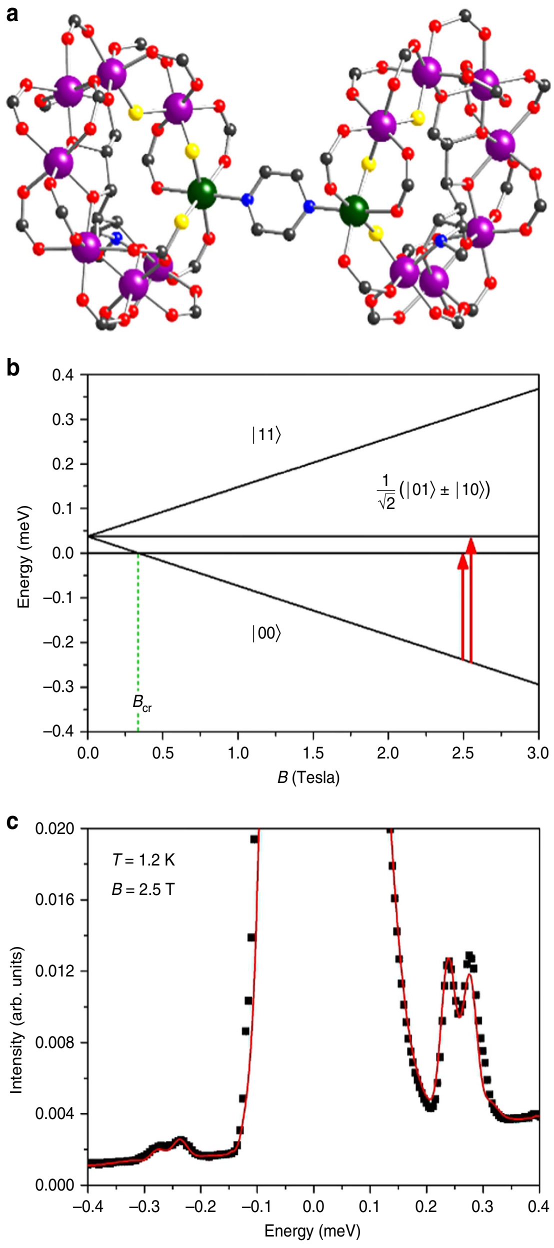

Figure 1 | The $(Cr_7Ni)_2$ dimer. (**a**) Molecular structure of the supramolecular dimer of formula $[Cr_7NiF_3(C_7H_{12}NO_5)(O_2CC(CH_3)_{15})]_2(N_2C_4H_4)$ (magenta, Cr; green, Ni; yellow, F; red, O; light blue, N; grey, C; $C(CH_3)_3$ groups and all H atoms omitted for clarity), consisting of two purple-(Cr_7Ni) AF rings, forming an angle of about 30°. The coupling between the rings is mediated by pyrazine, which directly links the two Ni ions. (**b**) Lowest-energy levels of the molecular dimer as a function of the applied magnetic field B, calculated by diagonalizing the microscopic spin Hamiltonian, equations (1 and 2). The arrows indicate the two transitions detected by in-field INS. $|0\rangle$ and $|1\rangle$ qubit states are encoded in the ground $|S=1/2, M=\pm 1/2\rangle$ doublet of each ring. Above $B_{cr}=0.34$ T the dimer ground state is a factorized ferromagnetic state. In the first two excited states the total spins ($S=1/2$) of the rings are entangled and correspond to two Bell states. (**c**) Measured INS spectrum (black points) and calculations (red line) for a collection of $(Cr_7Ni)_2$ crystals at $T=1.2$ K and $B=2.5$ T applied along the y-vertical axis, with an incident neutron wavelength $\lambda=7.5$ Å and integrated over the full range of measured Q. Excitations in both energy-gain and energy-loss sides of the spectrum are clearly visible.

possible because of the strong intra-ring couplings which preserve the $S = 1/2$ ground states. This approach can be applied also to dimers of more complex molecular qubits (described as pseudo-spin 1/2) and it does not require any assumption on the form of the interaction between the qubits.

Results

The $(Cr_7Ni)_2$ supramolecular dimer. The Cr_7Ni antiferromagnetic rings constitute the most studied family of molecular qubits[21,27–29]. The magnetic core is formed by seven Cr ions and one Ni ion arranged at the corners of an octagon. The dominant interaction is the nearest-neighbor antiferromagnetic exchange and leads to an isolated ground doublet behaving as a total spin $S = 1/2$, which can be used to encode a qubit. These molecules display coherence times sufficiently long for spin manipulations[29] and they have been proposed as prototype for implementing quantum gates[28,30] and quantum simulations[22].

Here we study the $[Cr_7NiF_3(C_7H_{12}NO_5)(O_2CC(CH_3)_{15})]_2(N_2C_4H_4)$ supramolecular dimer, where $N_2C_4H_4 = N$-methyl-D-glucamine (Fig. 1a). The synthesis of $(Cr_7Ni)_2$ is described in the 'Methods' section. The Cr_7Ni subunits have been fully characterized by INS and electron paramagnetic resonance spectroscopies and by low-temperature specific heat and magnetometry measurements[26]. This characterization shows, unequivocally, that the ground state is a $S = 1/2$ doublet and that it is the only state of the ring populated at the temperatures used in the present work. Indeed, the first excited multiplet lies at about 18 K. The Hamiltonian describing each Cr_7Ni molecule is (assuming the Ni ion on site 8)

$$H = J\sum_{i=1}^{6}\mathbf{s}(i)\cdot\mathbf{s}(i+1) + J'[\mathbf{s}(1)\cdot\mathbf{s}(8)+\mathbf{s}(7)\cdot\mathbf{s}(8)] + \sum_{i=1}^{8} d_i s_z^2(i) - \mu_B\sum_{i=1}^{8} g_i\mathbf{B}\cdot\mathbf{s}(i), \quad (1)$$

where $\mathbf{s}(i)$ is the spin operator of the the ith ion ($s = 3/2$ for Cr^{3+} and $s = 1$ for Ni^{2+}). The first two terms correspond to the dominant antiferromagnetic isotropic exchange interaction (with $J = 20$ K and $J' = 30$ K), while the third term describes the axial single-ion zero-field-splitting terms (with $d_{Cr} = -0.34$ K, $d_{Ni} = -7.3$ K and the z-axis perpendicular to the ring). The last term represents the Zeeman coupling with an external field B (with $g_{Cr} = 1.98$ and $g_{Ni} = 2.1$). The two Cr_7Ni rings are linked through a pyrazine unit, which provides two N-donor atoms binding to Ni centres in different rings. This leads to a weak exchange coupling between the Ni ions:

$$H_{int} = j\,\mathbf{s}(Ni_A)\cdot\mathbf{s}(Ni_B), \quad (2)$$

where A and B label the two rings. We have checked that the effects of the anisotropic zero-field-splitting terms on the results presented in this work are very small (see Supplementary Fig. 1), hence hereafter we neglect the third term in equation (1).

Figure 1b reports the calculated magnetic field dependence of the lowest-energy levels of $(Cr_7Ni)_2$. In the presence of an antiferromagnetic ring–ring coupling ($j > 0$), the supramolecular system is characterized by an entangled singlet ground state in zero applied field and by an excited triplet. Within this subspace each ring behaves as a total spin $S = 1/2$, because the strong intra-ring exchange interactions rigidly lock together the individual spins within each ring. This condition is preserved also in sizeable fields, which can then be used to induce (for $B > B_{cr}$) a factorized ferromagnetic ground state for the dimer. In this regime, by focusing on a specific low-temperature transition, we can selectively investigate the entanglement between the rings in the corresponding excited state. Indeed, the origin of the observed inter-ring correlations can be univocally attributed to the excited state involved in the transition (see below) because the ground state is factorized. Moreover, the application of a magnetic field significantly improves the experimental working conditions for detecting inter-ring interactions. In fact, it is easier to resolve a very small splitting δ between two peaks in the centre of the energy-transfer range (as it occurs in a sizeable field), than to observe a single-peak centred at δ (zero-field case), because it would be partially covered by the elastic signal.

Portraying entanglement with 4D INS. The 4D-INS technique[25] has the potential to yield a deep insight into the entanglement between molecular qubits, by measuring the 4D scattering function $S(\mathbf{Q},\omega)$ in large portions of the reciprocal $\mathbf{Q}$ space and in the relevant energy-transfer $\hbar\omega$ range. Indeed, the dependencies of the transition intensities on $\mathbf{Q}$ yield direct information on the dynamical spin–spin correlation functions[25]. The zero-temperature spin scattering function is ref. 31

$$S(\mathbf{Q},\omega) \propto \sum_{\alpha,\beta=x,y,z}\left(\delta_{\alpha,\beta} - \frac{Q_\alpha Q_\beta}{Q^2}\right)\sum_{p,d,d'} F_d(Q)F_{d'}(Q) \exp(i\mathbf{Q}\cdot\mathbf{R}_{dd'})\langle 0|s_\alpha(d)|p\rangle\langle p|s_\beta(d')|0\rangle\delta(\omega - E_p/\hbar), \quad (3)$$

where $F_d(Q)$ is the magnetic form factor for the dth ion, $|0\rangle$ and $|p\rangle$ are ground and excited eigenstates, respectively, E_p are eigenenergies and $\mathbf{R}_{dd'}$ are the relative positions of the N magnetic ions within the supramolecular dimer. The products of spin matrix elements are the Fourier coefficients of $T = 0$ dynamical correlation functions

$$\langle s_\alpha(d,t)s_\beta(d',0)\rangle = \sum_p \langle 0|s_\alpha(d)|p\rangle\langle p|s_\beta(d')|0\rangle e^{-iE_pt/\hbar}. \quad (4)$$

If $|0\rangle$ is a factorized reference state, and $|p\rangle$ is an excited state where the two rings are entangled, the dynamical correlations of equation (4) are non-zero also for pairs of spins where d is in one ring and d' in the other one. Conversely, these inter-ring correlations would be zero if the states of the two monomers were factorized also in $|p\rangle$, because the corresponding products of spin matrix elements would vanish. The spatial structure of these large-distance correlations produces short-Q modulations in $S(\mathbf{Q}, E_p/\hbar)$ through the $\exp(i\mathbf{Q}\cdot R_{dd'})$ factors in equation (3), see Fig. 2. Hence, the corresponding pattern of maxima and minima in the measured $S(\mathbf{Q}, E_p/\hbar)$ is a portrayal of the entanglement between molecular qubits in state $|p\rangle$.

We have measured by 4D-INS a collection of $(Cr_7Ni)_2$ single crystals, exploiting the position-sensitive-detectors of the cold-neutron time-of-flight spectrometer IN5 at the Institute ILL in Grenoble[32]. This kind of experiment is very challenging because of two conflicting requirements: on the one hand, a detailed $\mathbf{Q}$-dependence of the scattering function over a large range of $\mathbf{Q}$ is needed. On the other hand, very high resolution is needed to resolve INS transitions within the dimer's lowest-energy manifold, whose splittings are due to the small inter-ring coupling. In addition, the large single crystals of molecular nanomagnets required for INS are very difficult to grow. To guarantee the occurrence of a factorized reference (ground) state we have applied a magnetic field $B = 2.5$ T, much stronger than any ring–ring interaction. In addition, measurements have been performed at $T = 1.2$ K to make the populations of excited states negligible. From the model of equations (1) and (2) two peaks are expected, corresponding to excitations from the factorized ground state towards two excited Bell states (marked by red arrows in Fig. 1b). Figure 1c shows that two inelastic peaks are actually observed at 0.24 and 0.28 meV, both in the energy gain and energy-loss sides (Fig. 1c). These findings are

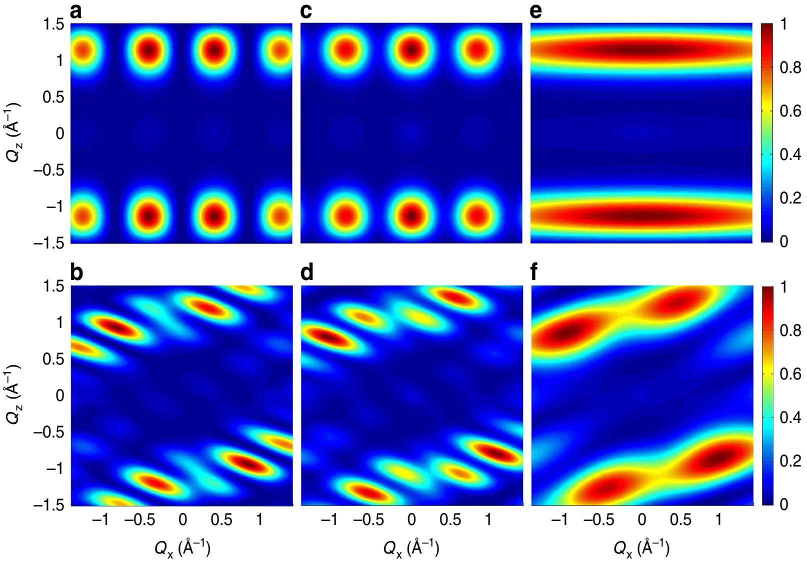

Figure 2 | Effects of inter-ring correlations on the intensity maps. Calculated neutron scattering intensity for the two in-field low-temperature inelastic transitions of the $(Cr_7Ni)_2$ dimer in the Q_x-Q_z plane. The cross section has been integrated over a symmetric Q_y range from -0.2 to 0.2 Å^{-1} and over energy ranges centred around the observed transition energies: $0.2\,\text{meV} < E < 0.25\,\text{meV}$ for **a**,**b** and $0.25\,\text{meV} < E < 0.33\,\text{meV}$ for **c**,**d**. The colour bar reports the transition intensity normalized for the maximum in each panel. The magnetic field $B = 2.5$ T is applied along the y-vertical axis. Calculations are shown in **a** and **c** for a single ideal dimer and in **b**,**d** for the real one with non-parallel rings. Short-Q modulations disappear when inter-ring correlations are forced to zero in equation (3) (**e** for an ideal dimer and **f** for the real system).

reproduced by equations (1) and (2) with $j = 1.1$ K. Preliminary measurements were also performed on the high-resolution spectrometer LET at ISIS to estimate the ring–ring coupling.

To illustrate the features in $S(\mathbf{Q}, \omega)$ reflecting inter-ring correlations and entanglement, consider the ideal case of a dimer composed by two perfectly regular and parallel rings, lying in planes parallel to the y–z plane. In this case all intra-ring distance vectors $\mathbf{R}_{dd'}$ are in the y–z plane, whereas inter-ring vectors have a large component along x (axis perpendicular to the rings). Thus, modulations of $S(\mathbf{Q}, \omega)$ as a function of Q_x directly reflect inter-ring dynamical correlations and entanglement through the term $\exp(i\mathbf{Q} \cdot \mathbf{R}_{dd'})$ in equation (3). Conversely, intra-ring correlations lead to modulations of $S(\mathbf{Q}, \omega)$ as a function of Q_y and Q_z. This is illustrated in Fig. 2a,c, that report the calculated INS intensity in the Q_x–Q_z plane for the two transitions in Fig. 1c, for an ideal $(Cr_7Ni)_2$ dimer described by equations (1) and (2). $S(\mathbf{Q}, \omega)$ is characterized by several maxima and minima whose pattern depends on the specific transition and reflects the structure of the involved wavefunctions. In particular, these maps clearly display Q_x-dependent modulations, due to the presence of entanglement in the excited $|p\rangle$ states of the dimer. On the contrary, if correlations between the two rings are forced to zero in equation (3), Q_x-dependent modulations disappear (Fig. 2e). The residual smooth Q_x-dependency of the intensity is merely due to single-ion form factors. A similar behaviour is observed if an Ising inter-ring interaction is considered, as it leads to factorized states (see Supplementary Note 3 and Supplementary Fig. 2). Figure 2b,d,f report the same calculations for a real $(Cr_7Ni)_2$ dimer, in which the planes of the rings are not parallel (they form an angle of about 30°) and their normals do not coincide with any axis of the laboratory reference frame (see 'Methods' section). Short-Q modulations of the intensity are still clearly visible for the two transitions to the entangled $|p\rangle$ states of the dimer (Fig. 2b,d) and are absent in Fig. 2f. Longer-period modulations are due to intra-ring correlations in the two non-parallel rings.

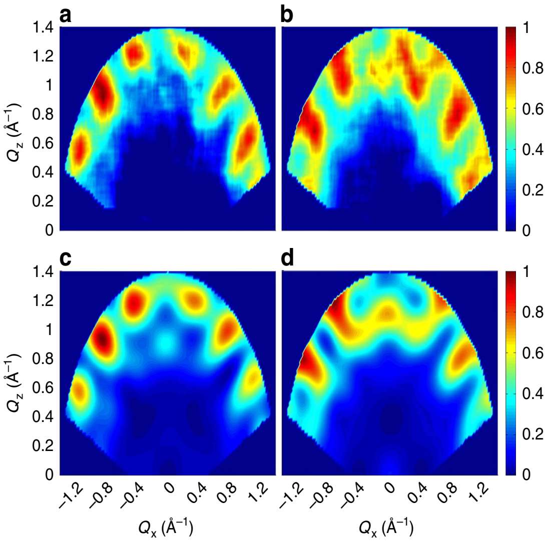

Figure 3 | Constant-energy plots of the neutron scattering intensity. **a**,**b** show the observed dependency of the neutron scattering intensity of the two inelastic excitations on the two horizontal wavevector components Q_x-Q_z, integrated over the full experimental Q_y data range measured on IN5 of -0.2 to 0.2 Å^{-1}. The measured cross section has been integrated over energy ranges centred around the observed transition energies: $0.2\,\text{meV} < E < 0.25\,\text{meV}$ for **a** and **c** and $0.25\,\text{meV} < E < 0.33\,\text{meV}$ for **b**,**d**. The colour bar reports the transition intensity normalized for the maximum in each panel. The measurement was carried out with a 7.5 Å incident neutron wavelength, a sample temperature of 1.2 K and a magnetic field $B = 2.5$ T applied along the y-vertical axis. **c**,**d** report the corresponding calculations accounting for the presence of differently oriented dimers in the crystals.

Figure 3a,b report the measured **Q**-dependence of the intensity of the two observed transitions. Short-Q modulations of the intensity are evident for both transitions, with the maxima in the low-energy excitation corresponding to minima in the high-energy one and vice versa. The observed pattern is more complex than in Fig. 2 because dimers with different orientations are present in the single crystals (see 'Methods' section). Nevertheless, these results clearly demonstrate the occurrence of entanglement in the excited states of the supramolecular dimer. Indeed, Fig. 3c,d show that the predicted short-Q modulations coincide with the experimental findings. It is worth stressing that magnetic anisotropy plays a negligible role in these results (see Supplementary Note 2), hence the different orientations of the dimers in the crystals do not affect the possibility of demonstrating the occurrence of entanglement.

Quantification of the entanglement between molecular qubits. Having experimentally shown the occurrence of entanglement, the next important question is whether is it possible to quantify it. In the following we show that it is possible to extract the concurrence C from the portrait reported in Fig. 3. C is one of the most used measures of the entanglement between a pair of qubits[33], and its value ranges from 0 for factorized states to 1 for maximally entangled ones. For pure two-qubit states $|p\rangle = a|00\rangle + b|10\rangle + c|01\rangle + d|11\rangle$, the concurrence is

$$C = 2|ad - bc|. \tag{5}$$

It is evident that $C = 0$ for a factorized state like $|01\rangle$ or $|10\rangle$ and $C = 1$ for the Bell states $(|10\rangle \pm |01\rangle)/\sqrt{2}$.

In the case of a molecular qubit, the $|0\rangle$ and $|1\rangle$ states are typically encoded in the two lowest-energy eigenstates (for example, the ground total spin $S = 1/2$ doublet in Cr$_7$Ni). By considering two molecular qubits (A, B) and restricting to the computational basis (that is, the subspace in which both molecular qubits are in the lowest doublet), the scattering function $S(\mathbf{Q}, E_p/\hbar)$ for the transitions from the factorized $|00\rangle$ ground state to excited $|p\rangle$ states contains two single-qubit contributions and an interference term:

$$S\big(\mathbf{Q}, E_p/\hbar\big) = |b|^2 I_{AA}(\mathbf{Q}) + |c|^2 I_{BB}(\mathbf{Q}) + 2Re[b\,c^* I_{AB}(\mathbf{Q})]. \tag{6}$$

By considering molecular qubits characterized by a well isolated $S = 1/2$ doublet, the explicit expression of the three contributions is:

$$I_{AA} = \sum_{\alpha,\beta=x,y,z}\left(\delta_{\alpha,\beta} - \frac{Q_\alpha Q_\beta}{Q^2}\right)\sum_{d,d'\in A} F_d(Q) \tag{7}$$

$$F_{d'}(Q)\exp(i\mathbf{Q}\cdot\mathbf{R}_{dd'})c_d c_{d'}\langle 00|S_\alpha^A|10\rangle\langle 10|S_\beta^A|00\rangle$$

$$I_{BB} = \sum_{\alpha,\beta=x,y,z}\left(\delta_{\alpha,\beta} - \frac{Q_\alpha Q_\beta}{Q^2}\right)\sum_{d,d'\in B} F_d(Q) \tag{8}$$

$$F_{d'}(Q)\exp(i\mathbf{Q}\cdot\mathbf{R}_{dd'})c_d c_{d'}\langle 00|S_\alpha^B|01\rangle\langle 01|S_\beta^B|00\rangle$$

$$I_{AB} = \sum_{\alpha,\beta=x,y,z}\left(\delta_{\alpha,\beta} - \frac{Q_\alpha Q_\beta}{Q^2}\right)\left[\sum_{d\in A,d'\in B} F_d(Q)\right. \tag{9}$$

$$\left.F_{d'}(Q)\exp(i\mathbf{Q}\cdot\mathbf{R}_{dd'})c_d c_{d'}\langle 00|S_\alpha^A|10\rangle\langle 01|S_\beta^B|00\rangle\right],$$

where the second summation is over the sites d and d' of ring A or B, $S_\alpha^{A,B}$ are effective spin-1/2 operators acting in the ground doublet of each molecular qubit and c_d are the corresponding projection coefficients[34]. This formula can be generalized to other types of molecular doublets. The factorized $|00\rangle$ ground state (obtained by applying a sizeable magnetic field) implies that $a = 0$ because $\langle 00|p\rangle = 0$.

All the quantities in I_{AA}, I_{BB} and I_{AB} are here calculated by assuming the $S = 1/2$ doublet deduced from the model interpreting measurements on the single-ring compound[26]. It is important to note that these quantities can be also determined from measurements on single-qubit compounds (for instance, in Cr$_7$Ni the c_d coefficients can be extracted by measuring local magnetic moments with nuclear magnetic resonance[35] or polarized neutron diffraction[36]). Hence, the concurrence $C = 2|bc|$ of the two excited states can be extracted from the data by fitting the observed **Q**-dependence (Fig. 3) with equation (6). It is worth noting that the inter-qubit interference contribution to $S(\mathbf{Q}, E_p/\hbar)$ (third term in equation (6)) enables one to discriminate between $|p\rangle$ states with real and complex coefficients. For the present experimental configuration, the observed short-Q modulations in $S(\mathbf{Q}, E_p/\hbar)$, integrated over an asymmetric range of Q_y, point to real wavefunctions (see Supplementary Note 4 and Supplementary Fig. 3), as expected for dominant Heisenberg interactions. Figure 4 shows the calculated **Q**-dependence of the transitions assuming different real values of b and c, corresponding to different values of C. Calculations for

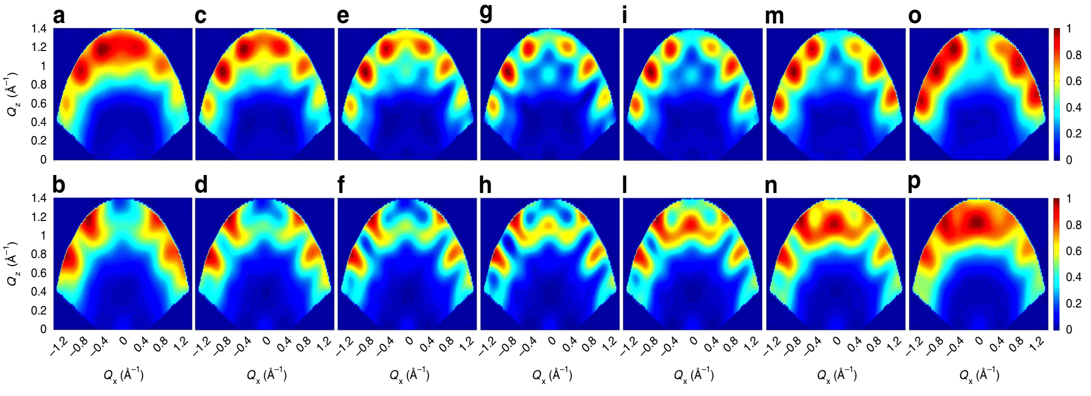

Figure 4 | Intensity plots for different values of the concurrence C. Calculations of the dependency of the INS intensity on the wavevector components Q_x-Q_z (integrated over the measured Q_y range) for different compositions of the excited states $|p\rangle$ (assuming $d = 0$ because of the sizeable applied field). The colour bar reports the transition intensity normalized for the maximum in each panel. Figures in the first (second) row correspond to the lower-energy (higher-energy) excitation. Real wavefunctions with positive values of c increasing (decreasing) from left to right are shown in the first (second) row and lead to different values of the concurrence: $C = 0.25$ for **a**,**b**,**o**,**p**, $C = 0.5$ for **c**,**d**,**m**,**n**, $C = 0.75$ for **e**,**f**,**i**,**l** and $C = 1$ for **g**,**h**.

positive values of c increasing (decreasing) from left to right are reported in the first (second) row, while examples with complex wavefunctions are reported in the Supplementary Note 4. The comparison between Figs 3a,b and 4 clearly shows that $C \simeq 1$ for both excited states. It is worth noting that this kind of information cannot be extracted by measuring the energy spectrum as in Fig. 1c, because the mere observation of two peaks is compatible with many possible models with $C < 1$. For instance, an Ising dimer model with two slightly different g values would yield a similar INS energy spectrum, but the two excited states would be factorized and $C = 0$ (see Supplementary Fig. 2). Furthermore, by determining the concurrence of the eigenstates by this approach, it is also possible to extract the concurrence in the thermodynamic equilibrium state as a byproduct[37].

Discussion

To summarize, by using the $(Cr_7Ni)_2$ supramolecular dimer as a benchmark, we have shown that the richness of 4D-INS enables us to portray entanglement in weakly coupled molecular qubits and to quantify it. This possibility opens remarkable perspectives in understanding of entanglement in complex spin systems. Molecular nanomagnets are among the best examples of real spin systems with a finite size, and are an ideal testbed to address this issue: they are also currently attracting increased attention for quantum information processing[38–40]. Tailored finite spin systems can also be assembled on a surface by using a scanning tunnelling microscope[41,42], but molecular nanomagnets have the advantage that a macroscopic number of identical and independent units can be gathered in the form of high-quality crystals. These enable elusive properties like entanglement to be explored by bulk techniques as 4D INS. It is important to underline that the present method works independently of the specific form of the inter-qubit interaction. Indeed, neither the demonstration of the entanglement through the observed short-Q modulations of the intensity, nor its quantification using equation (6), exploit equation (2). Hence, entanglement can be investigated even between molecular qubits where a sound determination of the full spin Hamiltonian is not possible, as might be the case for molecules containing 4*f* or 5*f* magnetic ions.

The use of larger single crystals and the consequent increase in the quality of the data, together with additional measurements at higher energies, will even allow the determination of two-spin dynamical correlation functions involving individual spins belonging to different molecular qubits. For instance, this would permit the direct determination of the quantum Fisher information[13], a witness for genuinely multipartite entanglement and the detection of entanglement between subsystems of the complex spin cluster[15]. Finally, the improvement in the flexibility and in the flux of the new generation of spectrometers, like those under development at the new European Spallation Source (https://europeanspallationsource.se), will further expand the possibilities of this kind of technique.

Methods

Synthesis and crystal structure. Unless stated otherwise, all reagents and solvents were purchased from Sigma-Aldrich and used without further purification. Analytical data were obtained by the Microanalysis laboratory at the University of Manchester. Carbon, hydrogen and nitrogen analysis (CHN) by Flash 2000 elemental analyser. Metals analysis by Thermo iCap 6300 Inductively coupled plasma optical emission spectroscopy.

Compound $[Cr_7NiF_3(Meglu)(O_2C^tBu)_{15}\ Et_2O]$ (1) was obtained by a similar method reported in ref. 43 for $Cr_7NiF_3(Etglu)(O_2C^tBu)_{15}\ Et_2O]$ in ~30% yield by using *N*-methyl-*D*-glucamine ($H_5Meglu = C_7H_{12}NO_5H_5$) instead of *N*-ethyl-*D*-glucamine ($H_5Etglu = C_8H_{14}NO_5H_5$).

Synthesis of $[Cr_7NiF_3(Meglu)(O_2C^tBu)_{15}]_2(C_4H_4N_2)$ (where $C_4H_4N_2$ = pyrazine): pyrazine (0.1 g, 1.25 mmol) was added to a warm (~30 °C) solution of 1 (6.0 g, 2.65 mmol) in dichloromethane anhydrous (130 ml) and the solution was stirred for 5 min, and then allowed to stand at room temperature for 7 days, during which time dark purple crystals of $[Cr_7NiF_3(Meglu)(O_2C^tBu)_{15}]_2(C_4H_4N_2)$ grew. The crystals were collected by filtration, washed with a small amount of dichloromethane and dried in a flow of nitrogen. Yield: 4.3 g (77%, based on pyrazine); elemental analysis calculated (%) for ($C_{168}H_{298}Cr_{14}F_6N_4Ni_2O_{70}$): Cr 16.35, Ni 2.64, C 45.31, H 6.75, N 1.26; found: Cr 15.89, Ni 2.53, C 45.81, H 6.77, N 1.07.

Single-large crystals preparation of $(Cr_7Ni)_2$ dimer: a powder of $[Cr_7NiF_3(Meglu)(O_2C^tBu)_{15}]_2(C_4H_4N_2)$ (3.0 g) was dissolved in refluxing dichloromethane anhydrous (100 ml) in an Erlenmeyer 500-ml flask, while stirring for 10 min and then anhydrous anisole (C_7H_8O) (25 ml) added and the solution was filtered. The filtrated was left undisturbed at ambient temperature under nitrogen for 2 weeks, during which time large well-shaped needles crystals alongside with small crystals including good X-ray quality crystals grew. The crystals were identified by X-ray crystallography as $[Cr_7NiF_3(Meglu)(O_2C^tBu)_{15}]_2(C_4H_4N_2)\ (CH_2Cl_2) \cdot 4(C_7H_8O)$ in short $(Cr_7Ni)_2$ dimer, and maintained in contact with the mother liquor to prevent degradation of the crystal quality. Elemental analysis for a powder sample obtained from several large $(Cr_7Ni)_2$ dimer crystals dried *en vacuo*; elemental analysis calculated (%) for ($C_{168}H_{298}Cr_{14}F_6N_4Ni_2O_{70}$): Cr 16.35, Ni 2.64, C 45.31, H 6.75, N 1.26; found: Cr 16.18, Ni 2.58, C 45.24, H 6.73, N 1.14.

X-ray data for compound $[Cr_7NiF_3(C_7H_{12}NO_5)(O_2CC(CH_3)_{15})]_2(N_2C_4H_4)$ were collected at a temperature of 150 K using a using Mo–K radiation on an Agilent Supernova, equipped with an Oxford Cryosystems Cobra nitrogen flow gas system. Data were measured and processed using CrysAlisPro suite of programs. More details on the crystal structure determination, crystal data and refinement parameters are reported in Supplementary Note 5 and Supplementary Table 1.

Supplementary Data 1 contains the supplementary crystallographic data for this paper.

Neutron scattering experiments. INS experiments were performed on the IN5 time-of-flight inelastic neutron spectrometer[32] at the high-flux reactor of the Institute Laue-Langevin. The IN5 instrument has a 30 m^2 position sensitive detector divided in 10^5 pixels, covering 147° of azimuthal angle and ±20° out-of plane. Six $(Cr_7Ni)_2$ single crystals were aligned on a copper sample holder with the [010] direction vertical. The crystals were placed with the flat faces perpendicular to the [110] or [1–10] directions lying on the sample holder, giving two set of crystal orientations. The dimensions of the crystals ranged from a minimum of $5 \times 3 \times 2$ mm to a maximum of $8 \times 4 \times 2$ mm. Measurements were taken by rotating the crystals (in steps of 1°) about the vertical axis, labelled y in the laboratory frame.

An incident neutron wavelength of 7.5 Å was selected to probe the excitations centred at 0.24 and 0.28 meV, with an energy resolution (full-width at half-maximum) of 22 μeV at the elastic line. The magnetic field was applied along the y-vertical axis.

Preliminary measurements were also performed on the high-resolution LET[44] spectrometer at ISIS neutron spallation source using an incident energy of 2.5 meV (40 μeV energy resolution), at a temperature of 1.8 K and a field of 5 T.

Data analysis and simulations. Measurements for different rotation angles were combined using the HORACE analysis suite[45]. Corrections for attenuation as a function of rotation and scattering angle based on the slab-like geometry of the sample holder were performed using the formula given in ref. 46. To isolate magnetic signals from the background and to separate in energy the two transitions, the data reported in Fig. 3a,b have been obtained by integrating over the full Q_y range and by fitting, for each set (Q_x, Q_z), the resulting energy dependence with two gaussians plus a background contribution. The four supra-molecules in the unit cell were included in the calculation of the scattering functions in equations (3) and (6). The two sets of crystal orientations were also taken into account in our simulations, to obtain the intensity maps in Figs 3c,d and 4.

Data availability. Supplementary Data 1 has been deposited at the Cambridge Crystallographic Data Centre (deposition number: CCDC 1480868) can be obtained free of charge via www.ccdc.cam.ac.uk/conts/retrieving.html (or from the Cambridge Crystallographic Data Centre, 12 Union Road, Cambridge CB21EZ, UK; fax: (+44)1223-336-033; or deposit@ccdc.cam.ac.uk).

Raw data from the INS experiment were generated at the Insitut Laue-Langevin large-scale facility and are available at the ILL Data Portal with the identifier http://doi.ill.fr/10.5291/ILL-DATA.4-04-457. Derived data supporting the findings of this study are available from the corresponding author upon reasonable request.

References

1. Einstein, A., Podolsky, B. & Rosen, N. Can quantum-mechanical description of physical reality be considered complete? *Phys. Rev.* **47,** 777–780 (1935).
2. Bell, J. S. On the Einstein Podolsky Rosen paradox. *Physics* **1,** 195–200 (1964).
3. Horodecki, R., Horodecki, P., Horodecki, M. & Horodecki, K. Quantum entanglement. *Rev. Mod. Phys.* **81,** 865–942 (2009).
4. Amico, L., Fazio, R., Osterloh, A. & Vedral, V. Entanglement in many-body systems. *Rev. Mod. Phys.* **80,** 517–576 (2008).

5. Eisert, J., Cramer, M. & Plenio, M. B. Colloquium: area laws for the entanglement entropy. *Rev. Mod. Phys.* **82,** 277–306 (2010).
6. Calabrese, P. & Cardy, J. Entanglement entropy and conformal field theory. *J. Phys. A* **42,** 504005 (2009).
7. Nishioka, T., Ryu, S. & Takayanagi, T. Holographic entanglement entropy: an overview. *J. Phys. A* **42,** 504008 (2009).
8. Nielsen, M. A. & Chuang, I. L. *Quantum Computation and Quantum Information* (Cambridge University Press, 2010).
9. James, D. F. V., Kwiat, P. G., Munro, W. J. & White, A. G. Measurement of qubits. *Phys. Rev. A* **64,** 052312 (2001).
10. Pan, J. *et al.* Multiphoton entanglement and interferometry. *Rev. Mod. Phys.* **84,** 777–838 (2012).
11. Jurcevic, P. *et al.* Quasiparticle engineering and entanglement propagation in a quantum many-body system. *Nature* **511,** 202–205 (2014).
12. Gühne, O. & Tóth, G. Entanglement detection. *Phys. Rep.* **474,** 1–75 (2009).
13. Hauke, P., Heyl, M., Tagliacozzo, L. & Zoller, P. Measuring multipartite entanglement through dynamic susceptibilities. *Nat. Phys.* **12,** 778–782 (2016).
14. Wieśniak, M., Vedral, V. & Brukner, Č. Magnetic susceptibility as a macroscopic entanglement witness. *New J. Phys.* **7,** 258 (2005).
15. Troiani, F., Carretta, S. & Santini, P. Detection of entanglement between collective spins. *Phys. Rev. B* **88,** 195421 (2013).
16. Giustina, M. *et al.* Bell violation using entangled photons without the fair-sampling assumption. *Nature* **497,** 227–230 (2013).
17. Ballance, C. J. *et al.* Hybrid quantum logic and a test of Bell's inequality using two different atomic isotopes. *Nature* **528,** 384–386 (2015).
18. Walborn, S. P., Ribeiro, P. H. S., Davidovich, L., Mintert, F. & Buchleitner, A. Experimental determination of entanglement with a single measurement. *Nature* **440,** 1022–1024 (2006).
19. Islam, R. *et al.* Measuring entanglement entropy in a quantum many-body system. *Nature* **528,** 77–83 (2015).
20. Siloi, I. & Troiani, F. Towards the chemical tuning of entanglement in molecular nanomagnets. *Phys. Rev. B* **86,** 224404 (2012).
21. Troiani, F. *et al.* Molecular engineering of antiferromagnetic rings for quantum computation. *Phys. Rev. Lett.* **94,** 207208 (2005).
22. Santini, P., Carretta, S., Troiani, F. & Amoretti, G. Molecular nanomagnets as quantum simulators. *Phys. Rev. Lett.* **107,** 230502 (2011).
23. Candini, A. *et al.* Entanglement in supramolecular spin systems of two weakly coupled antiferromagnetic rings (purple-Cr_7Ni). *Phys. Rev. Lett.* **104,** 037203 (2010).
24. Siloi, I. & Troiani, F. Detection of multipartite entanglement in spin rings by use of exchange energy. *Phys. Rev. A* **90,** 042328 (2014).
25. Baker, M. L. *et al.* Spin dynamics of molecular nanomagnets unravelled at atomic scale by four-dimensional inelastic neutron scattering. *Nat. Phys.* **8,** 906–911 (2012).
26. Garlatti, E. *et al.* A detailed study of the magnetism of chiral $\{Cr_7M\}$ rings: an investigation into parametrization and transferability of parameters. *J. Am. Chem. Soc.* **136,** 9763–9772 (2014).
27. Caciuffo, R. *et al.* Spin dynamics of heterometallic Cr_7M wheels (M = Mn, Zn, Ni) probed by inelastic neutron scattering. *Phys. Rev. B* **71,** 174407 (2005).
28. Carretta, S. *et al.* Quantum oscillations of the total spin in a heterometallic antiferromagnetic ring: evidence from neutron spectroscopy. *Phys. Rev. Lett.* **98,** 167401 (2007).
29. Wedge, C. J. *et al.* Chemical engineering of molecular qubits. *Phys. Rev. Lett.* **108,** 107204 (2012).
30. Chiesa, A. *et al.* Molecular nanomagnets with switchable coupling for quantum simulation. *Sci. Rep.* **4,** 7423 (2014).
31. Lovesey, S. W. *Theory of Neutron Scattering from Condensed Matter* Vol. 2 (Oxford University Press, 1984).
32. Ollivier, J. & Mutka, H. In5 cold neutron time-of-flight spectrometer, prepared to tackle single crystal spectroscopy. *J. Phys. Soc. Jpn* **80,** SB003 (2011).
33. Wootters, W. K. Entanglement of formation of an arbitrary state of two qubits. *Phys. Rev. Lett.* **80,** 2245 (1998).
34. Bencini, A. & Gatteschi, D. *Electron Paramagnetic Resonance of Exchange Coupled Systems* (Springer-Verlag, 1990).
35. Micotti, E. *et al.* Local spin moment distribution in antiferromagnetic molecular rings probed by NMR. *Phys. Rev. Lett.* **97,** 267204 (2006).
36. Guidi, T. *et al.* Direct observation of finite size effects in chains of antiferromagnetically coupled spins. *Nat. Commun.* **6,** 7061 (2015).
37. Gunlycke, D., Kendon, V. M., Vedral, V. & Bose, S. Thermal concurrence mixing in a one-dimensional Ising model. *Phys. Rev. A* **64,** 042302 (2001).
38. Ferrando-Soria, J. *et al.* A modular design of molecular qubits to implement universal quantum gates. *Nat. Commun.* **7,** 11377 (2016).
39. Shiddiq, M. *et al.* Enhancing coherence in molecular spin qubits via atomic clock transitions. *Nature* **531,** 348–351 (2016).
40. Aguilá, D. *et al.* Heterodimetallic [LnLn'] lanthanide complexes: toward a chemical design of two-qubit molecular spin quantum gates. *J. Am. Chem. Soc.* **136,** 14215–14222 (2014).
41. Khajetoorians, A. A. *et al.* Atom-by-atom engineering and magnetometry of tailored nanomagnets. *Nat. Phys.* **8,** 497–503 (2012).
42. Loth, S., Baumann, S., Lutz, C. P., Eigler, D. M. & Heinrich, A. J. Bistability in atomic-scale antiferromagnets. *Science* **335,** 196–199 (2012).
43. Faust, T. B. *et al.* Chemical control of spin propagation between heterometallic rings. *Chem. Eur. J.* **17,** 14020–14030 (2011).
44. Bewley, R. I., Taylor, J. W. & Bennington, S. M. LET, a cold neutron multi-disk chopper spectrometer at ISIS. *Nucl. Instr. Methods Phys. Res. Sect. A* **637,** 128–134 (2011).
45. Ewings, R. A. *et al.* HORACE: software for the analysis of data from single crystal spectroscopy experiments at time-of-flight neutron instruments. *Nucl. Instrum. Methods Phys. Res. Sect. A* **834,** 132–142 (2016).
46. Windsor, C. G. *Pulsed Neutron Scattering* (Taylor and Francis Ltd., 1981).

Acknowledgements

Very useful discussions with M.L. Baker and F. Troiani are gratefully acknowledged. E.G., P.S., G.A. and S.C. acknowledge financial support from the FIRB Project No. RBFR12RPD1 of the Italian Ministry of Education and Research. G.T., I.J.V.-Y., G.F.S.W. and R.E.P.W. thank the EPSRC(UK) for support, including funding for an X-ray diffractometer (grant number EP/K039547/1) and for the CDT NowNANO, which supported G.F.S.W. We acknowledge the Institute Laue-Langevin for funding the PhD of S.A. and for instrument time. We thank the ILL technical staff, in particular S. Turc and J. Halbwachs for technical assistance during the experiment. We thank John Crawford and Michael Hellier from the ISIS technical support for designing and machining the sample holders for the INS experiments.

Author contributions

E.G., T.G., S.A., P.S., J.O., H.M. and S.C. performed the experiment on crystals synthesized by G.T. after discussion with R.E.P.W. Data treatment was made by E.G., T.G., S.A., J.O., H.M., S.C., and data simulations and fits were performed by E.G., P.S., G.A. and S.C. The structure of the compound has been determined by T.G., I.J.V.-Y. and G.F.S.W. E.G., T.G., P.S., G.A. and S.C. developed the idea to use 4D INS measurements to portray and quantify entanglement in dimers of molecular nanomagnets. E.G., P.S., G.A. and S.C. also did theoretical calculations. E.G. and S.C. wrote the manuscript with inputs from all coauthors.

Additional information

Supplementary Information accompanies this paper at http://www.nature.com/naturecommunications

Competing financial interests: The authors declare no competing financial interests.

Reprints and permission information is available online at http://npg.nature.com/reprintsandpermissions/

How to cite this article: Garlatti, E. *et al.* Portraying entanglement between molecular qubits with four-dimensional inelastic neutron scattering. *Nat. Commun.* **8,** 14543 doi: 10.1038/ncomms14543 (2017).

Publisher's note: Springer Nature remains neutral with regard to jurisdictional claims in published maps and institutional affiliations.

This work is licensed under a Creative Commons Attribution 4.0 International License. The images or other third party material in this article are included in the article's Creative Commons license, unless indicated otherwise in the credit line; if the material is not included under the Creative Commons license, users will need to obtain permission from the license holder to reproduce the material. To view a copy of this license, visit http://creativecommons.org/licenses/by/4.0/

© The Author(s) 2017

Chapter 6 Conclusion

We have used INS to investigate several different molecular nanomagnets spanning different topics in the general field of current research. The third chapter of this work started off by examining a pair of dimers in a relatively tiny quantity of 0.1 g compared to the several g that were first required when neutrons were initially applied to molecular nanomagnet dimer systems. The lack of hydrogen which would result in strong incoherent scattering in these systems have allowed us to obtain staggeringly clean spectra which has permitted us to characterise the Ni dimer with relative ease. For the Co dimer the addition of orbital angular momentum complicates the physics but with a spin-only model we have still been able to arrive at a satisfactory characterisation of the magnetic properties in this system.

The powder of 4D-INS has allowed us to address the long standing problem of the spin Hamiltonian describing the magnetic properties of the famous Mn_{12} nanomagnet. Such applications of this technique to these systems were the obvious next step following the benchmark experiment by Baker *et al*[47]. and with the deuteration of this molecule we were able to obtain very good data allowing a huge amount of information on this system to be extracted and thus we were able to pin down the spin Hamiltonian terms. This important result provides assurance about the ability to characterise the Hamiltonians of future nanomagnets with complex polymetallic cores.

This technique has also helped us to characterise the significant amount of anisotropy delivered into a ring of Cr_8 by the insertion of Co(II), which represents a promising methodology for developing future SMMs.

Lastly one of the most exciting areas of the field is undoubtedly the potential application for molecular nanomagnets to be encoded as qubits for quantum information processing. The need to identify any potential entanglement in these compounds is essential for their application. Indeed entanglement is the major resource in QIP and we have also demonstrated that INS could be used to quantify if there is sufficient entanglement present for their implementation.

The role in which INS has to play will be vital if the future realisation of these systems in technologies of the future is to be achieved. With the first neutrons at the European Spallation Source now only a few years away the power of ToF neutron scattering to extract even more information on these promising systems seems just beyond the horizon.

References

[1] K.H.J Buschow, F.R. De Boer, *Physics of Magnetism and Magnetic Materials*, (Kluwer Academic publishers Netherlands **2003**).

[2] S. Blundell, *Magnetism in Condensed Matter*, (Oxford University Press, UK **2001**).

[3] O. Waldmann, T.C. Stamatatos, G. Christou, H.U. Güdel, I. Sheikin, H. Mutka, *Phys Rev. Lett.* **2009**, *102*, 157202.

[4] P. Santini, S. Carretta, G. Amoretti, T. Guidi, R. Caciuffo, A. Caneschi, D. Rovai, Y. Qiu, J. R.D. Copley, *Phys. Rev. B* **2005,** *71*, 184405.

[5] S. Carretta, P. Santini, G. Amoretti, T. Guidi, J.R.D. Copley, Y. Qiu, R. Caciuffo, G.A. Timco, R.E.P. Winpenny, *Phys Rev. Lett.* **2007**, *98*, 167401.

[6] M.N. Leuenberger and D. Loss, *Nature* **2001**, *410*, 789.

[7] D. Gatteschi and R. Sessoli, *Angewandte Chemie-International Edition* **2003**, *42*, 268.

[8] M. Affronte, A. Ghirri, S. Carretta, G. Amoretti, S. Piligkos, G.A. Timco, R.E.P. Winpenny, *Appl. Phys. Lett.* **2004,** *84,* 3468.

[9] J.M. Frost, K.L.M. Harriman, M. Murugesu, *Chemical Science* **2016,** *7*, 2470.

[10] A. Bencini and D. Gatteschi, *EPR of Exchange Coupled Systems*, (Dover publications, UK **2012**).

[11] D.W. Bruce, D. O'Hare, R.I. Walton, *Molecular Materials*, (John Wiley and Sons **2010**).

[12] E. Garlatti, *PhD thesis*, *Università Degli Studi Di Milano*, **2014**.

[13] D. Gatteschi, R.Sessoli, J. Villain, *Molecular Nanomagnets,* (Oxford University Press, UK **2006**).

[14] T. Lis, *Acta Crystallographica Section A* **1980**, *36*, 2042.

[15] R. Sessoli, D. Gatteschi, A. Caneschi, M.A. Novak, *Nature* **1993**, *365,* 141.

[16] R. Sessoli, H. L. Tsai, A.R. Schake, S. Wang, J.B. Vincent, K. Folting, D. Gatteschi, G. Christou, D.N. Hendrickson, *J. Am. Chem. Soc.* **1993**, *115*, 1804.

[17] J.R. Friedman, M. P. Sarachik, J. Tejada, J. Maciejewski, R. Ziolo, *Journal of Applied Physics* **1996,** *79*, 6031.

[18] J.M. Hernandez, X.X. Zhang, F. Luis, J. Tejada, J.R. Friedman, M.P. Sarachik, R. Ziolo, *Phys. Rev. B* **1997,** *55*, 5858.

[19] L. Thomas, F. Lionti, R. Ballou, D. Gatteschi, R. Sessoli, B. Barbara, *Nature* **1996**, *383*, 145.

[20] D. Gatteschi, A.L. Barra, A. Caneschi, A. Cornia, R. Sessoli, L. Sorace, *Coordination Chemistry Reviews* **2006,** *250*, 1514.

[21] A.L. Barra, D. Gatteschi, R. Sessoli, *Phys. Rev. B* **1997,** *56*, 8192.

[22] M.L. Baker and H. Mutka, *European Physical Journal-Special Topics* **2012***,* *213*, 53.

[23] F.K. Larsen, E.J.L. McInnes, H. E Mkami, J. Overgaard, S. Piligkos, G. Rajaraman, E. Rentschler, A.A. Smith, G.M. Smith, V. Boote, M. Jennings, G.A. Timco, R.E.P. Winpenny, *Angewandte Chemie-International Edition* **2003,** *42*, 101.

[24] S. Carretta, J. van Slageren, T. Guidi, E. Liviotti, C. Mondelli, D. Rovai, A. Cornia, A.L. Dearden, F. Carsughi, M. Affronte, C. D. Frost, R.E.P. Winpenny, D. Gatteschi, G. Amoretti, R. Caciuffo, *Phys. Rev. B* **2003,** *67*, 094405.

[25] G.A. Timco, A.S. Batsanov, F.K. Larsen, C.A. Muryn, J. Overgaard, S.J. Teat, R.E.P. Winpenny, *Chemical Communications* **2005**, *29*, 3649.

[26] G.A. Timco, E.J.L. McInnes, R.G. Pritchard, F. Tuna, R.E.P. Winpenny, *Angewandte Chemie-International Edition* **2008**, *47*, 9681.

[27] G.F.S. Whitehead, J. Ferrando-Soria, L. Carthy, R.G. Pritchard, S.J. Teat, G.A.Timco, R.E.P Winpenny, *Dalton Transactions* **2016**, *45*, 1638.

[28] G.A. Timco, T.B. Faust, F. Tuna, R.E.P. Winpenny, *Chemical Society Reviews* **2011**, *40*, 3067.

[29] M. Affronte, I. Casson, M. Evangelisti, A. Candini, S. Carretta, C.A. Muryn, S.J. Teat, G.A. Timco, W. Wernsdorfer, R.E.P. Winpenny, *Angewandte Chemie-International Edition* **2005**, *44*, 6496.

[30] G.F.S. Whitehead, B. Cross, L. Carthy, V.A. Milway, H. Rath, A. Fernandez, S.L. Heath, C.A. Muryn, R.G. Pritchard, S.J. Teat, G.A. Timco, R.E.P. Winpenny, *Chem. Commun.* **2013**, *49*, 7195.

[31] A. Ardavan, O. Rival, J.J.L. Morton, S.J. Blundell, A.M. Tyryshkin, G.A. Timco, R.E.P. Winpenny, *Phys Rev. Lett.* **2007,** *98*, 057201.

[32] T.B. Faust, V. Bellini, A. Candini, S. Carretta, G. Lorusso, D.R. Allan, L. Carthy, D. Collison, R.J. Docherty, J. Kenyon, J. Machin, E.J. McInnes, C.A. Muryn, H. Nowell, R.G. Pritchard, S.J. Teat, G.A. Timco, F. Tuna, G.F.S. Whitehead, W. Wernsdorfer, M. Affronte, R.E.P Winpenny, *Chemistry- A European Journal* **2011,** *17*, 14020.

[33] S.A. Wolf, D.D. Awschalom, R.A. Buhrman, J.M. Daughton, S. von Molnar, M.L. Roukes, A.Y. Chtchelkanova, D.M. Treger, *Science* **2001**, *294*, 1488.

[34] D.D. Awschalom and M.E. Flatte, *Nature Physics* **2007,** *3*, 153.

[35] S. Sanvito and A. Rocha, *J. Comput. Theor. Nanosci* **2006,** *3*, 624.

[36] R. Caciuffo, G. Amoretti, A. Murani, R. Sessoli, A. Caneschi, D. Gatteschi, *Phys Rev. Lett.* **1998,** *81*, 4744.

[37] C.M. Casadei, A. Gumiero, C.L. Metcalfe, E.J. Murphy, J. Basran, M.G. Concilio, S.C. Teixeira, T.E. Schrader, A.J. Fielding, A.

Ostermann, M.P. Blakeley, E.L. Raven, P.C. Moody, *Science* **2014**, *345*, 193.

[38] S.A. Kivelson, E. Fradkin, V.J. Emery, *Nature* **1998**, *393*, 550.

[39] C. Rüegg, N. Cavadini, A. Furrer, H.U. Güdel, K. Krämer, H. Mutka, A. Wildes, A. Habicht, P. Vorderwisch, *Nature* **2003**, *423*, 62.

[40] R. Basler, C. Boskovic, G. Chaboussant, H.U. Güdel, M.M. Murrie, S.T. Ochsenbein, A. Sieber, *Chemphyschem* **2003,** *4*, 910.

[41] R. Pynn, *Neutron Scattering A Primer*. **1990**.

[42] S.W. Lovesey, *Theory of neutron scattering from condensed matter,* (Oxford University Press, UK, **1971**).

[43] L.G. Squires, *Introduction to the theory of thermal neutron scattering* (Dover publications, US **1996**).

[44] J. Ollivier, J.-M. Zanotti, *Collection SFN* **2010**, *10,* 379.

[45] https://www.ill.eu/instruments-support/instruments-groups/instruments/in5

[46] F. Hipper, E. Geissler, J.L. Hodeau, E.L-Berna, J-L. Regnard, *Neutron and X-ray spectroscopy, (*Grenoble Sciences, France*,* **2005**).

[47] M.L. Baker, T. Guidi, S. Carretta, J. Ollivier, H. Mutka, H.U. Güdel, G.A. Timco, E.J.L. McInnes, G. Amoretti, R.E.P. Winpenny, P. Santini, *Nature Physics* **2012**, *8*, 906.

[48] O. Waldmann, R. Bircher, G. Carver, A. Sieber, H.U Güdel, H. Mutka, *Phys. Rev. B* **2007,** *75*, 174438.

[49] R.A. Ewings, A. Buts, M.D. Le, J. van Duijn, I. Bustinduy, T.G. Perring, *Nuclear Instruments & Methods in Physics Research Section a-Accelerators Spectrometers Detectors and Associated Equipment* **2016**, *834*, 132.

[50] M.L. Baker, *PhD thesis*, *University of Manchester*, **2010.**

[51] M.L. Baker, T. Lancaster, A. Chiesa, G. Amoretti, P.J. Baker, C. Barker, S.J. Blundell, S. Carretta, D. Collison, H.U. Güdel, T. Guidi, E.J.L. McInnes, J.S. Moeller, H. Mutka, J. Ollivier, F.L. Pratt, P. Santini, F. Tuna, P.L. Tregenna-Piggott, I.J. Vitorica-Yrezabal, G.A. Timco, R.E.P. Winpenny, *Chem. Eur. J.* **2016**, *22*, 1779.

[52] D. Parshall, R. Heid, J.L. Niedziela, T. Wolf, M.B. Stone, D.L. Abernathy, D. Reznik, *Phys. Rev. B* **2014,** *89*, 064310.

[53] J.R.D. Copley and T.J. Udovic, *J. Res. Natl. Inst. Stan.* **1993,** *98*, 71.

[54] A. Furrer and O. Waldmann, *Rev. Mod. Phys.* **2013,** *85*, 367.

[55] O. Waldmann, *Phys. Rev. B* **2003,** *68*, 174406.

[56] R.E.P. Winpenny, *Molecular Cluster Magnets,* (World Scientific Publishing Company, Singapore, **2011**).

[57] M. Kofu, O. Yamamuro, T. Kajiwara, Y. Yoshimura, M. Nakano, K. Nakajima, S. Ohira-Kawamura, T. Kikuchi, Y. Inamura, *Phys. Rev. B* **2013**, *88*, 064405.

[58] K.S. Pedersen, L. Ungur, M. Sigrist, A. Sundt, M. Schau-Magnussen, V. Vieru, H. Mutka, S. Rols, H. Weihe, O. Waldmann, L.F. Chibotaru, J. Bendix, J. Dreiser, *Chemical Science* **2014**. *5*,

[59] M.L. Baker, O. Waldmann, S. Piligkos, R. Bircher, O. Cador, S. Carretta , D. Collison, F. Fernandez-Alonso, E.J.L.McInnes, H.

Mutka, A. Podlesnyak, F. Tuna, S. Ochsenbein, R. Sessoli, A. Sieber, G.A. Timco, H. Weihe, H.U. Güdel, R.E.P. Winpenny *Phys. Rev. B.* **2012**, *86,* 064405.

[60] T. Guidi, B. Gillon, S.A. Mason, E. Garlatti, S. Carretta, P. Santini, A. Stunault, R. Caciuffo, J. van Slageren, B. Klemke, A. Cousson, G.A. Timco, R.E.P. Winpenny, *Nat. Commun.* **2015,** *6*, 7061.

[61] S. Lounis, P.H. Dederichs, S. Blugel, *Phys Rev. Lett.* **2008**, *101*, 107204.

[62] H.U Güdel, A. Stebler, A. Furrer, *Inorg. Chem.* **1979**, *18*, 1021.

[63] L. Zhang, A. Bagrets, D. Xenioti, R. Korytár, M. Schackert, T. Miyamachi, F. Schramm, O. Fuhr, R. Chandrasekar, M. Alouani, M. Ruben, W. Wulfhekel, F. Evers, *Phys. Rev. B* **2015,** *91*, 195424.

[64] V.V. Mazurenko, Y.O. Kvashnin, F. Jin, H.A. De Raedt, A.I. Lichtenstein, M.I. Katsnelson, *Phys. Rev. B* **2014,** *89*, 214422.

[65] S. G.Tabrizi, A.V. Arbuznikov, M. Kaupp, *J. Phys. Chem. A* **2016**, *120*, 6864.

[66] O. Hanebaum and J. Schnack, *Phys. Rev. B* **2015,** *92*, 064424.

[67] C. Sangregorio, T. Ohm, C. Paulsen, R. Sessoli, D. Gatteschi, *Phys Rev. Lett.* **1997**, *78*, 4645.

[68] D. DiVincenzo, *Fortschritte Der Physik-Progress of Physics* **2000**, *48*, 771.

[69] D. DiVincenzo and D. Loss, *J. Magn. Magn. Mater.* **1999**, *200*, 202.

[70] I.L. Chuang and M.A. Nielsen, *Quantum Computation and Information,* (Cambridge University Press, UK, **2010**)